A multifunctional sensor system for brake system applications

by

Rogelio Hernández Aguirre

A thesis
presented to the University of Waterloo
in fulfillment of the
thesis requirement for the degree of
Master of Applied Science
in
Mechanical Engineering

Waterloo, Ontario, Canada, 2015

AUTHOR'S DECLARATION

I hereby declare that I am the sole author of this thesis. This is a true copy of the thesis, including any required final revisions, as accepted by my examiners.

I understand that my thesis may be made electronically available to the public.

Preface

This is a revised version of the thesis that was originally approved on September of 2015 by the committee and published and uploaded to UW Space. The reason of the revision is to address issues related to uncited and inappropriately cited source material.

Abstract

The objective of this thesis is to develop a multifunctional MEMS (Micro Electro Mechanical System) sensor system for the simultaneous measurement of pressure and temperature inside a hydraulic system, more specifically a hydraulic brake system for automotive applications. The multifunctional pressure and temperature sensor system presented in this Thesis was designed to be installed in a new brake-by-wire system that requires the simultaneous reading of pressure and temperature per wheel cylinder. This system needs to control and monitor these parameters at each wheel cylinder to adjust the pressure for optimal braking. Current sensing systems installed in regular brake systems use a single pressure sensor that is positioned in the main cylinder and they do not include a temperature sensor. Numerous methods have been used to control and monitor the pressure in a brake system real-time. However, no MEMS sensor system has yet been reported that can monitor pressure and temperature real-time in brake systems.

In a representative automobile hydraulic brake system, the pressure and temperature can be as high as 4 Mpa and 120 °C, respectively. These conditions are developed in an oily environment with a pH ~ 11. The multifunctional sensor system presented here is based on the two sensors, one for pressure and one for temperature, working within the same packaging. These two sensors are glued on the surface of an adequate Transistor Outline (TO) base using a temperature resistance adhesive. The substrate with the two sensors is covered by a parylene layer for dielectric protection, protection from the corrosive medium and protection from the moisture inherent in the brake fluid. The interface of the sensor system to the hydraulic brake system uses a commercial 1/4 18 NPT fitting customized to serve as an interface as well as a metal shell between the sensor and the hydraulic cylinder. The TO base and the metal shell were joined by micro-brazing to minimize heat-affected areas and ensure that critical components are unharmed.

A finite element model to understand the effect of the parylene layer on the performance of the sensors was developed using COMSOL Multiphysics®. The model was validated by testing many prototypes of the developed sensor system using a custom made hydraulic hand pump which pressure is monitored by a digital hydraulic pressure gauge. The sample fitting is covered by a coil heater that includes a type -T Thermocouple positioned close to the sample to monitor the temperature. The complete apparatus allowed characterization of the test sensor from room pressure (13 psi) to 500 psi over a temperature range of 25 to 120°C. The test samples were characterized from atmospheric

pressure to 450 psi over a temperature range of 25 to 120°C. The experimental data shows a reduction in pressure sensitivity of 18.2 % due to the parylene layer which closely agrees with the model predictions of a reduction of 21%.

In summary, a multifunctional sensor system has been developed that can be used to control and monitor the pressure and temperature of a hydraulic cylinder real-time. The sensor system is novel in that it measures both parameters at a single point real-time with good sensitivity and accuracy making it ideal for applications in brake-by-wire systems.

Acknowledgements

First a large thank-you to my supervisors, Dr. Patricia Nieva and Dr. Amir Khajepour for their support and guidance throughout the completion of my degree. I would like to acknowledge the technical support of Ashwani Angra for provided me access to the facilities of MorHEAT® to perform the experimental test. I would like to acknowledge the help of Whitfield Welding for the support with the welding samples.

I would like to acknowledge the funding and financial support provided by the Government of México. I would like to thank CONACYT (National Council of Science and Technology of Mexico) for their financial support and also Canadian Microelectronic Corporation (CMC) for their technical support.

This thesis has been done with the support of the scholarship of the Minister of Education of the government of México.

Dedication

To my family.

No bird soars too high, if he soars with his own wings, thanks for being the wind beneath mine.

Table of Contents

List of Tables

List of Figures

Chapter 1
Introduction

1.1 Overview of a Brake system

The brake system is one of the most important subsystems in the vehicles, and has drastically changed due to the progress in sensor technology, control systems, hydraulic and electrical systems, and the increased importance of safety conditions. Nowadays, brake systems have the ability to be compatible with different control systems such as the Anti-lock Brake System (ABS), Traction Control System (TCS), Vehicle Stability Control system (VSC), and regenerative braking system. To have such compatibility, it is necessary to control the braking pressure of each wheel independently. The process of providing the brake force for each wheel independently through the vehicle stability control system as opposed to the driver input is called differential braking.

On the other hand, the use of electrical components has increased in braking systems and has led to a group of smart braking systems called brake-by-wire systems. Contrary to standard systems, the process of making the braking force in these systems is not entirely mechanical, or conducted by the driver; it is created by electrical components, or in some cases from the cooperation of the electrical and hydraulic components. A new cost effective brake-by-wire system is being developed at the University of Waterloo that can control each wheel braking force independently. The general form of this braking system is shown in Figure 1.1.

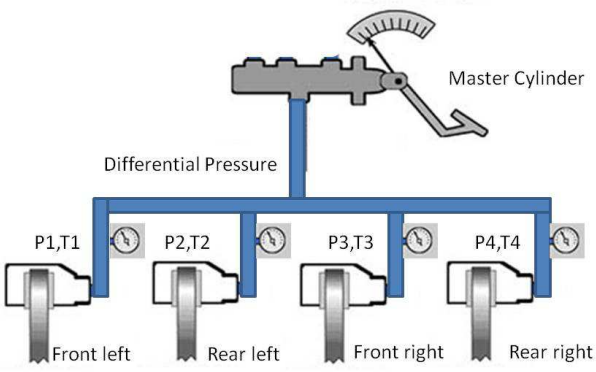

Figure 1-1. Conceptual diagram of the brake-by-wire system being developed at the University of Waterloo.

In this Electro Hydraulic Brake (EHB) system, an actuator is used to change the trapped oil volume inside the caliper cylinder to control the brake pressure directly. Each wheel has a

cylinder and an actuator, thus making it possible to control the braking force of each wheel independently. The trapped braking oil in the caliper cylinder is used to transfer force into pressure, and to amplify braking force.

Most brake fluids used today are glycol ether based with a pH~11 [1]. The system works because these liquids are not appreciably compressible since in their natural state the component molecules do not have internal voids and the molecules pack together well, so bulk forces are directly transferred to compress the fluid's chemical bonds. In operation, the brake fluid is subjected to very high temperatures, up to 120 ºC, especially in the wheel cylinders. These high temperatures can cause vaporization of the brake fluid, which is a problem because vapor is highly compressible relative to liquid, and, therefore, negates the hydraulic transfer of the braking force. Figure 1-3 shows the typical temperature profile on a brake system obtained during a wind tunnel experiment at Volvo Cars [2]. On this vehicle, thermocouples are attached at different locations of the caliper, at the front- and backside of the brake pad and within the brake fluid.

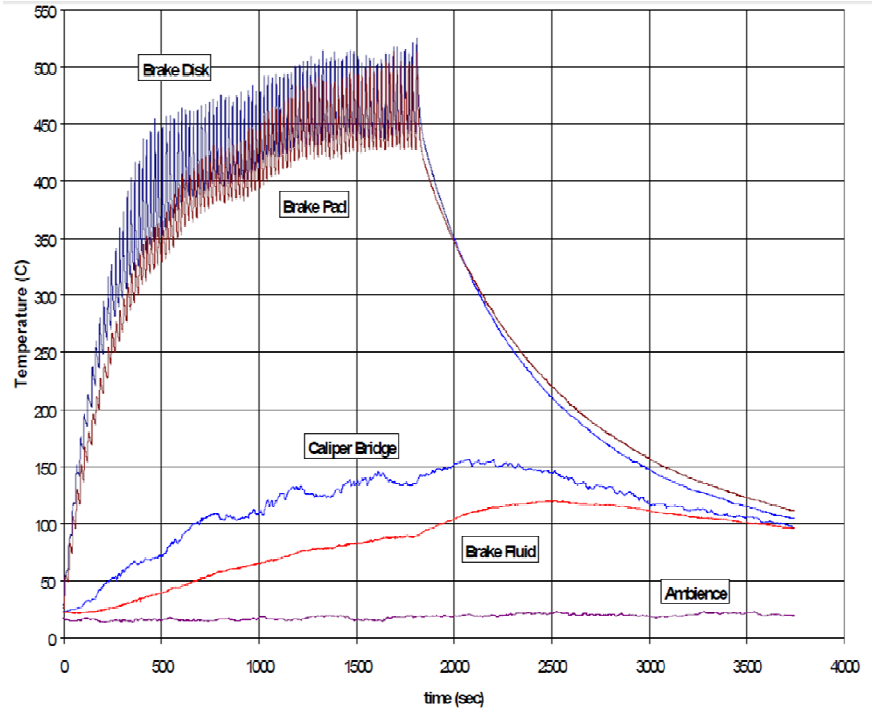

Figure 1-2. A typical temperature profile of a brake system measured by Volvo extracted from [2].

In addition to the high temperature in the hydraulic fluid, the braking performance of a vehicle can be significantly affected by the temperature rise in the brake components themselves. High temperature during braking may cause brake fade, premature wear, bearing failure, thermal

cracks, and thermally excited vibration [3]. Moreover, braking distance is directly affected by the brake system temperature. The higher the temperature of the brake system, the longer the braking distance. In these facts, reside the importance of monitoring the temperature of the brake fluid.

1.2 Overview of existing problems and research objectives

Operational data from automotive hydraulic brake systems is typically taken at the main cylinder leading to one pressure signal for all the brake system [4]. Additionally, current sensor systems monitor just pressure but not temperature. The prime peculiarity of this new brake-by-wire system is the fact that each wheel cylinder need to receive individual readings. Using current commercial sensors individual feedback will need four pressure sensors, four temperature sensors and eight different sensor penetrations in the brake system which could result in big disturbances to the braking system. To minimize intrusiveness and obtain temperature and pressure readings at a single point, a good approach is to use Micro Electro Mechanical System (MEMS) sensor systems. While numerous approaches have been taken to address the control and monitoring of the pressure in a electro-hydraulic brake system, no MEMS sensor system has yet been reported that can carry out simultaneous real-time measurements of pressure and temperature in automotive electro-hydraulic brake systems. In this Thesis, a mechatronics approach is used to integrate two different MEMS sensors, one for pressure and one for temperature, in one single package. In this approach, the pressure signal is used as the main controlled variable of the EHB system being adjusted according to the driving conditions, while the temperature sensor is used for monitoring and potentially compensating the pressure signal due to the effect of the temperature on the performance of the brake fluid. In addition, having both MEMS sensors integrated in the same package also reduces the price of fabrication and implementation.

The working conditions inside a wheel cylinder take place at relatively high temperatures, up to 120°C, and in an alkaline chemical environment of pH ~11. The pressures can reach up to 4 Mpa due primarily to the glycol ether based composition of the brake fluid. The brake fluid is hygroscopic [5] and thus the water percentage inside the brake fluid is high. While this increases the boiling point and reduces the viscosity of the brake fluid, the humidity levels in the brake fluid can damage any sensor system that operates in contact with it. Hence, proper selection of the protective packaging is needed.

The main objective of this work is to successfully deliver a constant and reliable measurement of pressure and temperature for all operation modes of an electro-hydraulic brake system using one single MEMS sensor system. The main criteria used to develop such a system includes (1) compatibility to current sensor fittings used in hydraulic brake systems ; (2) resistance to the harsh environment of the brake fluid; (3) compatibility with automotive electrical conditions; and (4) low cost.

1.3 Organization of this thesis

This thesis is presented in an introduction, four main chapters, and a conclusion chapter. Chapter 2 presents a literature review on current monitoring sensor systems for hydraulic brake systems, and a comprehensive summary of MEMS sensors for pressure and temperature measurements in a hydraulic brake system environment. The chapter concludes with a discussion of current multifunctional MEMS sensing platforms.

In Chapter 3, the working conditions inside the wheel cylinder of an EHB system are discussed first. The internal environment of the brake system presents several challenges that guide the design of the proposed MEMS sensor system. The choice of the sensing mechanisms for pressure and temperature is examined in terms of achieving the design objectives. Additionally, the fabrication process of the sensor is presented and detailed. This chapter concludes with a summary of the sensor system design.

Chapter 4 presents the modeling and analysis of the multifunctional MEMS sensor system. The sensor system was modeled to account for the effect of the packaging on the performance of the sensors. The numerical modeling was done using finite element (FE) simulations carried out by the commercial FE software COMSOL Multiphysics©.

In Chapter 5, experimental results of the fabricated devices are presented. Details of the test bench used during the experiment are described. Properties of the sensor, such as sensitivity, accuracy and linearity are discussed. Finally, the experimental results are compared with the model presented in Chapter 4.

Conclusions to the Thesis are included in Chapter 6 which also a list of the main contributions and suggested future paths for the continuation of this research.

Chapter 2
Literature Review

This chapter discusses existing research and commercial products on monitoring systems for braking systems. It also discusses MEMS sensors for pressure and temperature applications. The chapter starts by reviewing current monitoring systems for brake systems and their importance and continues on by reviewing different multifunctional MEMS approaches to measure pressure and temperature. A review of current multifunctional MEMS sensing platforms and their packaging methods is presented last.

2.1 Monitoring systems for automotive brakes

The introduction of advanced functionality such as electronic stability program (ESP), drive-by-wire, and more sophisticated actuators and sensors offer both new opportunities and requirements for more accurate and flexible control in automotive brake systems. The brake system is no longer a stand-alone system whose only purpose is to generate stable and efficient braking but it is seen as a subsystem where each wheel can receive individual brake commands from higher level control systems. Several companies have included those kinds of systems in their cars. In the following; this section presents he different approaches that have been taken by a few manufactures:

Mercedes-Benz Sensotronic Brake Control

Sensotronic Brake Control (SBC) is the name given to an innovative electronically controlled brake system that Mercedes-Benz developed in 2002 to fit the future passenger car models. With Sensotronic Brake Control electric impulses are used to pass the driver's braking commands onto a microcomputer which processes various sensor signals simultaneously and, depending on the particular driving situation, calculates the optimum brake pressure for each wheel. The primary requirements of a pressure sensor for Brake-by-Wire applications as this one, are high precision and reliability as well as multi-functionality and flexibility, features strongly desired in modern sensor design. These requirements have heavily influenced the design choice made by Mercedes. In order to enhance the precision it has been conceived a silicon micromachined piezo-resistive pressure sensor chip with two different sensitivities: a higher one in a low-pressure range (0 to 30 bar), where often an elevated resolution is required, and a lower one at higher pressures (up to 250 bar). Thus, with one single membrane chip,

practically two sensors are obtained. Fig 2-1 shows the profile of the sensor designed by Mercedes.

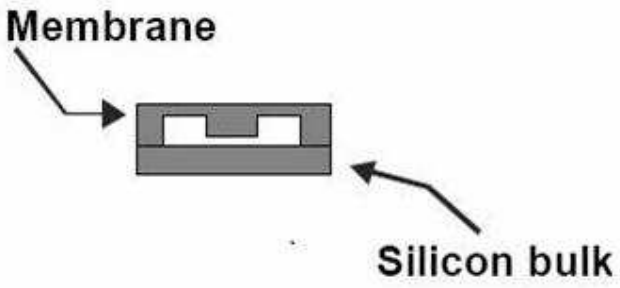

Figure 2-1 Diagram of the sensor chip profile used by Mercedes modified from [4].

The transduction of the physical quantity, pressure in this particular case, into an electrically measurable value is performed through piezo-resistive elements implanted on the surface of the silicon chip. This type of transducers is sensitive to the stresses in the two coordinates defined with respect to the plane where the elements are implanted in the chip [6]. The stresses on the piezo resistors induce changes in their resistance that can be detected with rather a high accuracy as unbalance of a Wheatstone bridge. The SBC is an example of a successful case of monitoring of pressure in an EHB; however, this system distributes the pressure to each wheel from a central unit and the pressure monitoring is performed in the same unit but not independently as is required. Moreover, this system does not monitor the temperature, just pressure.

Volvo In-Vehicle Brake System

In 2012 Neys [2] reported an In-Vehicle Brake System Temperature Model developed with Volvo Cars. The primary goal of this system is to estimate the temperature of the different brake system components, particularly the temperature of the brake fluid, in order to detect dangerous situations that can arise due to overheating of the brake system. Neys approached the problem using the sensors signals readily available in the Brake Control Module (BCM) and on the vehicle CAN-bus instead of use a temperature sensor. Fig 2-2 shows the model flow of this system. The system was capable to estimate the fluid temperature with a deviation of plus or minus 30 K. Due to the complexity of the model, this was used just for Alpine descent but not for normal daily braking.

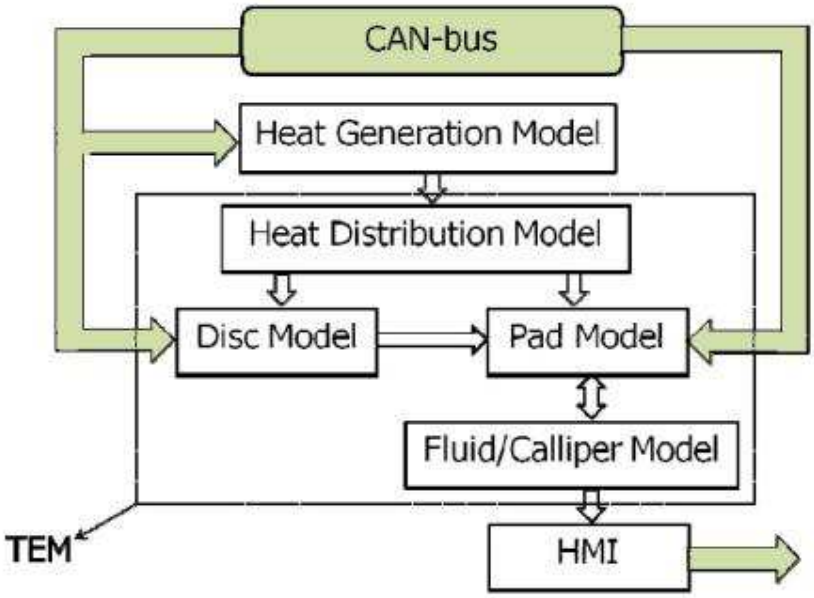

Figure 2-2 Brake System Temperature model flow chart developed by Volvo Cars extracted from [2].

The system was finished until prototype level just for one type of cars. However, a better temperature model, a new Heat Generation model, and a friendly and more efficient Human Machine Interface is necessary to implement the system into production vehicles. Another major drawback of this system is the deviation of 30 K to predict the brake fluid temperature.

European Autonomous Braking system

In 2010 the European New Car Assessment Program (EuroNCAP) required that the automobile makers include in their cars an Autonomous Emergency Braking (AEB) to obtain its highest safety rating. The Autonomous Emergency Braking system uses different radar and sensors to identify potential obstacles ahead of the car. If a potential collision is detected, AEB systems will apply bigger pressure to the brakes to reduce the speed and avoid the collision. These systems use a pressure sensor to regulate all the pressure in the system. Examples of systems using the pressure signal to control the Autonomous Emergency Braking are: FIAT City Brake Control [7], Mitsubishi Forward Collision Mitigation [8], Ford Active City Stop [9] among others. All these systems use a central pressure sensor to control the braking force of the car; however, these systems does not include the measurement of temperature.

Although the previous cases show the importance of having monitoring of temperature and pressure in a car, to the best of our knowledge, there is not a commercial monitoring system that includes both signals. In that fact, the importance of developing a multifunctional sensor resides.

2.2 Multifunctional MEMS Sensors and Packaging

Sensors detect and convert a physical phenomenon or input (e.g. pressure, heat, etc.) into a quantity or output that is readable by an instrument. Sensors and their data acquisition systems are crucial for any industrial process. There are as many sensors as there are different physical quantities to be detected.

2.2.1 Pressure MEMS Sensors

Pressure sensing is the second largest sensor market after temperature sensing, representing a 15 billion dollars global business that is growing every year [10]. They are also one of the most widely used MEMS sensors for automotive applications. MEMS pressure sensors usually use a diaphragm as a force collector to measure a change in strain (or deflection) generated due to the application of a force over the area of the diaphragm. The change in deflection is captured by a measurement system integrated with the sensor with the output typically given by an electrical signal whose amplitude is proportional to the pressure difference between the upper and bottom sides of the diaphragm. In the following, different MEMS sensing mechanisms are discussed with the objective of selecting the best one for the brake application.

Capacitive Pressure Sensor

A pressure sensor is comprised of two major parts: 1) an element that is affected by pressure changes, and 2) the associated electronics. The pressure sensing element in a capacitive pressure sensor is a pair of parallel plates which form a capacitor. One plate is fixed to a ceramic diaphragm that flexes in response to a change in pressure, thus changing the gap and the capacitance between the two electrodes (Fig 2-3).

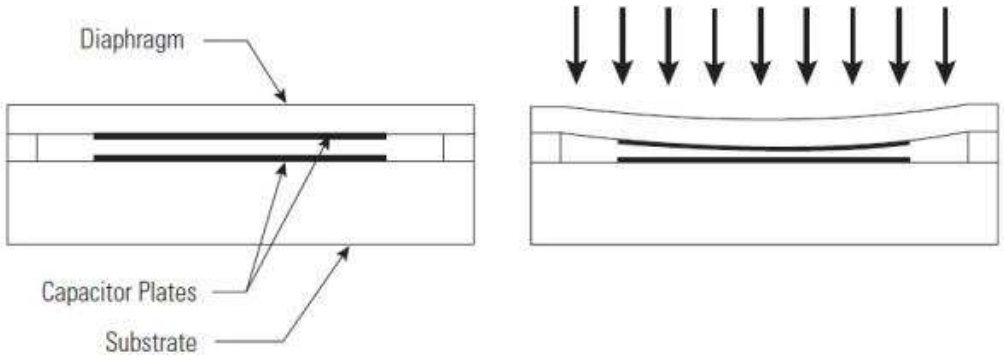

Figure 2-3. Schematic of a capacitive MEMS pressure sensor. The diaphragm is shown deflected under pressure difference.

As described in [23], capacitive pressure sensors offer several advantages over their piezoresistive counterparts because of their lower power consumption [11], smaller temperature sensitivity [12], and higher pressure sensitivity [13] . However a major drawback is their excessive signal loss from parasitic capacitances [15]. This has hindered the development of commercial capacitive MEMS pressure sensors for high temperature applications until high temperature on-chip circuitry is available [16]. In addtion, the change in capacitance is normally non-linear with pressure [17] unless a bossed diaphragm or a contact mode (touching electrodes) is used for linearization. Capacitive pressure sensors are therefore not widely used in automotive or commercial applications mainly because the complicated circuitry that is needed to get the signal. Table 2-1 shows some capacitive pressure sensors for high-pressure and high-temperature applications.

Table 2-1 Comparison of capacitive pressure sensors built for high pressure/temperature applications.

Model	Pressure Range	Temperature Resistance	Chemical Resistance against corrosion (4 > pH > 9).
K. Karsten, et al. [18]	0.1 - 3.8 MPa	25 - 250 ºC	No
Production Motorola MPXY8040A [19]	0.5 - 0.9 MPa	25 - 125 ºC	No
SENSATA [20]	0.5 - 5 MPa	25 - 250 ºC	Yes

Optical Pressure Sensors

Optical pressure sensors are based on optical interferometry and usually consist of a pair of parallel mirrors separated by an air gap. This arrangement is known as a Fabry-Perot cavity or a sensing interferometer. A semi-reflective mirror is formed by depositing a dielectric layer at the end of an optical fiber. The second mirror is formed by a diaphragm mounted at a certain distance in front of the optical fiber end. Exposing the diaphragm to pressure changes the gap between the mirrors which can be directed correlated to the applied pressure. Different pressures ranges can be accommodated by appropriately selecting thickness and diameter of the diaphragm to keep the maximum deflection and maintain a linear relation between pressure and deflection.

Optical sensors offers some advantages as: entirely passive: can be used in an explosive environment, immune to electromagnetic interference, resistant to high temperatures and chemically reactive environment, small size, and a high degree of biocompatibility. However, aligning the optics and calibrating the sensors can be challenging and expensive because of the high sensitivity [21].

Piezoresistive Pressure Sensors

First discovered by Lord Kelvin in 1856, the piezoresistive effect is widely used as a sensor principle. In piezoresistive MEMS pressure sensors, the pressure changes the resistance by mechanically deforming the diaphragm shape, enabling the piezoresistors in the diaphragm and connected in a bridge circuit, for example, to detect pressure as a proportional differential voltage across the bridge. The change in resistance is due to the physical change of the structure because of its deformation [22]. This effect provides an easy and direct energy-signal transduction mechanism between the mechanical and the electrical domains.

Nowadays, micromachined silicon-based pressure sensors are commercially available for many applications such as automotive, biomedical, and aerospace [16] and are typically offered as piezoresistive devices. Piezoresistive pressure sensors have advantages in their robustness, linearity, simple measurement circuitry, and immunity to electromagnetic noise. However, difficulties in temperature compensation and fabrication control (that would affect sensor offset) are the two major drawbacks of piezoresistive sensors compared with capacitive sensors. Piezoresistive pressure sensors typically have two longitudinal piezo resistors (R_1 and R_3) and two transverse piezo resistors (R_2 and R_4) forming a Wheatstone bridge on a silicon diaphragm. The piezoresistors measure strain at the diaphragm edges and generate an electrical output proportional to the diaphragm deflection.

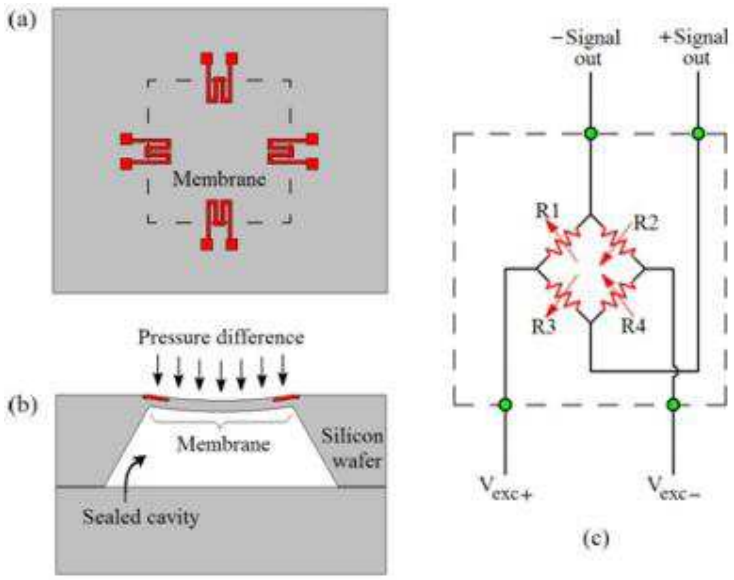

Figure 2-4 Schematic of a piezoresistive pressure sensor showing the (a) top view and (b) side view; as well as its (c) piezoresistive strain gauges connected in a Wheatstone bridge configuration. Figure extracted from [23].

Figure 2-4 presents an schematic of a piezoresistive MEMS pressure sensor and its electronic circuitry provided by a Wheatstone bridge. Their main disadvantage is their temperature dependence, which makes them susceptible to changes in ambient temperature. A temperature compensation method is used to eliminate this undesired effect by using a second sensor that measures the temperature independently to correct the pressure reading using a more sophisticated signal processing unit. Temperature compensation can be used up to where the resistance value of the piezoresistors starts to significantly drop (around 600 °C for silicon [24]).

2.2.2 Temperature Sensors

The measurement of temperature is extensively practiced and can be achieved using several different principles. A brief review of these sensors and their applications is presented next.

Thermocouple

A thermocouple is a temperature-measuring device consisting of two dissimilar conductors that contact each other at one or more spots, where a temperature differential is experienced by the different conductors (or semiconductors). It produces a voltage when the temperature of one of the spots differs from the reference temperature at other parts of the circuit. Thermocouples can usually work between -200°C to 2300 °C, depending on their configuration [25]. Any junction of dissimilar

metals will produce an electric potential related to temperature. Thermocouples for practical measurement of temperature are junctions of specific alloys which have a predictable and repeatable relationship between temperature and voltage. Some of the advantages of Thermocouples are their wide variety of physical forms, wide temperature range, inexpensive and rugged. However, the thermocouples are not linear, a reference temperature is required, are least stable and less sensitive. In addition, the deterioration of their junction over time requires that the thermocouple gets frequently calibrated [25].

Thermistor

A thermistoris based on a ceramic material whose resistance varies with temperature. Ceramic-oxide compositions are manufactured to exhibit NTC or PTC(negative, or positive, temperature coefficient) resistance characteristics, where resistance of the sensors decrease, or increase, several orders of magnitude as temperature is increased [26].Thermistors exhibit a high and fast output, and although very sensitive, their output is non-linear, and their material is fragile.

Resistive temperature detector (RTD)

Resistance thermometers, also called resistance temperature detectors (RTDs), are sensors used to measure temperature by correlating the resistance of the RTD element with temperature. It is similar to the thermistor, but with a sensing element made of metal. Most RTD elements consist of a length of fine coiled wire wrapped around a ceramic or glass core. The element is usually quite fragile, so it is often placed inside a sheathed probe to protect it. The RTD element is made from a pure material, typically platinum, nickel or copper. The material has a predictable change in resistance as the temperature changes, and it is this predictable change that is used to determine temperature [27]. The RTD is one of the most accurate temperature sensors. Not only does it provide good accuracy, but it also provides excellent stability and repeatability. It is one of the most used temperature sensors in MEMS applications [27], [28] , [29].

Infrared (IR) sensor

IR sensors (detectors) detect temperature by measuring the thermal radiation emitted by an object. The main problem of using IR sensors in an oily environment, such as the one exisiting in brake systems, is the presence of contaminants in the sensing media which could affect the surface finish of the sensing object.

2.2.3 Multifunctional MEMS Sensors

The goal of this project is to develop a fast-response multifunctional MEMS sensor system for the simultaneous measurement of pressure and temperature in an electro-hydraulic brake system. There

are two main approaches to deal with multifunctional sensors: a discrete and an integrated approach. The discrete approach to implementing a multifunctional sensing platform consists in combining several single-parameter MEMS sensors in a single packaging or chip. The integrated approach is based on the design of a single MEMS device that is sensitive to several parameters at the same time. This approach itis more complex but it allows for smaller and more accurate MEMS sensor systems.

In the following, a review of some recent efforts on developing multifunctional MEMS sensors according to the aforementioned categorization is presented.

Discrete approach

As described in [23], the Berkeley Sensor and Actuator Center (BSAC) at the University of California developed a discrete multifunctional sensor that simultaneously measures temperature, acceleration, pressure and strain (TAPS) for IC engine, geothermal, and power generation applications. This multifunctional TAPS sensor has been built in silicon carbide (SiC) and includes single parameter MEMS sensors such as resonant strain gauges, resonant tuning forks, accelerometers and temperature sensors all fabricated in the same chip and integrated with, high temperature electronics on a single SiC chip. The TAPS sensor has been designed to work at temperatures up to 600 ℃, pressures up to ~ 7 Mpa, high g-shock and corrosive and oxidizing harsh environments [30].

Abdolreza Rashidi Mohammadi at the University of British Columbia developed a discrete multifunctional MEMS sensor that measures pressure using a Silicon-based MEMS capacitive sensor and temperature using an platinum RTD. [31]. Top view of the sensor is shown in Figure 2-5. To compensate for thermal effects in the capacitive pressure sensor, an additional reference pressure sensor with a fixed diaphragm was added to the silicon chip. For chemical protection, the final device was embedded in epoxy. The multifunctional sensor was successfully tested up to 170 ℃ and and 2 Mpa inside an environmental test chamber.

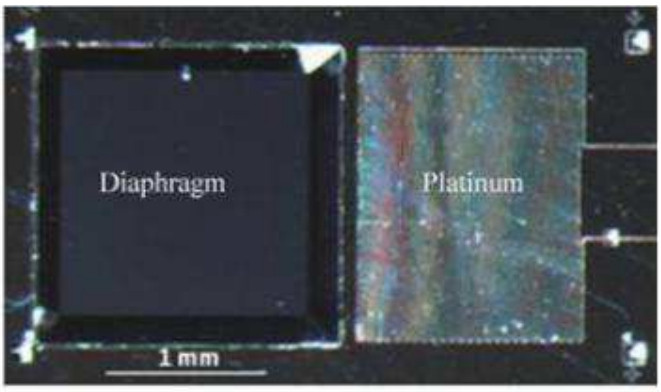

Figure 2-5. Multifunctional MEMS sensor for harh environment applications reported by researchers at the University of British Columbia . Photo modified from [31].

Oiler and Shock [32] reported the design, fabrication, and application of a temperature and electrical conductivity multifunctional sensor arrays for studying the harsh environments of hot springs at Yellowstone National Park. Their design consisted of an array of resistance temperature detector (RTD) and conductivity sensors. The RTD array was conceived as a linearly arranged set of meandering resistors of nickel, while the conductivity sensors were designed as four-point probes with electrode spacing optimized for the range of conductivity of their application, the four-point-probe configuration utilized two outer electrodes to pass a current and two inner electrodes to measure the voltage drop. Both arrays were fabricated on a fused quartz substrate. For protection purposes, an electrically insulating epoxy (H77, Epoxy Technologies) was placed over the solder connections, and the entire array was coated with a second layer of 10 µm Parylene-C to provide additional protection.

Zongyang Zhang et al, [33] packaged an engine oil MEMS pressure sensor inside a metal chamber filled with silicon oil and covered by a corrugated diaphragm. As the silicon oil has many excellent properties, such as smaller temperature and viscosity coefficients, higher heat resistance, good insulation performance, non-corrosive to metal, nontoxic, etc, it has obtained a wide applications as a transmission medium in the area of sensor package. This approach protected their sensor while keeping almost the same pressure stimulus due to the flexibility of the corrugated diaphragm. Although this option accomplishes the objective of protection, the main drawbacks are that it needs expensive packaging equipment, and it is very difficult to keep the silicon oil clean before putting it inside the metal chamber.

Integrated approach

Mertens et al. [34] used the fact that the resonance frequency of a silicon microcantilever is inversely proportional to a temperature increase due to a decrease in Young's modulus of silicon and the elongation of the microcantilever caused by this increase in temperature. The authors also reported a shift in the resonance frequency mainly due to varying damping effect at different ambient pressures.

More recently Najafi et al. [35] developed a multifunctional sensor for simultaneous measurement of pressure and temperature. The design includes elastic membranes and bi-layer beams as pressure and temperature sensing bodies, respectively, and capacitance readout for transduction. The bi-layer beams are placed such that their out-of-plane displacements due to different coefficients of thermal expansion change the capacitances between two sets of electrodes. Finite element simulations and post-processing results verify the applicability of the design technique proposed by Najafi in the measurement of pressures up to 1 Mpa and temperature changes up to 250 °C. Later on, the same research group developed a multifunctional sensor based on a multifunctional membrane with a step located in the middle, which responds simultaneously to both pressure and temperature variations [23]. Their new design uses standard membrane-based pressure and thermostatic-based temperature sensing principles found in MEMS devices and outputs two capacitance values. Although the sensor was fabricated to prototype level and through simulations and experiments functionality turned out, a final design requires the manufacture of the membrane in Silicon Carbide, a material whose manufacturing process is highly expensive.

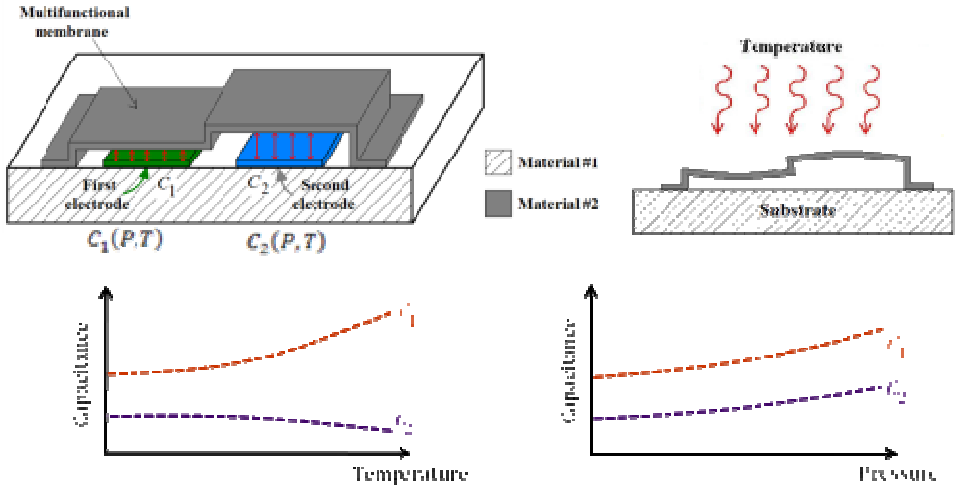

Figure 2-6. Bi-material pressure-temperature sensitive membrane proposed by Najafi et al. [23].

Chapter 3

Multifunctional Sensor system design

This chapter first presents the working conditions found inside the wheel cylinder of the EHB. The design requirements for the new multifunctional MEMS sensor are then defined and followed by a detail explanation of the fabrication process.

3.1 Working Conditions

Sensor location

In current applications of EHB systems, the pressure sensor is located in the main cylinder and from this position the pressure of the complete brake system is monitored and controlled. Therefore, one pressure sensor is more than enough to control the pressure of the system (refer to Fig 3-1).

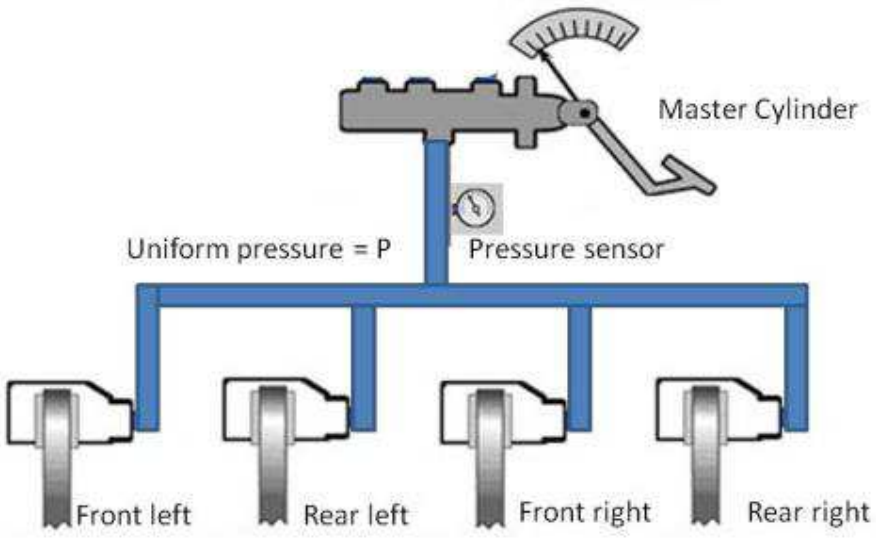

Figure 3-1. Conceptual diagram of current brake systems

As it was described in section 1.2, for our application the sensor system will be part of an EHB system with differential pressure braking capacities. Each wheel cylinder will receive an independent pressure from the other wheel cylinders. Moreover, as each wheel cylinder will have a different pressure this will cause a different temperature in each sub-system, mainly because the thermal interaction between the brake fluid and the caliper will be different in each case, refer to Figure 1-1 that shows a conceptual diagram of this new system. For this reason, is imperative to

have a pressure and a temperature sensor per wheel cylinder, and the location of this sensor system should be as close as possible to the wheel cylinder where the higher temperature is present [2] [3].

Operational requirements

The brake pressure at the EHB system goes up when the driver increases the force exerted on the pedal, stays constant while he/she holds the pedal, and finally drops when the brake pedal is released. During these phases, the pressure can reach up to 4 Mpa (580 psi). Figure 3-2 shows the pressure profile of the EHB system. In the EHB system used for this application, an actuator is used to change the trapped oil volume inside the caliper cylinder directly to control the brake pressure. Each wheel has an actuator that is separate from the other wheels, thus making it possible to control the braking force of each wheel independently. The trapped braking oil in the caliper cylinder is used to transfer force into pressure, and to amplify braking force. It works because liquids are not appreciably compressible (in their natural state the component molecules do not have internal voids and the molecules pack together well, so bulk forces are directly transferred to compress the fluid's chemical bonds).

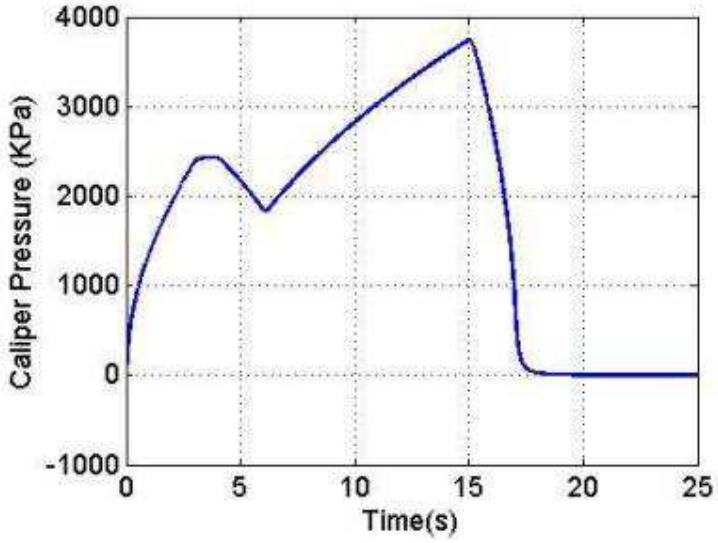

Figure 3-2. A typical pressure profile of an Electro-Hydraulic Brake System extracted from [36].

These pressure conditions inside the wheel cylinder take place in an alkaline chemical environment with a pH ~11 are due primarily to the glycol ether based composition of the brake fluid. Heat generated under braking, especially under heavier breaking or prolonged breaking, may affect the brake fluid that can only work if it is liquid and not so hot that it has become vapor. In this operating condition, the brake fluid is subjected to very high temperatures,

especially in the wheel cylinders. Figure 1-3 shows the typical temperature profile on one brake system [2]. Figure 3-3 displays the detailed temperature profile obtained from Figure 3-4.

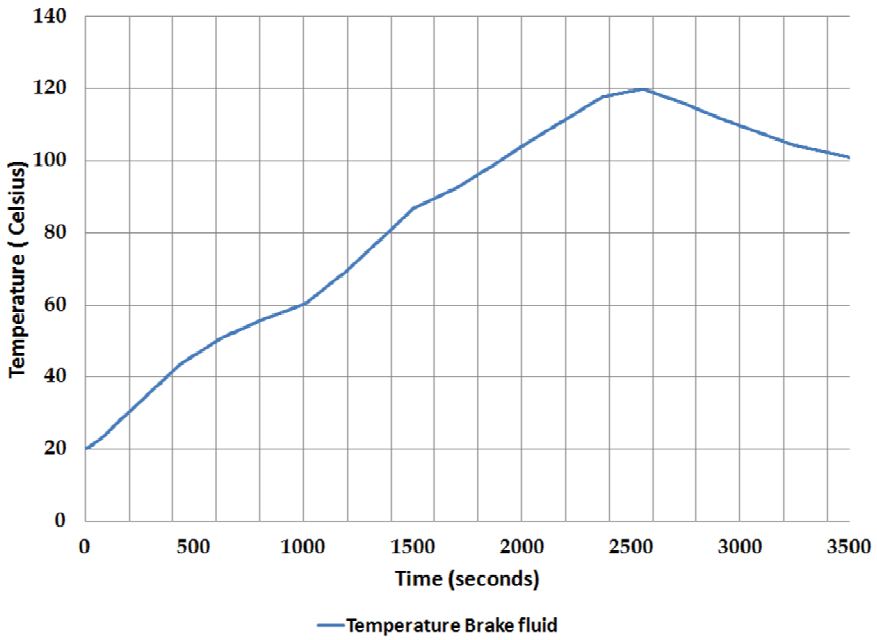

Figure 3-3. The temperature profile of the wheel cylinder on an EHBS modified from [2].

Considering that the pressure inside the wheel cylinder is the same due to the incompressibility of the brake fluid, as was described before, and that the temperature does not have a spatial gradient due to the high conductivity of the wheel cylinder material and the very large contact area between the fluid and the wheel cylinder [2], it is possible to use a discrete approach using two different and independent MEMS transducers close to each other and in the same packaging. This approach will permit evaluate the concept of having two sensors at the same substrate, and in future projects joint both sensors at the same chip. Table 3-1 shows the summary of the working conditions of the sensor system.

Table 3-1. Working conditions of the sensor

Parameter	Range
Pressure	0.4 to 4.0 Mpa (50-580 psi)
Temperature	-20 to 120 ºC
pH	~11

3.2 Development of the sensor system

3.2.1 Requirements

Monitoring of the brake systems is typically taken at the main cylinder leading to one general pressure signal for all the brake system. In consideration of the formerly discussed, the presumptive use of commercial sensors will cause to have eight different sensors and eight different sensor penetrations in the brake system resulting in big disturbances to the system. To lessen the intrusion caused by the sensors, and to obtain the temperature and pressure signals at the same time, the best approach is to use Micro Electro Mechanical System (MEMS) sensors. A mechatronics approach was used to integrate with one packaging two different MEMS sensor, the pressure, and the temperature one. The sensor system must be: (1) compatible with the current sensors fitting used in hydraulic systems ; (2) support the harsh environment of the brake system ; (3) capable to obtain the pressure and the temperature readings using just one interface; (4) compatible with automotive electrical conditions ; and (5) low cost.

3.2.2 Selection of the sensors

MEMS silicon-based pressure sensors are commercially available for many applications such as automotive, biomedical, and aerospace [16]. Piezoresistive MEMS pressure sensors are very common and have been chosen for this application over MEMS capacitive sensors due to their robustness, linearity, simple measurement circuitry and immunity to electromagnetic noise. However, difficulties in temperature compensation and fabrication control affect sensor offset and performance. Thus, a MEMS temperature sensor collocated next to the MEMS pressure sensor should provide temperature readings as well as the means for temperature compensation. For this project, a unpackaged commercial MEMS piezoresistive pressure sensor manufactured by BCM sensors was selected, refer to figure 3-4. The model SE103 is designed for absolute pressure measurements (refer to figure 3-5). As a piezoresistive sensor die, the SE103 is based on MEMS technology and was purchased unpackaged or in a “bare-die” configuration. The die has a footprint of 2.45 mm x 2.45 mm for the pressure range used in this project. The SE103 die has a silicon-on-glass structure that permits to create a vacuum gauge cavity and it is offered in with five solder pads for both adjustment and temperature compensation of zero offsets. The SE103 have a time response of ≤ 2 ms.

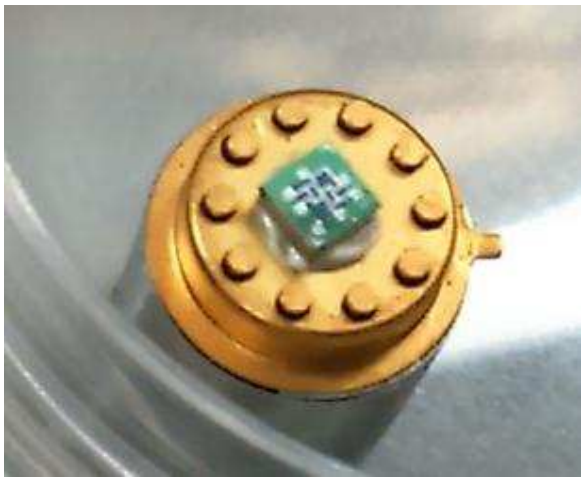

Figure 3-4. BCM MEMS Pressure Sensor bonded to the Transistor Outline (TO) header.

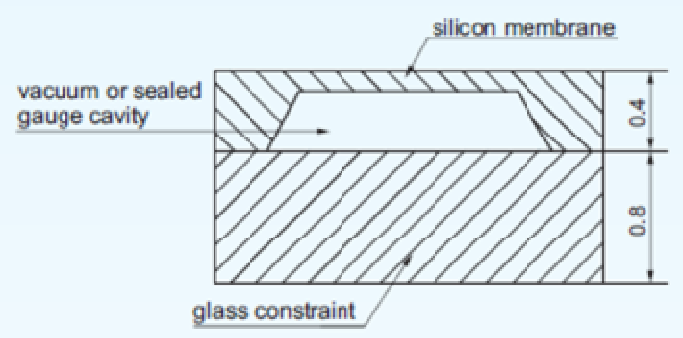

Figure 3-5. Schematic cross section of the BCM sensor, glass constraint for absolute pressure measurements extracted from [37].

The temperature measurement is performed using a commercial resistance temperature detector (RTD) manufactured by US Sensor (see Figure 3.6). This type of sensor measures temperature by correlating the resistance of the RTD element with temperature and it is known to be one of the most accurate and used MEMS temperature sensors [27]. Not only does it provide good accuracy, but it also provides excellent stability and repeatability, while having a time response of 1 second.

Figure 3-6. Platinum RTD sensor use for the manufacturing of the proposed MEMS sensor system

3.2.3 Packaging and chemical resistance to the harsh environment

To prevent sensor malfunction or degradation due to chemical attack, MEMS devices exposed to chemical environmental conditions must be protected from the media with a protective coating applied to the exposed area [38]. For our application, we need to consider that the brake fluid is hygroscopic - that means it attracts and soaks up water. As it was mentioned before, while this directly increases the boiling point of the brake fluid and reduces the viscosity of the brake fluid, the humidity levels in the brake fluid can damage the sensor systems, especially the wire bonds connections. Parylene coating has been extensively used in electronic components [39]. Several types of Parylene materials with slightly different chemical structures are available for various applications. The benefits of Parylene coating include room temperature conformal deposition, pinhole-free, excellent adhesion to most substrates, high moisture impermeability, chemical resistance and it has a maximum operating temperature of 225°C at oxygen free environments. Parylene was used as a coating material for this project at high-temperature operation in alkaline conditions. The Parylene layer was designed to offer (1) dielectric protection; (2) protection of the wire bonding (electrical connections); (3) protection from the corrosive medium (brake fluid); and (4) protection from the moisture in the brake fluid.

3.3 Fabrication process

The prototype was fabricated gluing both sensors on the same substrate. A commercial Transistor Outline (TO) Header was selected and purchased from Spectrum Semiconductors (refer to Figure 3-7). This TO Header includes the lead pins needed to make the electrical connections to the sensors. While the TO header makes sure that the encapsulated components are provided with power, the upper surface permit the interaction of the MEMS sensors with the sensing media and provides a mechanical basis for the installation of the MEMS sensors while at the same time

providing power to the encapsulated components with the aid of pins. Humidity, in particular, can cause the MEMS sensors to corrode rapidly, leading to failure of the entire system. This is why these TO header components require reliable and permanent protection, a topic that was explored deeply before in this thesis.

Figure 3-7 TO Header-39 manufactured by ELECTROVAC used as the substrate for the MEMS sensor system.

Figure 3-8 shows the MEMS pressure sensor and the RTD sensor glued to the surface of the TO Header using ABLEBOND® 84-1LMI, a die attach adhesive designed for microelectronic chip bonding. This adhesive is resistant enough to support the specified high pressure and high temperature. To cured, the adhesive was exposed to a thermal profile of 60°C for one hour and 130°C for two hours.

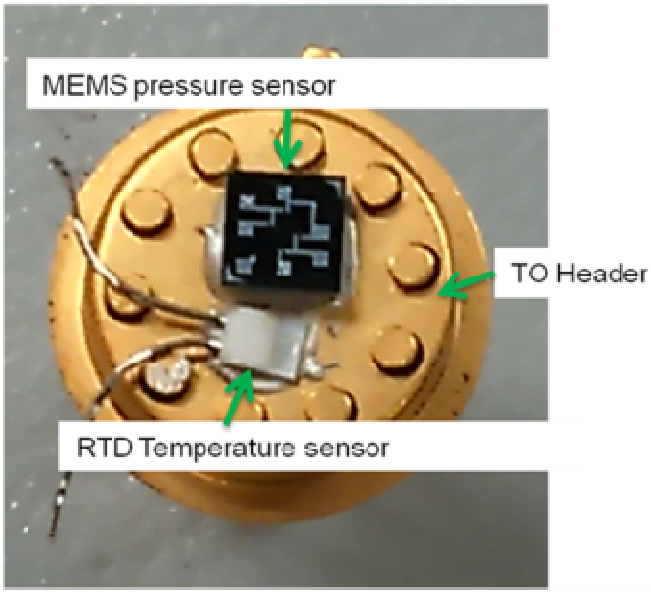

Figure 3-8. TO substrate showing the MEMS and the RTD sensor glued on it

Once the adhesive is cured, the leads of the RTD were soldered to the TO Header lead pins using paste SynTECH-LF Lead-Free. The MEMS pressure sensor was then wire bonded to its respective TO lead wires. The MEMS pressure sensor is based on an open Wheatstone bridge; therefore, five connections are needed to power up the sensor and obtained the signal. The wire bonded was done according to the diagram of the MEMS sensor; Figure 3-9 shows the terminal pads LAYOUT of the MEMS sensor.

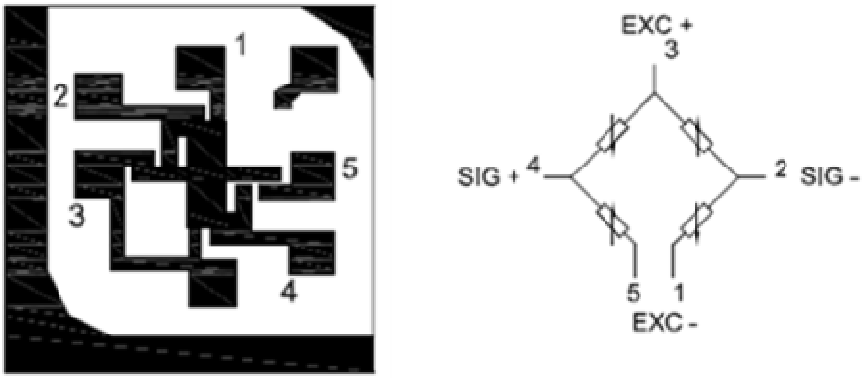

Figure 3-9 Terminal pads Layout of the MEMS pressure sensor extracted from [36].

The wire bonding process was done at the Toronto Nanofabrication Centre (TNFC) of the University of Toronto using a TPT HB16 Wire Bonder. Figure 3-10 shows the MEMS piezoresistive pressure sensor electrically connected to the TO header through wire bonding.

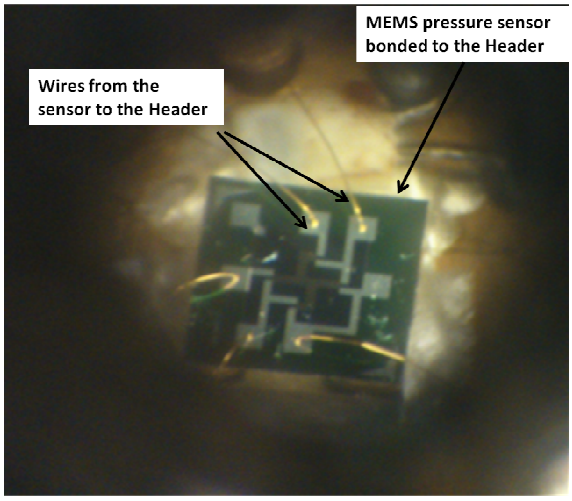

Figure 3-10 MEMS piezoresistive pressure sensor wire bonded to the TO header.

After the connections were finished, the parylene protection layer was deposited over the sensors using a vapor deposition process at room temperature. A Parylene coater, model SCS 2010 (Specialty Coating Systems, IN) was used at the Nanofabrication Centre of the University of Toronto to coat packages with 4-μm thick Parylene C films. The coater has a tolerance of +/- 10 % of specified thickness. For covering a 1μm-thick film, 1.55 g Parylene material was used. The material was heated at 150°C under a vacuum (1 Torr), and the Parylene started to vaporize. The gaseous material was then pyrolyzed at 680°C under a vacuum (0.5 Torr) in a furnace to form Parylene monomers. The monomers were then polymerized at room temperature under 50 mTorr as a conformal coating on the sensor in a stainless steel deposition chamber [40]. The three-step deposition process includes: (1) vaporization of solid dimmers to gaseous ones; (2) pyrolysis of gaseous dimmers to monomers; and (3) Parylene deposition (see Figure 3-11 [41]). One of the advantages of Parylene is that as this is a gaseous monomer that builds from the surface outward. This produces a pinhole free (pinhole free @ .6 micrometer or higher) conformal layer of uniform thickness. Surface tension causing the pulling away of sharp edges, bridging or thin out when conventional coatings are used in the curing process does not occur with the parylene process. Due to the fact that the parylene coating is performed at room temperature, there is no need for a high cure temperature cycle and there is no presence of thermal or mechanical stress. The high flexibility of the coating also prevents the wires from detaching from the pads due to thermal expansion.

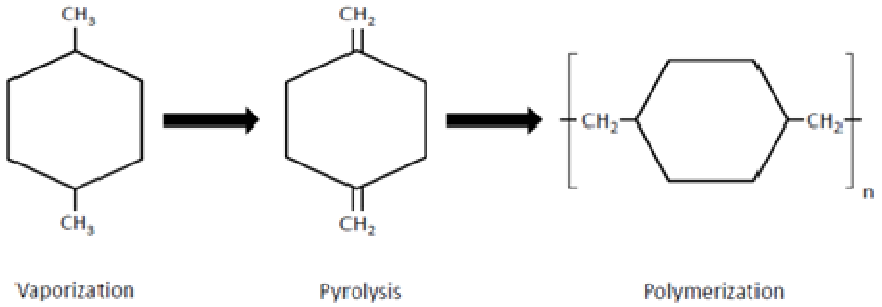

Figure 3-11. Three-Step Vapor Deposition Process of Parylene with chemical chains.

Figure 3-12 shows an schematic of the parylene-covered wire bond chemical process. Being a vapor deposition process, all the surface of the sensor system, including the wire bonds, were covered with an even layer of parylene.

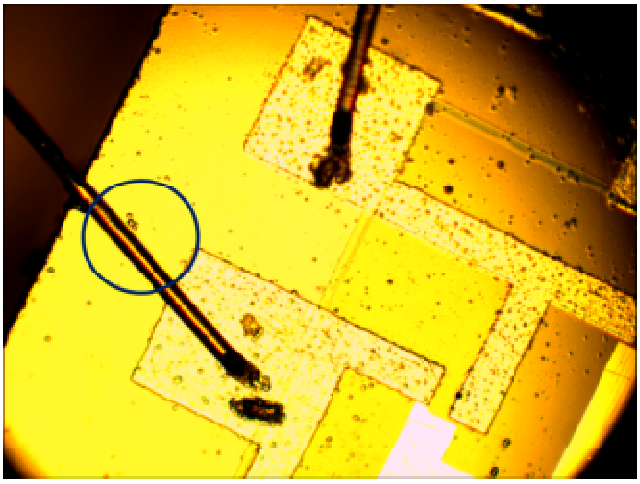

Figure 3-12. Microscopic picture of the sample covered by the parylene layer.

The last packaging step consists of building an interface of the sensor system to the brake system. Such an interface should be compatible with the current fittings of the brake system. For this purpose, a commercial 1/4 18 NPT fitting (Future Hydraulik part M12810-05-04) was customized to be used as an interface and as a metal shell. The TO base and metal shell need to be joined forming a sealed chamber for the sensor system. Several joining process exists to create the sealing ; however, a very important aspect to consider for this step is the temperature that will be reached during the welding process, the integrity of the TO Header and the MEMS sensors should be kept it. Among these methods, resistance welding, micro-brazing, and micro laser welding have been used to join the steel of the metal shell to the KOVAR alloy of the TO substrate [42]. Figure 3-13 shows the metal shell used as an interface with the brake system.

Figure 3-13. Steel case used as last interface with the Brake System (left), Steel case and TO Header subassembly (right).

Different suppliers were evaluated to choose the best option that can guarantee a seal without leaks, which is primordial for the correct performance of the sensors. Figure 3-14 shows the first set of samples welded by the École Polytechnique de Montréal.

Figure 3-14. First set of welded samples made of the Polytechnique of Montreal showing the detail of the poor joint between the TO Header and the metal shell.

The samples were tested on a hydraulic hand pump to evaluate if the welding line can resist up to 580 psi (4 Mpa), which is the biggest pressure of the brake system. These set of samples failed the test at 50 psi, presenting a big leakage. After analyzing the samples and the way that the welding process was performed, further machining of the steel case was needed to seat the header flush inside the steel case. The modification consisted on widening the opening (refer to figure 3-15) and try the micro-laser welding again.

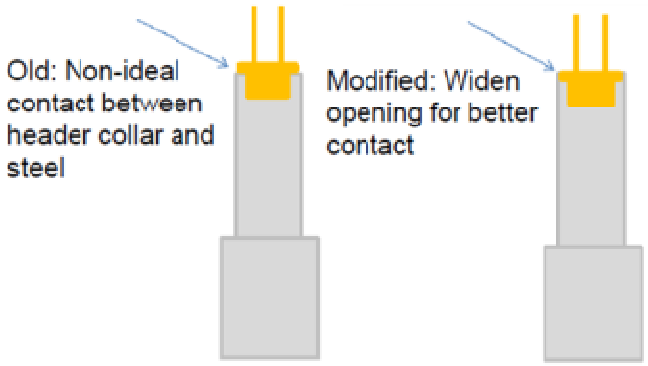

Figure 3-15. Modification of the seating of TO Header and Steel Case to improve the contact area of the sub-assembly.

The second set of samples were tested. However, the samples leaks at 150 and 300 psi respectively (refer to figure 3-16). After these results, two suppliers were contacted to do the welding process (refer to figure 3-17), Grand Valley Specialty Welding at Cambridge Ontario, and Whitfield Welding at Oldcastle Ontario. The sample of Grand Valley Specialty leaks at 400 psi. The sample was analyzed, and some cracks were observed on the welding line of the sample (refer to figure 3-18) while the sample from Whitfield Welding resisted up to 650 psi. However, while the welding line resisted this high pressure, some leaks were observed on the glass section of the TO Header at 480 psi for sample #1 and 520 for sample #2.

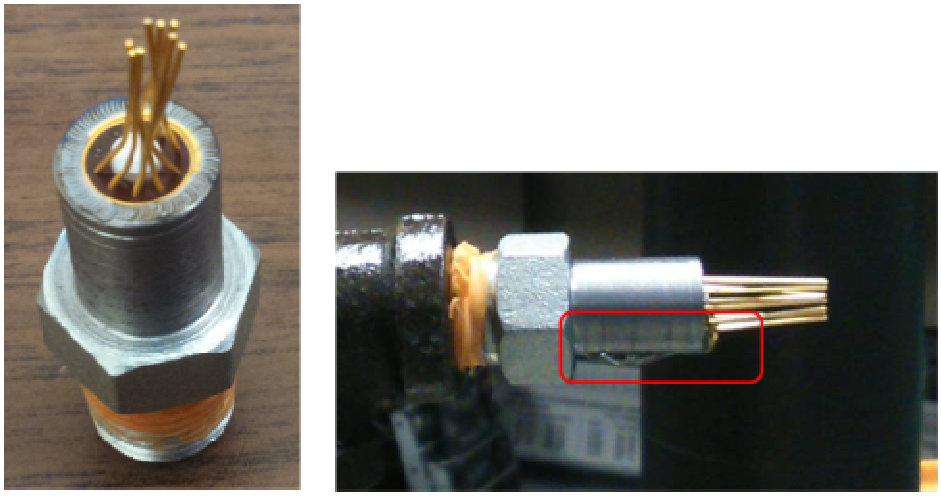

Figure 3-16 Second set of samples from the Polytechnique of Montreal (left), Leak of second trials of samples from the Polytechnique of Montreal(right).

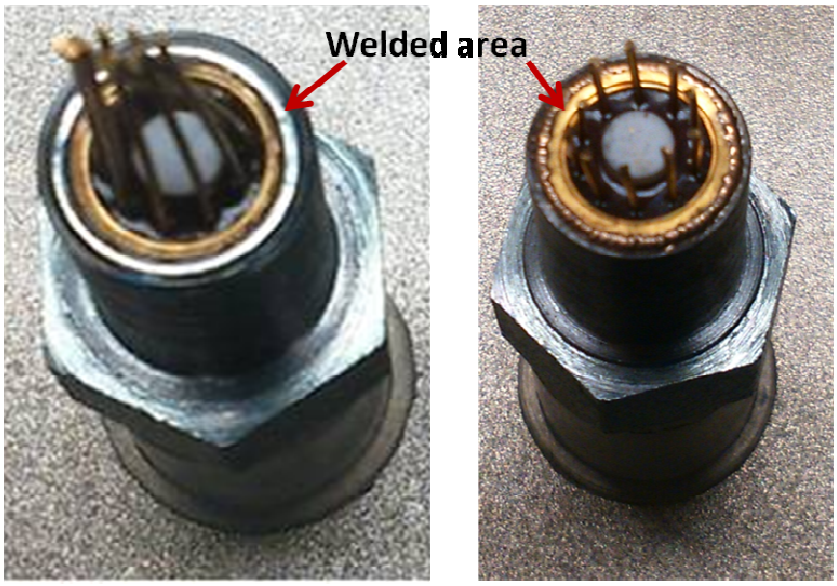

Figure 3-17 Sample from Grand Valley Specialty Welding (left). Sample from Whitfield Welding (right)

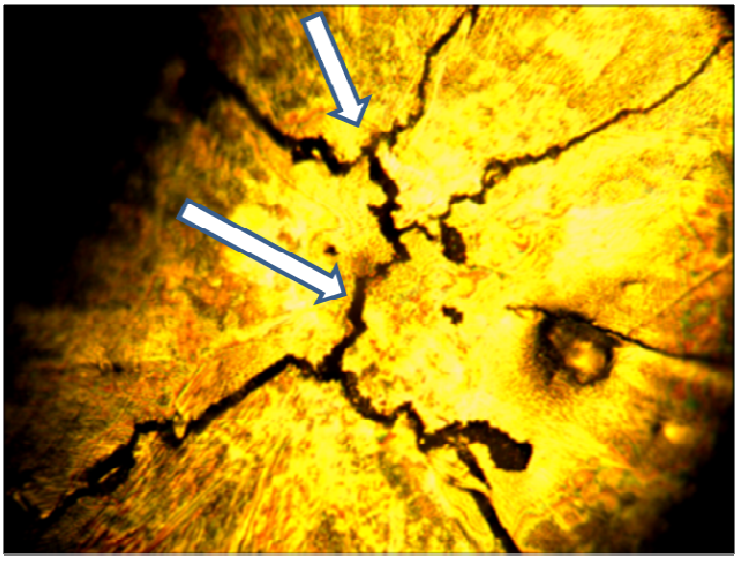

Figure 3-18 Crack on welding line of the sample from Grand Valley Specialty Welding observed under Microscope.

The process used by Whitfield Welding was micro-brazing. The joint was filled with silicon bronze wire. It is important to comment that the minimum temperature reached in the melt pool for the alloy to flow was about 1100 °C, but this would only be in the vicinity of the laser spot

that is under a millimeter in diameter, and only for a small fraction of a second (~5-10 ms). So the temperature that the device reached (away from the joint) was not much higher than room temperature. The micro-brazing process resulted in small heat-affected zones and ensured that critical components were unharmed. The figure below shows the schematic of the final packaged sensor system.

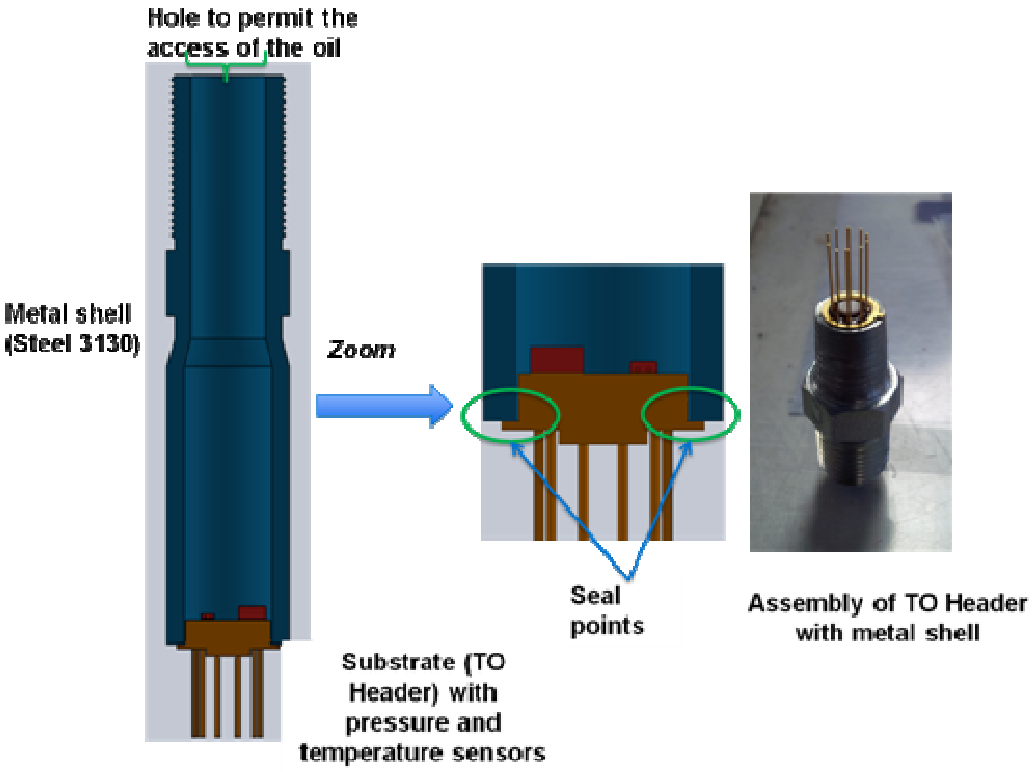

Figure 3-19 Schematic of the final packaging (left); excerpt showing details of the sealing points (center); and physical sample (right).

After the welding process, the samples were inspected under a microscope to ensure that the MEMS sensor was not damaged during the welding process, in particular the wire bonds were closely inspected as they are the most delicate parts of the MEMS sensor. Figures 3-20 and 3-21 show the wire bonds properly connected to the MEMS pressure sensor.

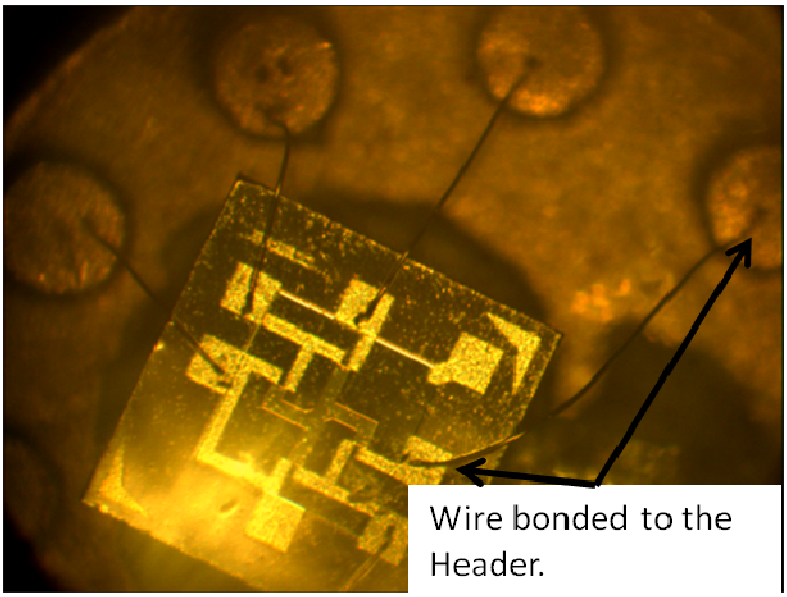

Figure 3-20. Bond Pads and wires on the MEMS pressure sensor of sample #2 after the micro-brazing welding process

After inspection, wires were soldered to the TO Header pins to facilitate further testing. Figure 3-21 shows the sample # 1 ready to be tested.

Figure 3-21 Sample # 1, fully connected and ready to be tested.

Chapter 4

Modeling

This chapter investigates different performance characteristics of the proposed multifunctional MEMS sensor through the use of numerical modeling. While the adhesion of parylene described in previous chapters will protect the sensor system from the conditions of the brake fluid, this also will affect its performance. Adding an extra layer of polymer on the surface of the RTD sensor will create an additional thermal mass that will be located between the sensing media and the RTD. This potentially can affect the response time and sensitivity of the sensor, and should be considered for the final sensor system design. Concerning the pressure sensor, the adhesion of the parylene over the deflective diaphragm, will make it more rigid, and may cause a dampening effect, this directly will affect the stress response of the diaphragm and hence the sensor sensitivity. The sensor system was modeled to account for the impact of the packaging on the performance of the sensor. The numerical modeling is based on finite element (FE) analysis and it is performed using the commercial FE software COMSOL ©.

4.1 Thermal modeling

The FE model developed in this section is used for the analysis of the effect of the packaging, punctually the parylene layer, on the performance of the Resistance Temperature Detector (RTD) in terms of loss of sensitivity, offset in the signal, etc. The sensor system considered in the following simulations consists of:

- A steel chamber that works as the last interface with the brake system and creates a sealed chamber where the sensors and substrate will be.
- A TO Header made of KOVAR; that works as the substrate for the MEMS Pressure sensor and the RTD sensor.
- The RTD Sensor, which is the central element of the analysis.
- A Parylene layer, which works as a protective layer.

Figure 4-1 shows the schematic diagram of the packaging.

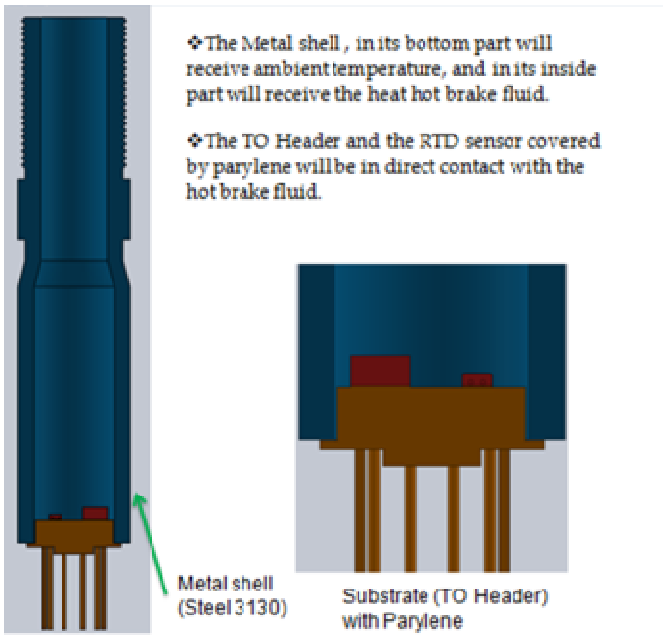

Figure 4-1 Schematic of the final packaging with the RTD, TO Header and Steel Case.

To obtain the effect of the packaging on the performance of the sensor, we need to get the final transfer function that describes the behavior of the RTD sensor. Resistance thermometers, also called Resistance Temperature Detectors (RTDs), are sensors used to measure temperature by correlating the resistance of the RTD sensing element, usually made of metal, with temperarture. The material has a predictable change in resistance as the temperature changes, and it is this predictable change that is used to determine temperature. Figure 4-2 shows the conceptual diagram of the transfer function of the RTD sensor.

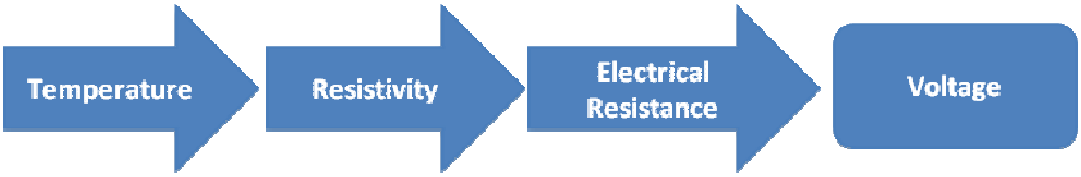

Figure 4-2 General transfer function of an RTD sensor.

For this thermal model, as this is a commercial RTD sensor and not a fabricated one, the model will not focus on the change of the resistivity of platinum because this property is not changing due to the packaging effect, the model is going to concentrate on the change of electrical resistance on the platinum when constant current is applied and the sensor is stimulated by the sensing media.

Two distinct polynomial equations describe a platinum RTD transfer function [27] ,[43]: one for temperatures below 0ºC and another for temperatures above 0 ºC.

The equation for $t \leq 0^oC$ is

$$\boldsymbol{R_{RTD}(t) = R_0(1 + At + Bt^2 + C(t - 100^oC)t^3} \quad (1)$$

The equation for $t \geq 0^oC$ is

$$\boldsymbol{R_{RTD}(t) = R_0(1 + At + Bt^2)} \quad (2)$$

In equations (1) and (2):

t is RTD temperature (ºC); $R_{RTD}(t)$ is the RTD resistance as a function of RTD temperature (t) ; R_0 is the RTD resistance at 0 ºC ; $A = 3.9083 \times 10^{-3}$°C ; $B = -5.775 \times 10^{-7}$°C, and $C = -4.183 \times 10^{-12}$°C.

For this first model, we will consider a constant current of 1 mamp, and the resistance vs. temperature curve given by the supplier. In normal conditions, the temperature (t) that the RTD would read, would be the one that is on its surface; however, with the Parylene layer covering the RTD sensor, the temperature that the RTD would read could be different. To understand the temperature that the RTD will read, a thermal analysis is needed in the sensor system. The sensor system will have two inputs:

- The Brake fluid temperature profile coming from the brake system (refer to figure 3-5).
- The transfer of temperature coming from the ambient temperature through the steel shell.

Using the Heat equation on the domain described by the sensor system is possible to obtain the temperature profile that would reach the RTD. However, considering this is a 3D problem an analytical solution is not feasible due to the geometry of the elements. An approximation method such as Finite element method is needed to apply the Fourier law to the domain. The analysis will be applied to the domain considering a time-dependent solution, that is, not a steady state.

$$\rho C_p \frac{\partial T_2}{\partial t} + \rho C_p u \cdot \nabla T_2 = \nabla \cdot (k \nabla T_2) + Q \quad (3)$$

C_p is the specific heat capacity, $C_p = \frac{J}{kg * K}$

ρ is the density.

k is the conductivity.

$\frac{\partial T_2}{\partial t}$ is the partial derivative of the temperature with respect to time

Q is the internal heat source.

Now that the PDE of heat conduction has been set, we need to include the boundary conditions, that, for a given point in time, specify the behavior of the solution on the border of the domain.

$$T(x,t) = T_w(x,t)$$

The temperature on the boundary of the body is prescribed by $T(x,t)$,= $T_w(x,t)$, where T_w is a known function. In our case there are two different boundary conditions, the temperature profile of the brake fluid, and the temperature profile of the packaging. Instead of considering the TO Header to a constant ambient temperature in its external area, the metal shell was considered in the packaging. The steel case would be in contact with the TO Header, and through its thickness the ambient temperature will be conducted to the TO Header and after that to the RTD Sensor (Figure 4-3, showing the cross section).

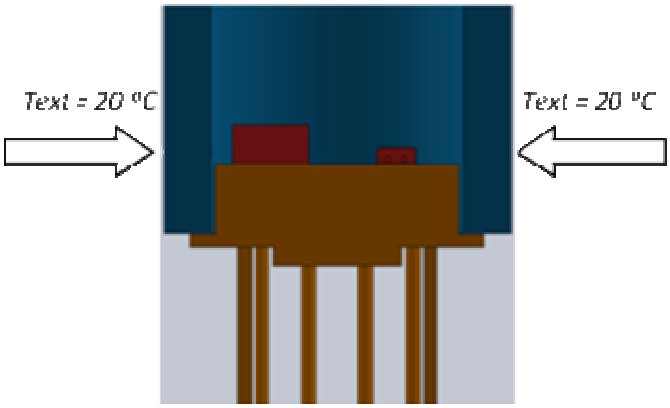

Figure 4-3. Cross section of the metal shell in contact with the TO Header.

To do this simulation, a geometric model of the real packaging was designed. The Geometric model consists of 4 main parts : The TO Header, which works as a substrate for the RTD; the RTD sensor, in this case the RTD sensor is considered just as one block of ceramic material; the parylene layer, which is 4 um thickness and is applied to the TO header and RTD surfaces; the steel shell, which dimensions are taking from the real one (refer to Figure 4-4)

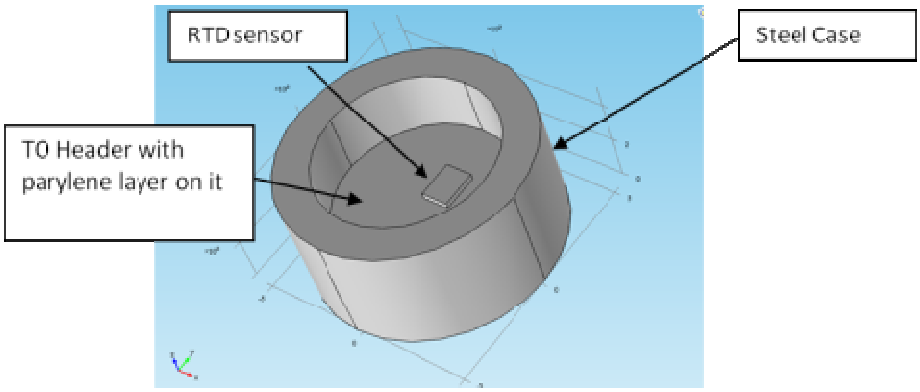

Figure 4-4 Geometric model of the packaging

In this modeling, the RTD is not considered as a complex element (that is a ceramic layer, a platinum layer, a glass layer, and a parylene layer) instead just like a solid block of ceramic material , which is the substrate material of the RTD sensor. This is due to two main reasons:

- The purpose of this model is obtained the thermal input to the TO Header, to apply this thermal input to the model of the RTD.
- Includes the RTD and its complete geometry will cause a very long time simulation, and the meshing will be cumbersome leading to a not reliable result.

Figure 4-5 shows the boundary conditions applied to the packaging.

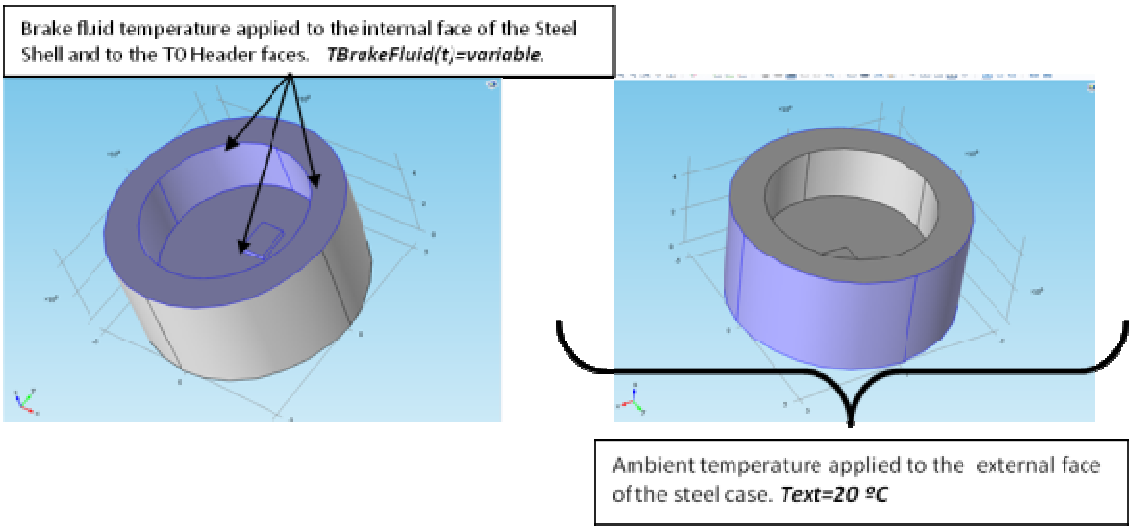

Figure 4-5 Boundary Conditions applied to the Packaging Model

Once that the geometry, materials, and boundary conditions have been defined, the discretization of the model was performed. The physics-controlled mesh sequence of COMSOL was used. This tool select the meshing according to the physics involved in the problem. Figure 4-6 shows the meshing of the geometry.

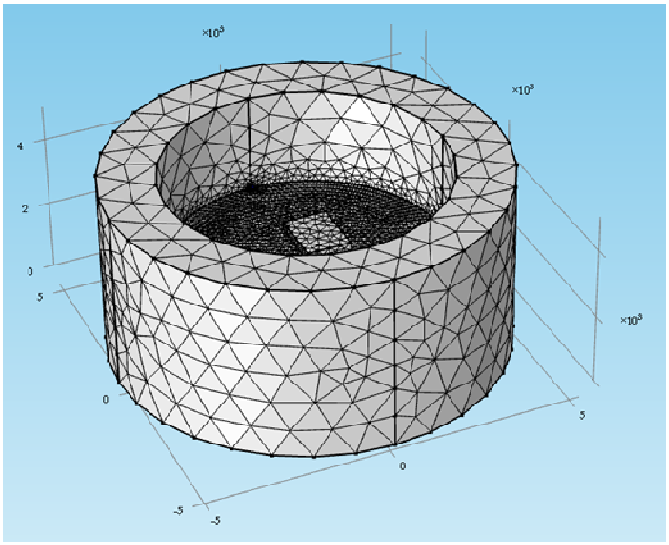

Figure 4-6.- Discretization scheme of the TO Header - Steel case model.

Using the Fourier law with a time-dependent solution to the model, temperature dependent properties and the boundary conditions as shown in pages 34 to 36, the following temperature profile is obtained on the TO Header lateral faces, figure 4-7. The temperature obtained in the simulation of the packaging will be used in the RTD Model as a boundary condition applied to the substrate instead of a constant temperature, this will lead to a more realistic result.

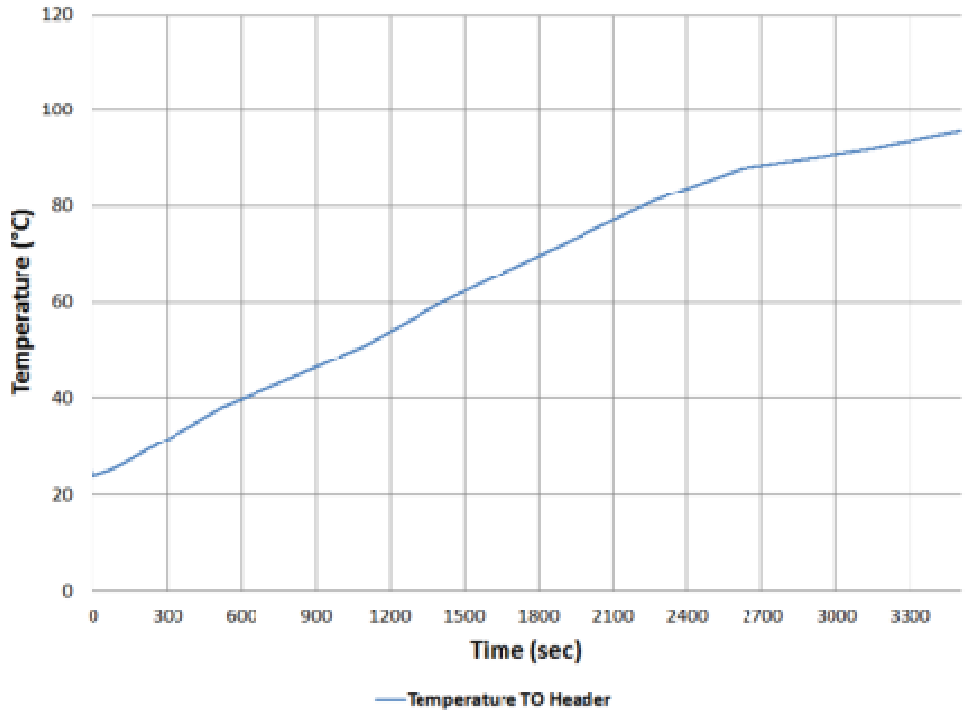

Figure 4-7 Temperature of the lateral face of the TO Header

Modeling of the RTD sensor

In each wheel cylinder, the temperature does not have a gradient. Overall the brake fluid in the wheel cylinder the temperature is the same [2]. For the sake of the modeling, the geometry of the RTD was built in COMSOL itself, and not exported from other software, this would not affect the model (refer to Figure 4-8).

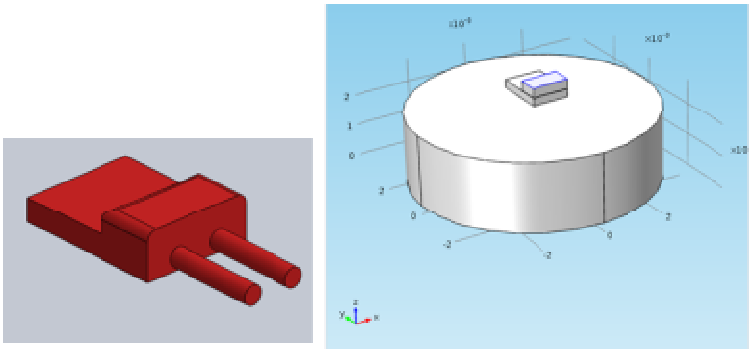

Figure 4-8 RTD Sensor Model in Solidworks and Model in COMSOL including the TO Header

The dimensions of the RTD were modeled considering the supplier drawing. However, as the final geometry of the RTD is a design information protected by the supplier, the drawing does not give

details about the dimension of the Platinum layer, instead this data was obtained averaging the value of several papers about design of RTD [28], [39], [44]. The values at the literature for the thickness of the platinum layer vary from 0.8 to 1.15 µm, for the modeling, a value of 1 µm was used. The model assumes that the final geometry of the platinum layer (which is unknown) is planar (see figure 4-9).

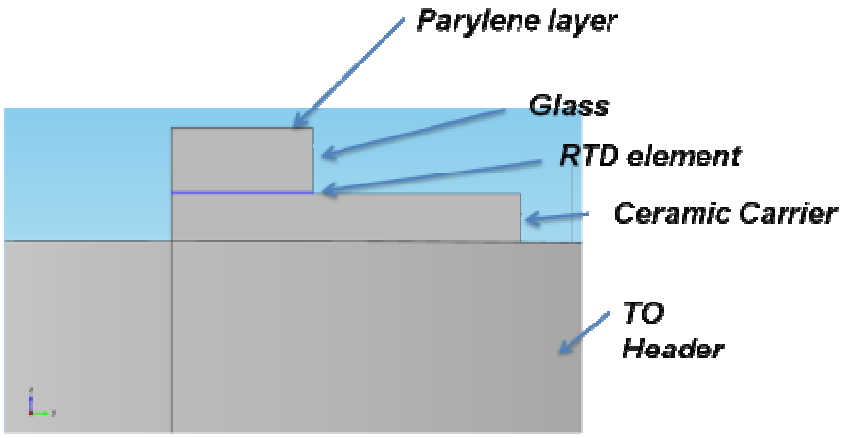

Figure 4-9 Cross section view of the Model.

Following the steps of the previous modeling, the RTD sensor was modeled with the following boundary conditions (see figure 4-10).

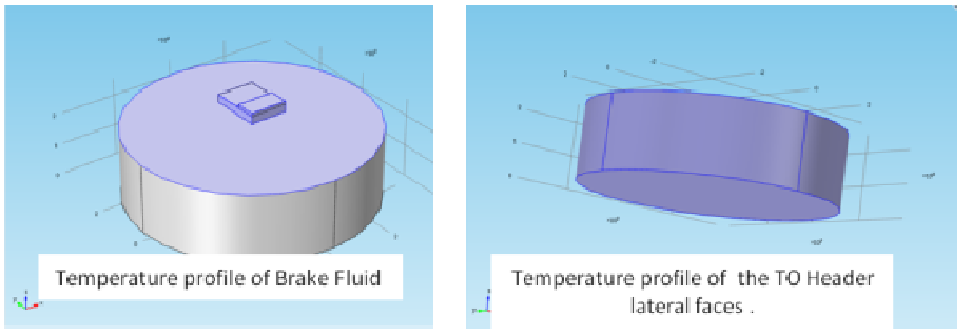

Figure 4-10. Boundary conditions of the substrate with the RTD sensor.

The physics-controlled mesh sequence of COMSOL was used to define the discretization of the model. Figure 4-11 shows the meshing of the geometry.

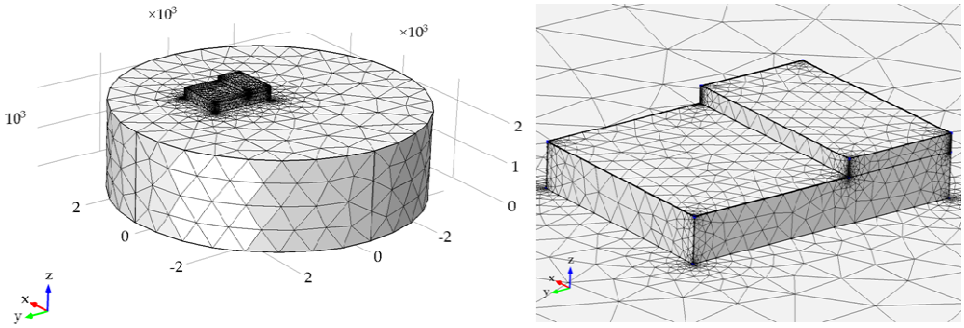

Figure 4-11.- Discretization of the RTD Model(left), detail of the RTD sensor (right).

After applying the Fourier law with a time-dependent solution, Figure 4-12 shows the temperature of the RTD sensor compared with the temperature of the brake fluid with a 4 um parylene layer applied over the RTD sensor. Different element sizes were used on this simulation to obtain an accurate result and validate the meshing. Table 4-1 summarizes the elements used on the RTD model.

Table 4-1.- Summary of elements used on the RTD model.

Property	**Value**
Tetrahedral elements	32529
Pyramid elements	0
Prism elements	0
Hexahedral elements	0
Triangular elements	9249
Quadrilateral elements	0
Edge elements	1238
Vertex elements	64

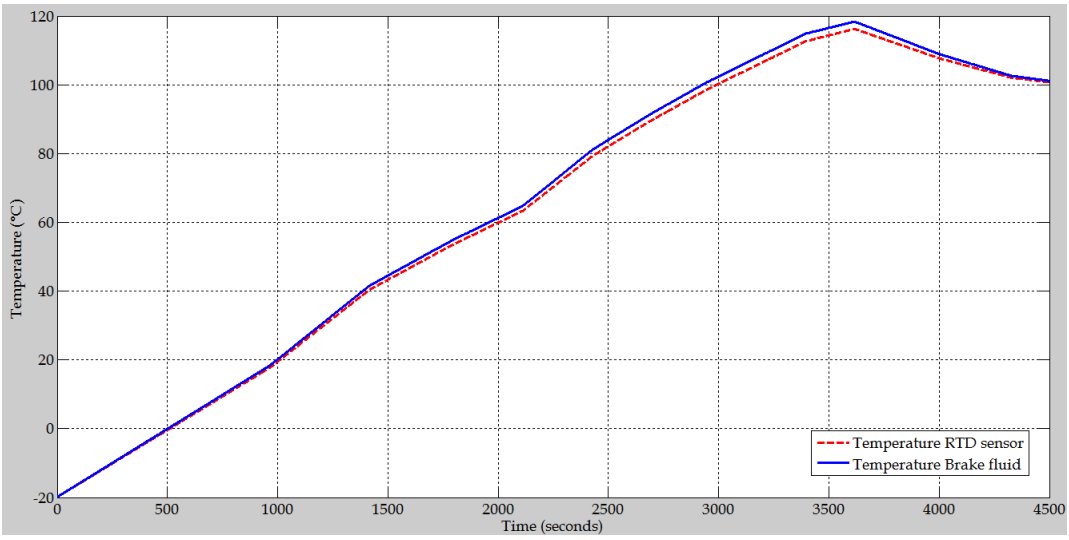

Figure 4-12 Brake fluid temperature versus RTD Temperature.

Analyzing the figures 4-12 and 4-13, it can be observed that the maximum temperature difference between the brake fluid temperature and the temperature that the RTD will read is 1.7 ºC. According to the simulation result, this is located close to the point of highest temperature during the braking cycle. We can conclude that the effect of the parylene layer is minimum, mainly because the rate of temperature increase is very slow, on this application is 0.03 $^{\circ C}/_{sec}$.

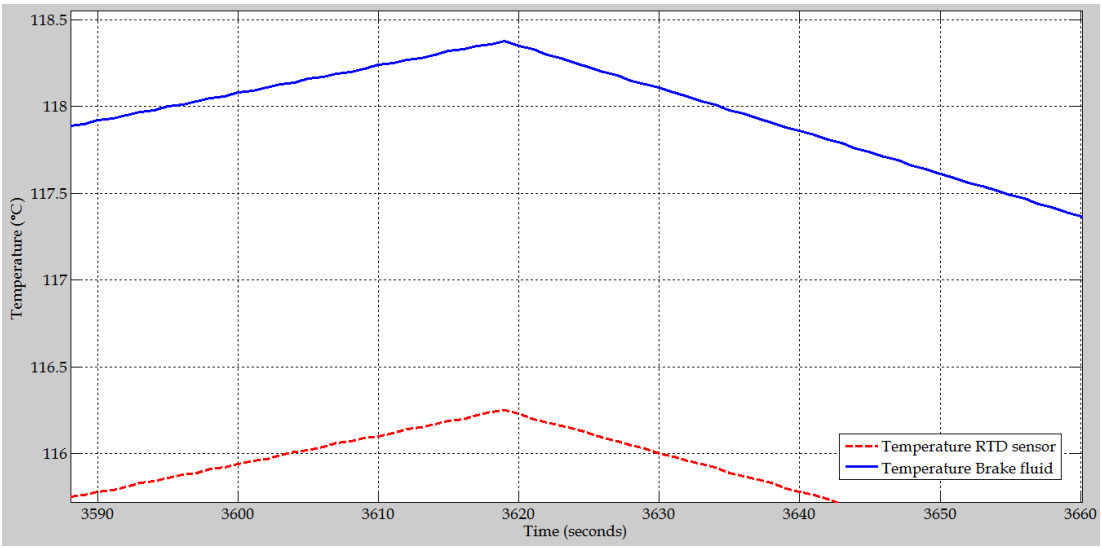

Figure 4-13 Maximum difference of temperature between the brake fluid temperature and the sensor system with a four um parylene protection layer.

Once that we have the temperature profile that the RTD sensor will read considering the parylene layer, we can calculate the output of the sensor and compared this output with the output of a no

protected sensor. Using Equation 1 and 2 and a constant current of 1 mAmp we can obtain the characteristic curve of the commercial RTD. Figure 4-14 shows this curve.

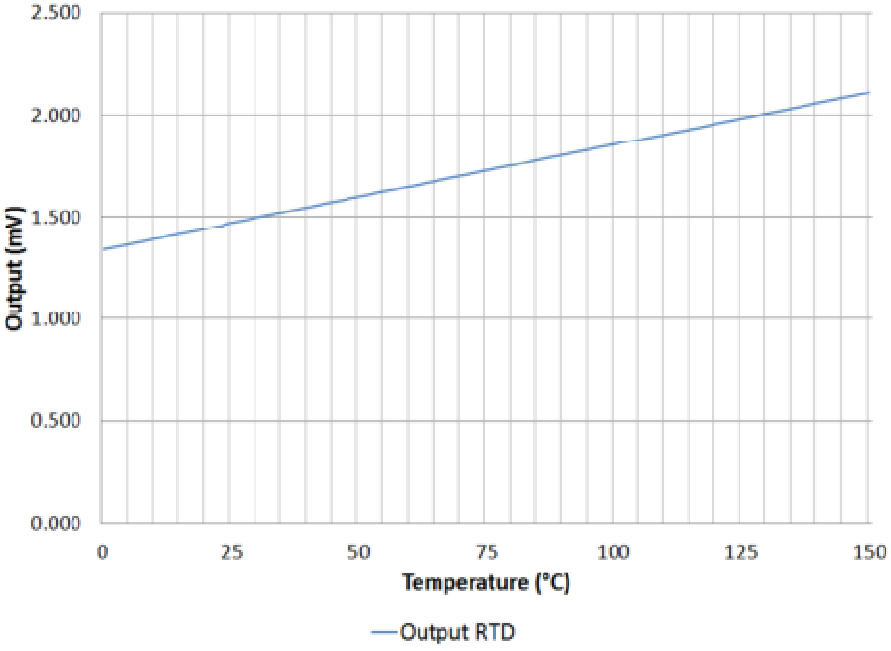

Figure 4-14 Voltage vs Temperature curve, at 1 amp of constant current.

As was described on page 33, the resistivity of the sensor is not affected by the parylene layer, the direct effect in the performance of the sensor is in the fact that the temperature that the sensor will read without reaching steady state will be slightly different that the one that the brake fluid will have. Figure 4-15 shows the difference in the output between the RTD with and without packaging effect from 20 to 120 °C.

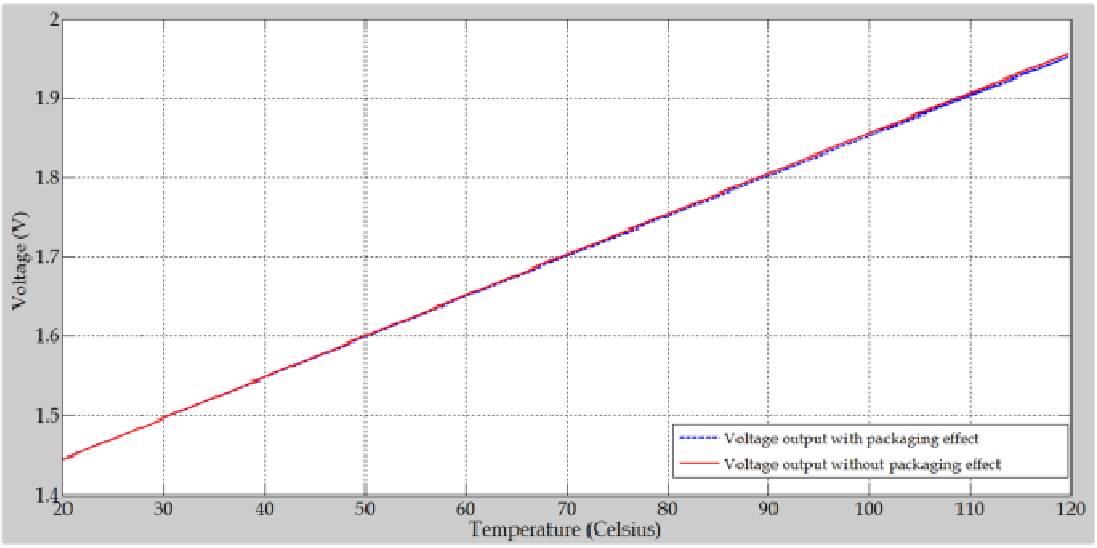

Figure 4-15 Voltage output with and without Parylene vs. Temperature, from 0 to 120 Celsius

The results of FE numerical simulations in this section provide useful information on the average temperature and temperature variation of different components of the sensor during its working cycle.

4.2 Mechanical modeling

In this section, a FE model is developed for the analysis of the effect or impact of the packaging, punctually the parylene layer, on the performance of the piezoresistive pressure sensor in terms of: loss of sensitivity, change in linearity , etc. For the mechanical model, the steps would be very similar to the ones followed by the thermal model:

- Construction of the geometry of the pressure sensor.
- Definition of governing equations.
- Definition of materials and properties.
- Definition of Boundary conditions

For this case, the Piezoresistive MEMS Module of COMSOL Multiphysics ©was used. Figure 4-16 show the conceptual diagram of the principle of the piezoresistive pressure sensor.

Figure 4-16 Principle of a piezoresistive pressure sensor

First, a model of the piezoresistive pressure sensor without Parylene layer will be addressed, and later on one with the Parylene layer. The reason of this is to obtain and understand the complete performance of the sensor without any protection layer, and then have a core model that is possible compare with analytical solutions, such that, that a validation is feasible. Once this is done, the addition of the protection layer is possible, and then perform a comparison of the models and analyze the effect of the protection layer on the performance of the sensor.

Mathematical Analysis

The analysis is done for square shape diaphragm deflection, which is the case of our sensor. In a pressure sensor, the pressure is applied uniformly on top of the diaphragm/plate, normal to the plane of the plate in the z-direction. The governing differential equation for a two-dimensional plate with a uniform pressure load, P, subject to lateral bending can be expressed as [34].

$$D\left[\frac{\partial^4 w}{\partial x^4} + 2\frac{\partial^4 w}{\partial x^2 \partial y^2} + \frac{\partial^4 w}{\partial y^4} = P\right] \quad (1)$$

where $D = Eh^3/12(1-\nu^2)$ is the flexural rigidity of the diaphragm, and w is the deflection of the diaphragm at (x,y). E is the Young modulus of silicon, h is the thickness of the diaphragm , and ν is the Poisson's ratio of the silicon. The above equation is called the plate equation. In order to find the deflection and the stress distribution in the diaphragm, the above equation must be solved with appropriate boundary conditions. Once the expression for w is obtained by solving the above equation, the value of the surface stresses in the diaphragm can be obtained using the following equations:

$$\sigma_x = -\frac{Eh}{2(1-\nu^2)}\left(\frac{\partial^2 w}{\partial x^2} + \nu\frac{\partial^2 w}{\partial y^2}\right) \quad (2)$$

$$\sigma_y = -\frac{Eh}{2(1-\nu^2)}\left(\frac{\partial^2 w}{\partial x^2} + \nu\frac{\partial^2 w}{\partial y^2}\right) \quad (3)$$

where σ_x and σ_y are the x- and y-directed surface stresses, respectively. Equations (2) and (3) provide the surface stresses on the top of the diaphragm. Considering the fact that the piezoresistors

formed by implantation/diffusion exists on the surface (top 1um) of the diaphragm, the piezoresistors may be assumed to be experiencing theses stresses [45].

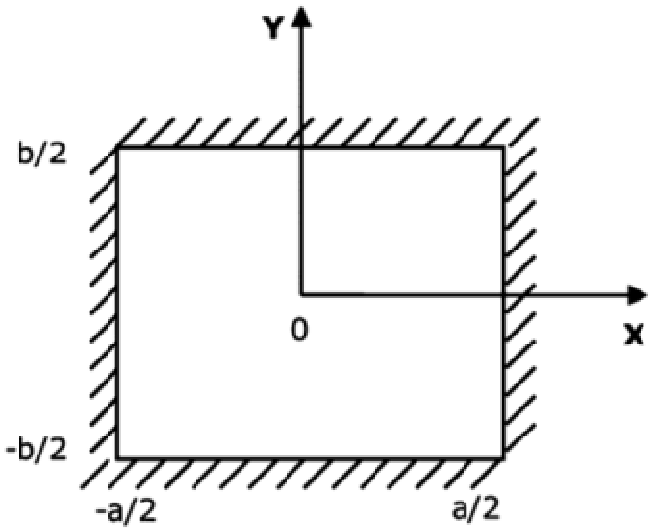

Figure 4-17 Schematic of a square plate extracted from [46]

Considering a square plate with all the edges clamped as shown in the Figure 4-17. For a square diaphragm a = b. The boundary conditions for a square plate are given by:

$$W\left(x = \pm \frac{a}{2}; y\right) = 0 \quad (4)$$

$$W\left(x; y = \pm \frac{a}{2}\right) = 0 \quad (5)$$

$$\frac{\partial W}{\partial x}\left(x = \pm \frac{a}{2}; y\right) = 0 \quad (6)$$

$$\frac{\partial W}{\partial y}\left(x; y = \pm \frac{a}{2}\right) = 0 \quad (7)$$

It is assumed that the diaphragm bending is elastic in nature, and the deflection is small compared to the thickness of the diaphragm. For the square diaphragm, no exact solutions are available, but many approximate solutions are used in literature [44]. The Load-deflection relationships for square diaphragm with Length L, thickness H are given below [47]:

$$\frac{Pa^4}{EH^4} = \frac{4.2}{1-\nu^2}\left[\frac{w}{H}\right] + \frac{1.5}{1-\nu^2}\left[\frac{w}{H}\right]^3 \quad (8)$$

'P' is measured in Pascal (Pa); 'w' is center deflection of diaphragm, 'a' is half the side length, 'E' is Young's Modulus and 'v' is Poisson's Ratio. To keep deflection in range above formula is reduced to:

$$\frac{Pa^4}{EH^4} = \frac{4.2}{1-v^2}\left[\frac{w}{H}\right] \quad (9)$$

Maximum deflection at center of diaphragm is given by:

$$w_{max} = \frac{Pa^4}{4.2EH^4} \quad (10)$$

Maximum stress at center of each edge is given by:

$$\sigma_{max} = 0.308\left[\frac{L}{H}\right]^2 \quad (11)$$

It is clear from above relations that maximum deflection is directly proportional to the square of the length of the diaphragm and inversely proportional to the thickness of the diaphragm. Once that the maximum stresses are obtained, it is possible to use them to obtain the piezoresistive change. The phenomenon by which the electrical resistance of a material changes in response to mechanical stress is known as piezoresistivity. In stressed silicon, there is a change in crystal potential distribution due to deformation. This in turn causes a change in the band diagram and the effective mass of the holes and electron. This changes the carrier mobility that leads to a change in the resistivity/resistance. Consequently, a resistor fabricated using a piezoresistive material will undergo a change in resistance when subjected to stress [45]. The mathematical analysis of the piezoresistive effect of the silicon is out of the scope of this thesis. With the current analytical formulation of the maximum stress and deflection of the pressure sensor, it is possible to validate the further mechanical FEM modeling.

Construction of the geometry of the pressure sensor

The first step in any FEM simulation consists of the fabrication of the geometric model, in this particular case just the diaphragm section will be model due to this is the part that include the piezo resistors which in turn convert the mechanical stimulus (pressure) on an electrical one (voltage). As was described in chapter 3, the pressure sensor used for this project was one purchased from BCM Sensor Technologies. As this is a commercial sensor, many of the design parameters are unknown; therefore, some of these parameters were selected based on the literature while other were obtained directly from the sensor.

One of the MEMS pressure sensor was selected and put it on the Probe Station to obtain a picture of the sensor in its superior part, which is the zone that includes the diaphragm, the connectors, and the piezo resistors. Figure 4-18 shows the image of this sensor.

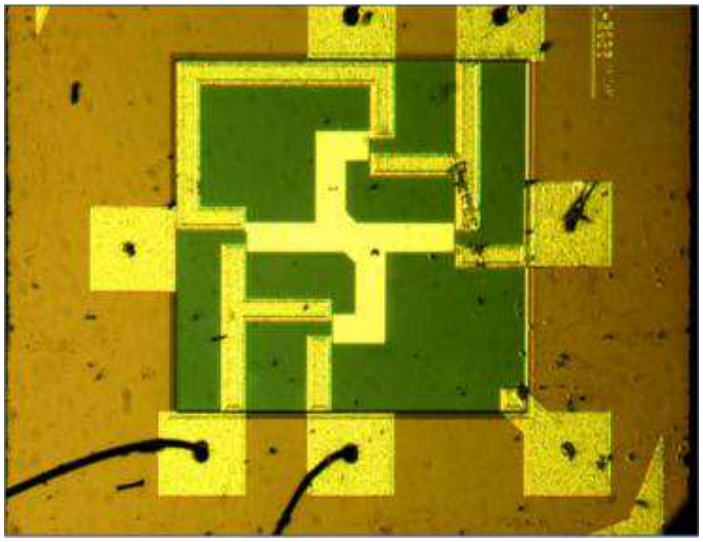

Figure 4-18. Picture of the MEMS Pressure Sensor

Using the picture taken with the probe station, and knowing the total length of the MEMS Die it is possible to interpolate the rest of the dimensions of the sensor, that is: diaphragm's length , the width of the connectors , the size, position and shape of the piezo resistors, the size of the bond pads among others. Figure 4-19a shows the picture of this sensor with the label of the dimension of the green square, which is the silicon die without the glass coating. Using this information together with an On-screen digital photo editor measurement tool is possible to obtain the dimensions needed. For this purpose, the free software Golden Ratio was used. Figure 4-19b shows the software Golden Ratio being used to get the dimension of the diaphragm.

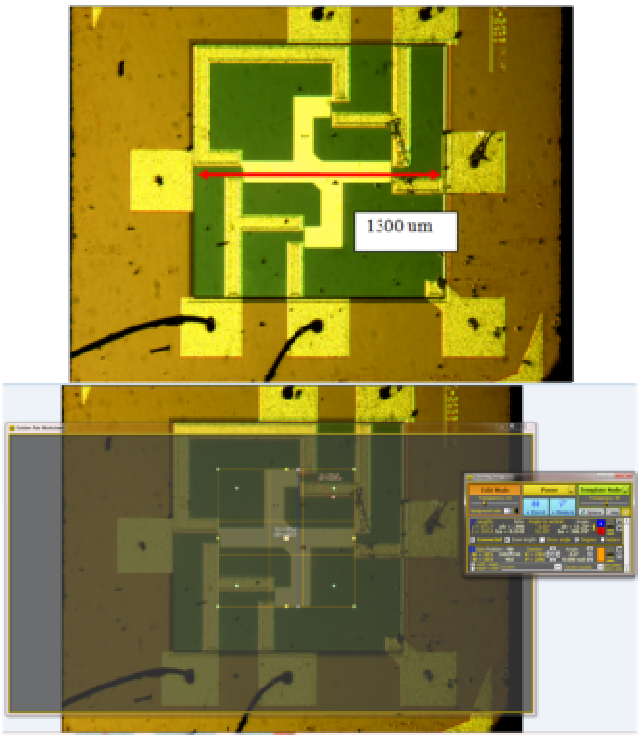

Figure 4-19 (a)Known Distance of MEMS of the MEMS Pressure Sensor, (b) Use of Golden Ratio to obtain the length of the diaphragm

With the same principle and same software, but using a bigger zoom on the probe station, was possible to obtain a picture of the piezo resistors on the diaphragm, and get in this way their shape, their dimensions and their position. Figure 4-20 shows the picture of one of the piezo resistors on the diaphragm. It can be seen in Figure 4-20, the piezo resistors have a serpentine shape. To bring the complete piezo resistors within the high-stress regions, meander shaped piezo resistors, as shown in Fig. 4-20 are used. These types of piezo resistors generally consist of a piezoresistive and a connecting arm. The number of turns in the piezo resistor is dependent upon the particular sensor; the serpentine shape is preferred for better sensitivity than any other configuration [45], [48]. The total length of the piezo resistor arm is divided between the different arms to get the same resistance as a resistor without a turn.

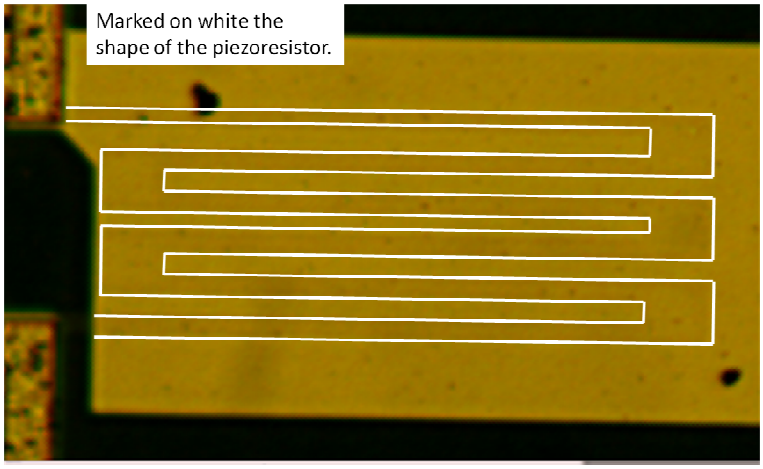

Figure 4-20. Picture of the Piezoresistor element of the MEMS Pressure Sensor

Regarding the resistor's size, from the technology point of view, larger resistors can be matched with the high-stress regions easily but at the same time larger resistors lead to a reduced sensitivity due to the stress averaging effect [45].Concerning to the placement of the piezo resistors, when the diaphragm is considered as a thin plate, clamped at the four edges, the maximum stresses exist at the center of edges. Therefore, generally the four piezo resistors are placed at the center of the four edges of the diaphragm. According to this general design principle, we can obtain the length of the diaphragm based on the position of the piezo resistors. Figure 4-21 shows the diaphragm of the pressure sensor marked on red.

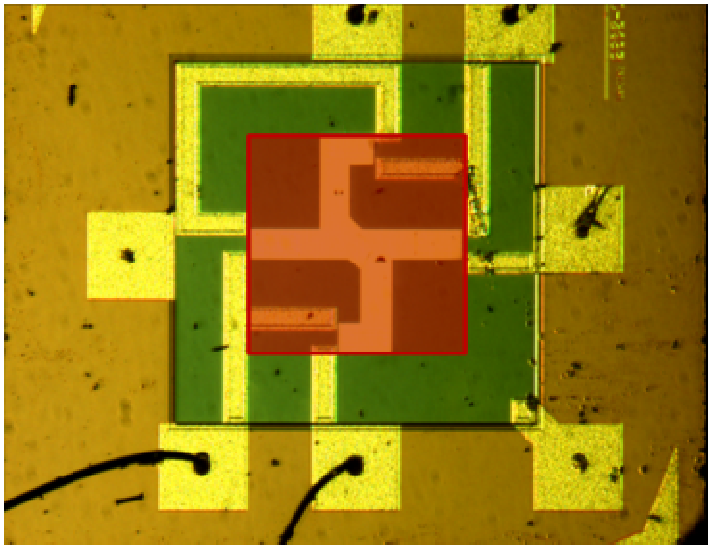

Figure 4-21 Marked on red, diaphragm of the MEMS pressure sensor

Once that the information of the length of the diaphragm of the sensor was obtained, the thickness of the diaphragm can be inferred using the output curve defined by the supplier and the design principle of small deflection for thin plates. It is generally desirable to have a deflection scheme that is linear with pressure as such sensors are easy to calibrate. For a small deflection of the diaphragm, the diaphragm deflection is directly proportional to the applied pressure. Usually, the diaphragm in a micro pressure sensor is modeled as a plate clamped at the edges. A plate can be considered to be "thin" if the ratio of the thickness of the diaphragm to the smaller span length is <1/20 [49]. The small deflection theory for bending of thin plates assumes that the deflection of mid-point of surface of diaphragm must be small compared to thickness of the plate and the maximum deflection must be <1/5th of thickness of the diaphragm. The Table 4-2 show s the dimensions of the sensor.

Table 4-2 Parameters of the MEMS Pressure Sensor

PARAMETER	DIMENSION
Length of diaphragm	750 um
Thickness of diaphragm	34 um
Width of piezo resistor	6 um
Length of piezo resistor	172 um
Length of shoulder of piezo resistor	20 um
Length of Bond Pad	300 um
Total of traces per serpentine of each piezoresistor	6

Once that the dimensions have been obtained, it is possible to build the physical model on COMSOL Multiphysics© using the MEMS Module. The geometry was created using a block (the diaphragm) with the given values of width, depth, and height. Two work planes are defined on the top and bottom side of the block. The next step is to define the borders of the membrane on the work planes. This also sets the frame at the same time. Afterward, the remaining geometry of the sensor, hence the dimensions of the resistors and the connections, is defined by a 2D drawing on the upper work plane. Figure 4-22 shows the model of the pressure sensor. Figure 4-23 displays the area of the diaphragm and the piezo resistors on the diaphragm.

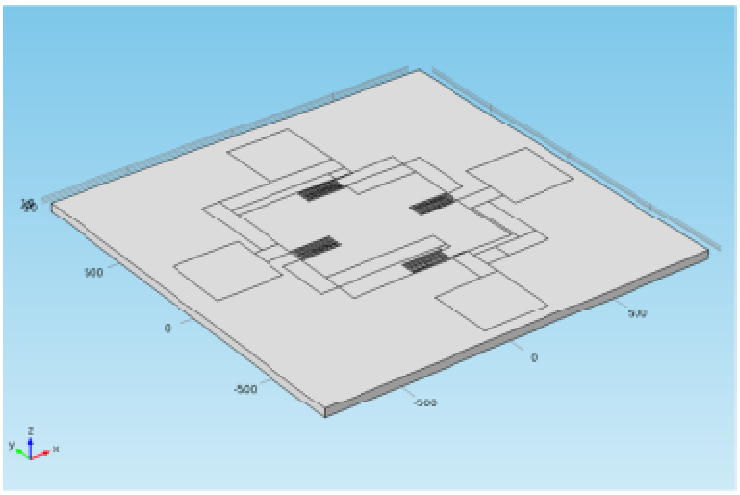

Figure 4-22 Model of the MEMS pressure sensor built on COMSOL Multiphysics©

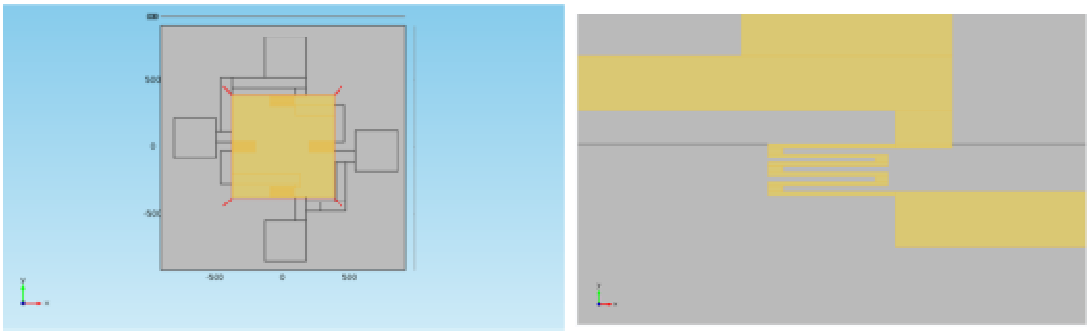

Figure 4-23 (a)Diaphragm on COMSOL, (b) Piezoresistors on the diaphragm

Definition of the governing equations

In the following sections, we will gather and then put together the pieces required to complete the analytical description for the output of a pressure sensor. The governing equation of this model is the same described before on the mathematical analysis. The governing differential equation for a two-dimensional plate with a uniform pressure load, P, subject to lateral bending can be expressed as [34] :

$$D\left[\frac{\partial^4 w}{\partial x^4} + 2\frac{\partial^4 w}{\partial x^2 \partial y^2} + \frac{\partial^4 w}{\partial y^4} = P\right] \quad (1)$$

In order to find the deflection and the stress distribution in the diaphragm, the above equation must be solved with appropriate boundary conditions. Once the expression for w is obtained by solving the above equation, the value of the surface stresses in the diaphragm can be obtained using the following equations:

$$\sigma_x = -\frac{Eh}{2(1-\nu^2)}\left(\frac{\partial^2 w}{\partial x^2} + \nu\frac{\partial^2 w}{\partial y^2}\right) \quad (2)$$

$$\sigma_y = -\frac{Eh}{2(1-\nu^2)}\left(\frac{\partial^2 w}{\partial x^2} + \nu\frac{\partial^2 w}{\partial y^2}\right) \text{ (3)}$$

where σ_x and σ_y are the x- and y-directed surface stresses, respectively. These equations provide the surface stresses on the top of the diaphragm. Considering the fact that the piezoresistors formed by implantation/diffusion exists on the surface (top 1um) of the diaphragm, the piezoresistors may be assumed to be experiencing theses stresses [45].

Considering a square plate with all the edges clamped as shown in the Figure 4-21. For a square diaphragm a = b. The boundary conditions for a square plate are given by:

$$W\left(x = \pm\frac{a}{2}; y\right) = 0 \text{ (4)}$$

$$W\left(x; y = \pm\frac{a}{2}\right) = 0 \text{ (5)}$$

$$\frac{\partial W}{\partial x}\left(x = \pm\frac{a}{2}; y\right) = 0 \text{ (6)}$$

$$\frac{\partial W}{\partial y}\left(x; y = \pm\frac{a}{2}\right) = 0 \text{ (7)}$$

The piezo resistors must be placed in these regions to experience the maximum stress and thus provide maximum sensitivity. The piezo resistors on top of a diaphragm in pressure sensor experience no uniform stress, and, therefore, the non-uniform stresses must be accounted for by averaging the stress on the resistors as shown in Equations 8 and 9:

$$\sigma_{yave} = \frac{1}{A}\int_y \int_x \sigma_y dxdy \quad (8)$$

$$\sigma_{xave} = \frac{1}{A}\int_y \int_x \sigma_x dxdy \quad (9)$$

where σ_x and σ_y are the x- and y-directed stresses on the diaphragm, σ_{xave} and σ_{yave} are the average x- and y-directed stresses at the piezoresistor location, respectively. A is the area of each piezoresistor. To get the correct value of relative change in resistance we must use the value of σ_{xave} and σ_{yave}. The relative change in resistance can then be expressed by:

$$\frac{\Delta R}{R} = \pi_l \sigma_{xave} + \pi_t \sigma_{yave}$$

After understanding the relationship between change in resistance and applied stress, we can now obtain the equations for the output of a piezoresistive pressure sensor with four piezo resistors in Wheatstone bridge configuration. The general equations for a Wheatstone bridge circuit can then be used to obtain the output of a micro pressure sensor.

The output of the pressure sensor is calculated by approximating the stresses on the piezo resistors. The maximum stress regions of the diaphragm and the placement of the resistors on the diaphragm are shown in figure 4-24.

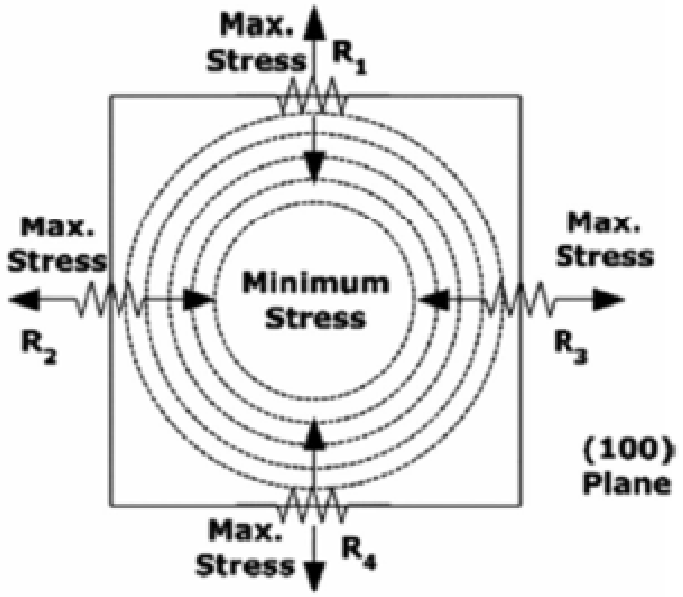

Figure 4-24. Placement of piezoresistors and stress distribution on the diaphragm surface extracted from [46]

Each resistor experiences both longitudinal and transverse stress. Let σ_l and σ_t denote the longitudinal and transverse stress experienced by R2 and R3. Then, the stress experienced by R1 and R4 can be approximated as longitudinal stress, σ_l and transverse stress, σ_t (which is rotated by an angle of 90°, compared to stresses in R2 and R3). Initially, R1 = R2 = R3 = R4 = R0. When R2 experiences stress due to σ_l and σ_t, the relative resistance change is given by:

$$\alpha_1 = \frac{\Delta R_2}{R_2} = \pi_l \sigma_l + \pi_t \sigma_t$$

where π_l and π_t are the longitudinal and transverse piezoresistive coefficients of silicon, respectively. Similarly, the relative resistance change for R1 is given by:

$$\alpha_2 = \frac{\Delta R_1}{R_1} = \pi_l \sigma_l + \pi_t \sigma_t$$

where α_1, $\alpha_2 > 0$ (as $\Delta R_2 > 0$ and $\Delta R_1 < 0$). Also, by symmetry, $\frac{\Delta R_3}{R_3} = \alpha_1$ and $\frac{\Delta R_4}{R_4} = -\alpha_2$. The output voltage of the sensor can then be given by:

$$V_{out} = \left(\frac{R_1 R_3 - R_1 R_4}{(R_1 + R_3)(R_2 + R_4)}\right) V$$

$$V_{out} \approx \left(\frac{\alpha_1 + \alpha_2}{2(1 + \alpha_1 - \alpha_2)}\right) V$$

By knowing the piezoresistive coefficient and stresses on the resistors, we can estimate the output of the sensor.

Definition of the materials and properties

The material of the whole diaphragm (membrane and frame) is single crystal, lightly doped n-silicon. The material of the piezoresistors is lightly doped p-silicon. Aluminum is used as a metal strip to connect between resistors. Table 4-3 shows the different materials and properties for the MEMS pressure sensor.

Table 4-3Materials and properties used on the model

Materials and properties			
Component of model	Material	Property	Value
Diaphragm	Silicon	Young modulus	166 Gpa
		Poisson's ratio	0.26
		Density	2330 kg/m^3
		Electrical Conductivity	NA
		Piezoresistivity Matrix	NA
		Heat Capacity	712 Joules
		Coefficient of linear expansion.	$2.6 * 10^{-6}°C^{-1}$

Piezoresistors	P-doped Polysilicon	Young modulus Poisson's ratio Density Electrical Conductivity Piezoresistivity Matrix Heat Capacity Coefficient of linear expansion.	Elasticity Matrix 0.26 2330 kg/m^3 COMSOL function COMSOL function 712 Joules NA
Connections	Aluminum	Young modulus Poisson's ratio Density Electrical Conductivity Piezoresistivity Matrix Heat Capacity Coefficient of linear expansion.	70 GPa 0.35 2330 kg/m^3 35.6 10^6 S/m NA 904 Joules NA

Definition of boundary conditions

The lower side of the frame is defined a fixed and a pressure applied on the upper side of the membrane as boundary load. The areas within the boundaries of the connections are determined as thin conductive layers with a thickness of 400 nm and the areas bordered by the geometry of the resistors are defined as thin piezoresistive layers, also with a thickness of 400 nm. The electrical properties are determined by setting a ground and a terminal at the edges of two connection pads for each sensor and a voltage, usually 5V, is applied to them. For easier analysis of the terminal current an average has to be defined by these edges as well as over the relevant edges or boundaries at the remaining connection pads where the voltage for the device output is supposed to be measured. The mesh for the FEM analysis is built by the software on the base of the defined physics. The element size is defined as "finer". Because of the simple geometry and the consideration of only a few physical effects, the computer-generated mesh is sufficient and does

not have to be optimized by user controlled settings in order to decrease the time that is needed for the numerical analysis.

Results of core model

Once that the geometry, materials, and boundary conditions have been defined, the discretization of the model was performed. The physics-controlled mesh sequence of COMSOL was used. This tool select the meshing according to the physics involved in the problem. Figure 4-25 shows the meshing of the model. It can be seen in the Fig 4-25, that the denser mesh is located on the piezoresistors area, which are the ones that will be subjected to the highest stresses.

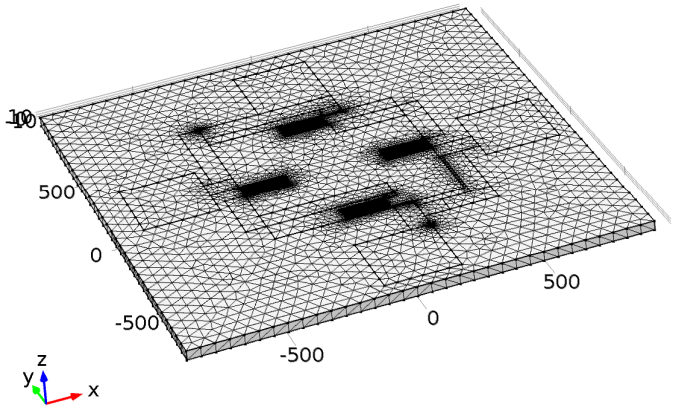

Figure 4-25.- Discretization scheme of the piezoresistive pressure sensor model.

To validate the meshing, different sizes of elements were used to obtain the maximum deflection at a pressure stimulus of 100 bar, and using the maximum deflection value obtained theoretically a comparison was made to validate the discretization. Table 4-4 shows the result of this validation.

Table 4-4.- Comparison of meshing size versus maximum deflection value.

Element size	# Elements	Maximum deflection value	Difference respect to theoretical value
Extremely Coarse	1603	4.8 µm	25 %
Coarser	3260	5.2 µm	19%
Coarse	13553	6.09 µm	5%
Normal	20523	6.31 µm	2.3%

Fine	34833	6.385 µm	0.4 %
Finer	48521	6.39 µm	0.0%

Theoretically the shear stress should be maximal at the midpoint of the edge of the diaphragm. Figure 4-26 shows the shear stress along the edge in the model. This shows a maximum magnitude at the center of each of the two edges along which the plot is made. Stress has its maximum value close to the piezoresistor with a value of approximately 897 Mpa.

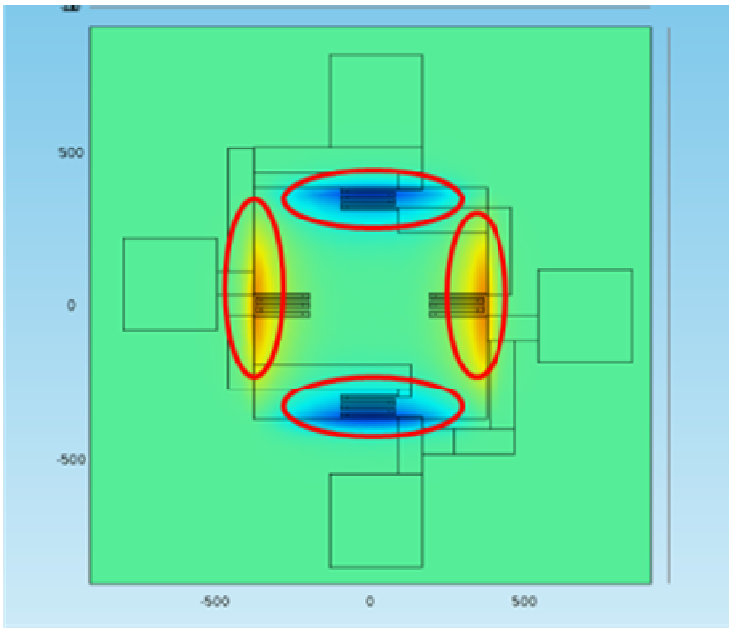

Figure 4-26 Modeling stress results, position of the piezoresistors on the highest stress zone

Displacement of the diaphragm as a result of 10 Mpa (100 bar) difference applied to the membrane at its center is 6.39 um. The result is in good agreement with the theoretical and mathematical result. The RED color shows the maximum displacement at the center of the diaphragm, similarly the displacement along the edges are zero as they are fixed, this is shown by BLUE color.

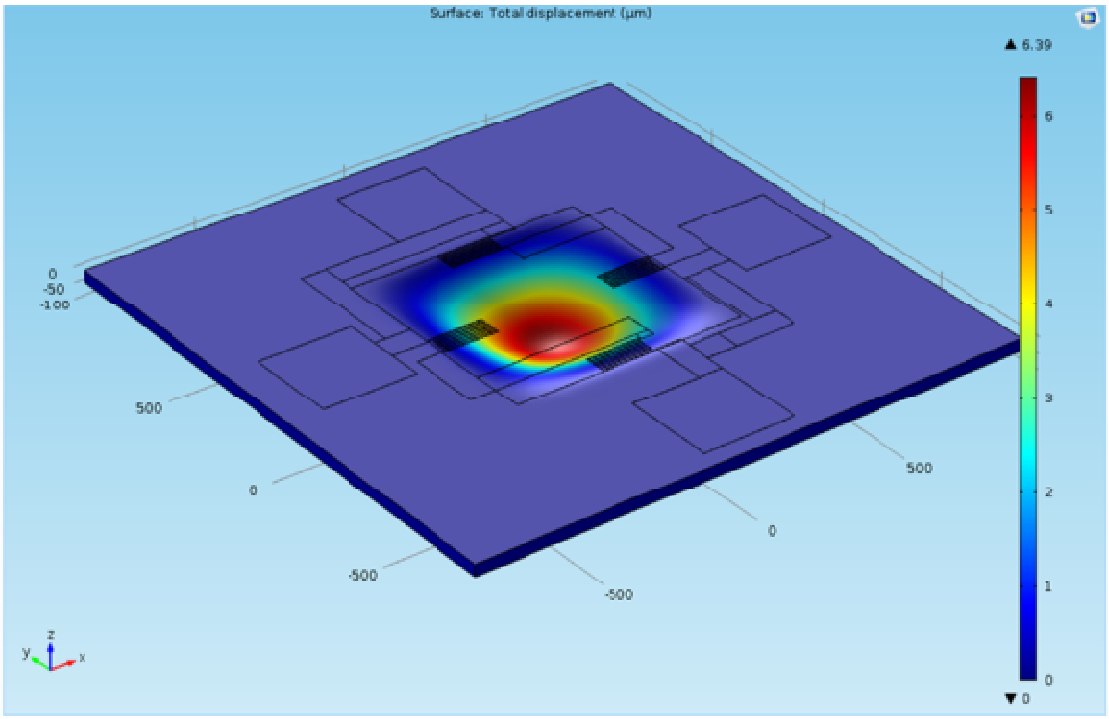

Figure 4-27 Diaphragm deflection as result of an applied pressure of 10 Mpa

Once that the model has been validated in terms of displacement and stress, a complete cycle of loading was performed, from 0 to 10 Mpa in steps of 0.5 Mpa, this with the purpose to compare the simulated output with the expected output of the commercial sensor. Figure 4-28 shows the voltage output resulting from the model at an applied pressure of 10 Mpa. Figure 4-29 displays the comparison between the model on COMSOL and the commercial sensor.

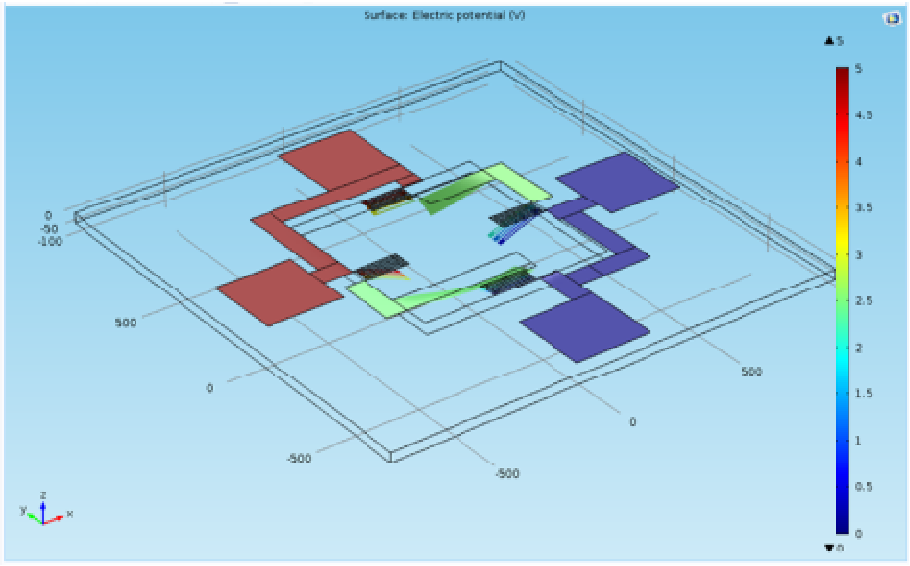

Figure 4-28 Voltage output as result of an applied pressure of 100 bar

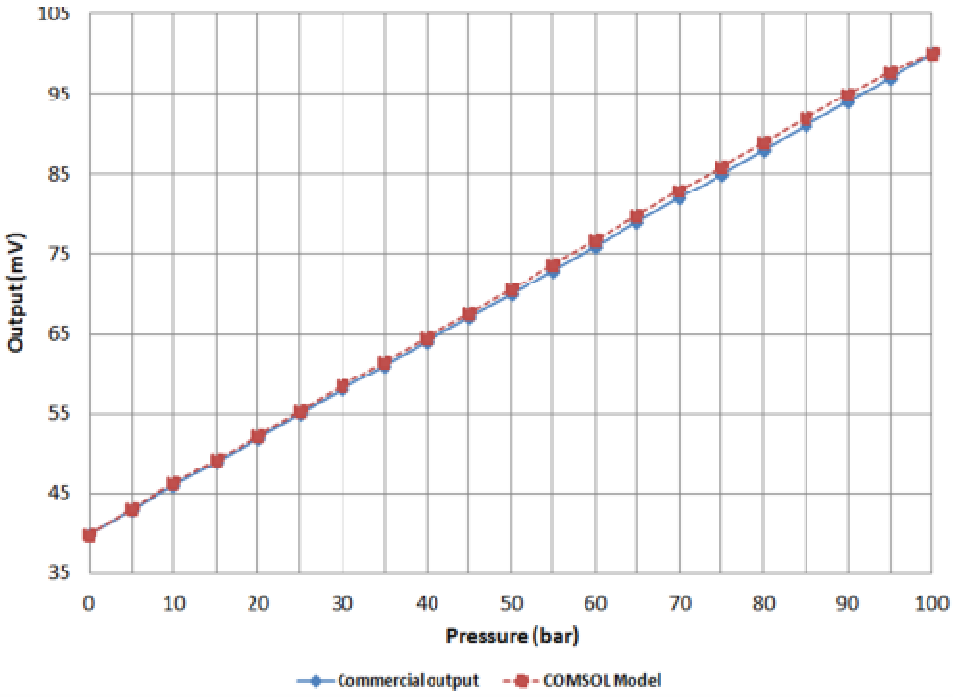

Figure 4-29 Comparison of COMSOL Model voltage output and Commercial sensor voltage output. The data was normalized to a common initial offset of 40 mV.

Table 4-5 Comparison of COMSOL model and commercial sensor spec sheet

Pressure, bar	Commercial sensor output, mVolts	COMSOL model output, mVolts
0	40	40
5	43	43.2
10	46	46.3
15	49	49.3
20	52	52.4
25	55	55.4
30	58	58.5
35	61	61.6
40	64	64.6
45	67	67.6
50	70	70.6
55	73	73.7
60	76	76.8
65	79	79.8
70	82	82.9
75	85	85.9
80	88	89
85	91	91.9
90	94	95
95	97	97.9
100	100	100.1

Analyzing the data, the COMSOL model follows the expected sensor output really close, with a difference of 1 mV at the worst case and an average percentage difference of 2.4 %. This model is the core stone for the final mechanical model that includes the parylene layer. As was previously commented, there is a compliant protection layer on top of the sensor. The following model has the purpose to understand if this layer has a strong influence on the performance of the sensor or not. The FEM with COMSOL 5.0 software was used to simulate the mechanical behavior of the device. A layer of parylene with the corresponding material properties listed on table 4.4 was put over the upper face of the diaphragm. Forces were applied as pressure loads at the top of the parylene layer. The pressure is transferred through the parylene to the top of the

diaphragm and consequently to the piezoresistors. To obtain a more realistic result, temperature-dependent material properties were used (see Appendix 1), and the effect of the thermal expansion was added to this model using the coupling module of COMSOL. Figure 4-30 shows the general 3D model of the pressure sensor with the parylene layer on it.

Table 4-6 Properties of protection layer

Materials and properties			
Component of model	Material	Property	Value
Protection layer	Parylene	Young modulus	2.76 Gpa (see Appendix A)
		Poisson's ratio	0.4
		Density	1290 kg/m^3
		Thickness	4 um
		Piezoresistivity Matrix	NA
		Heat Capacity	712 $J/(kg * ℃)$
		Coefficient of thermal expansion	$30 * 10^{-6} ℃^{-1}$

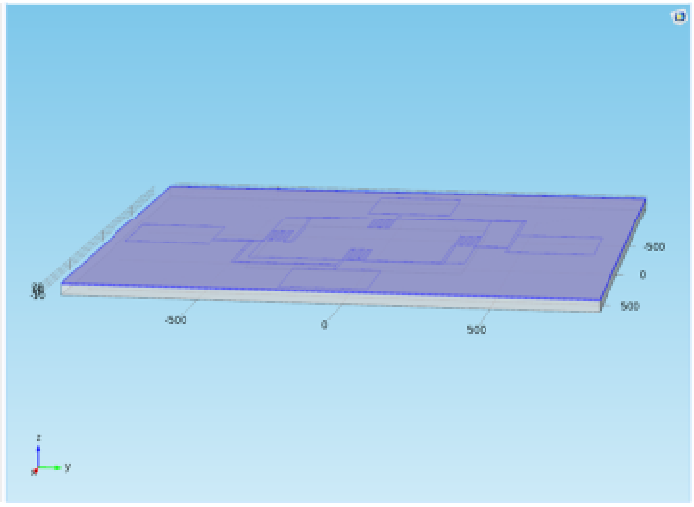

Figure 4-30. Parylene layer over the diaphragm of the piezoresistive pressure sensor.

For comparison, the core model without parylene explained before, and the model with the parylene layer were analyzed. Figure 4-31 shows the result of the comparison. It can be seen in Fig 4-31 that the output of the sensor is reduced near to a 21 % due to the effect of the parylene layer, the sensitivity of the sensor change from 0.6 mV per bar to 0.475 mV per bar.

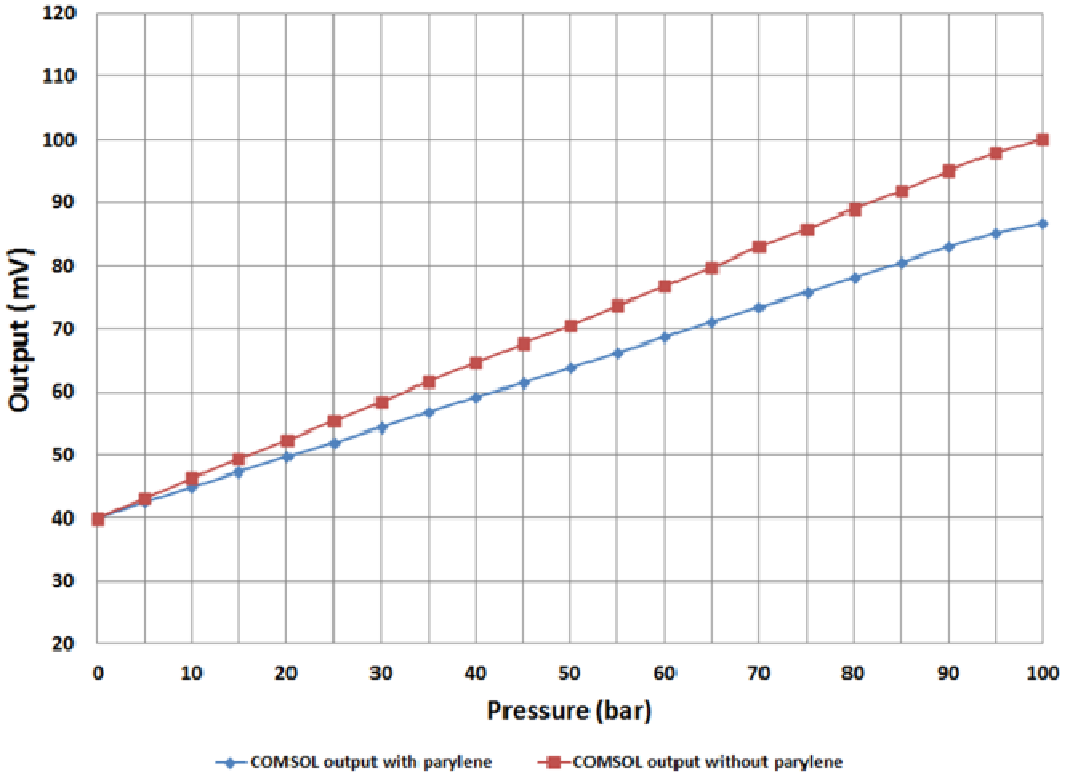

Figure 4-31. Output of pressure sensor with and without Parylene layer.

To understand the effect of the temperature on the performance of the MEMS Pressure sensor, the temperature coefficient of Span (TCS) was obtained from the manufacturer of the MEMS Pressure Sensor, the TCS is equal to 0.22 $\%FSO/℃$. (Full scale output). Using this information, the temperature coefficient of Span was added to the COMSOL Model. Figure 4-32 shows the expected output of the model at different temperatures .

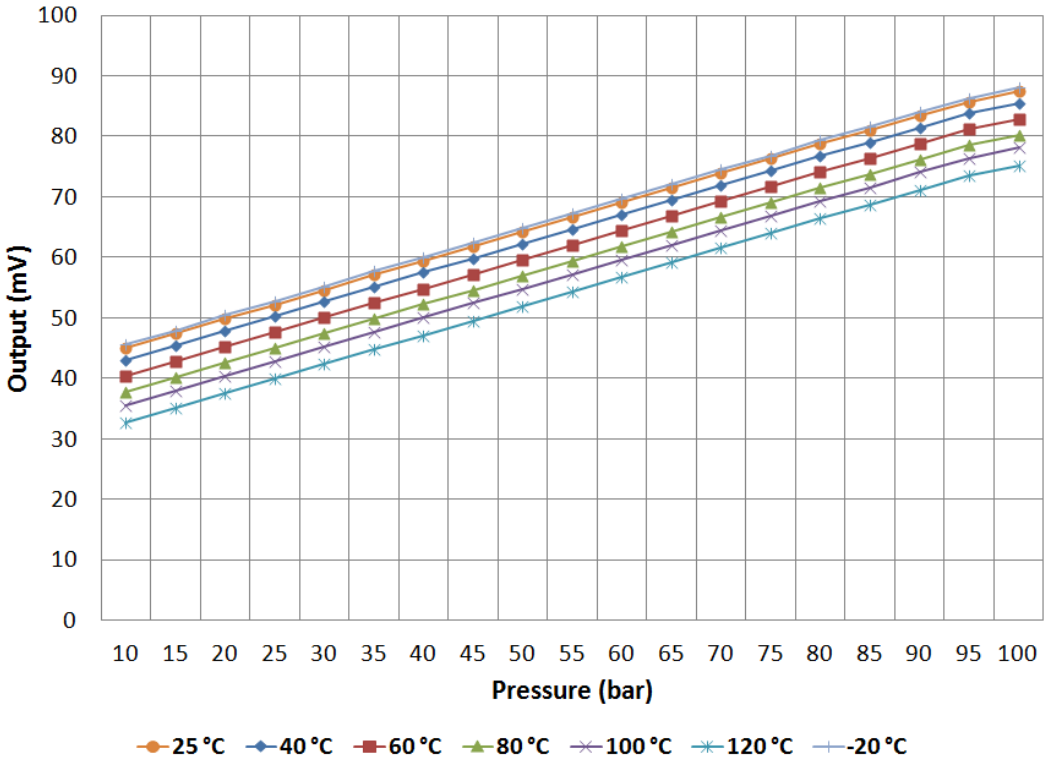

Figure 4-32.- Output of the COMSOL model at different temperatures

Chapter 5

Experiments and Results

In this chapter, the experimental procedures and their results for the fabricated prototypes are presented. The results of the experiment are compared with the results of the model. Finally, characteristics of the sensor, such as sensitivity, accuracy and linearity are analyzed.

5.1 Experimental Setup

The fabricated devices were tested at the installations of MorHEAT ©, which is a company dedicated to the fabrication of premium plastic melt temperature and pressure transducers. The test bench used for the characterization of the fabricated samples is shown on Figure 5-1.

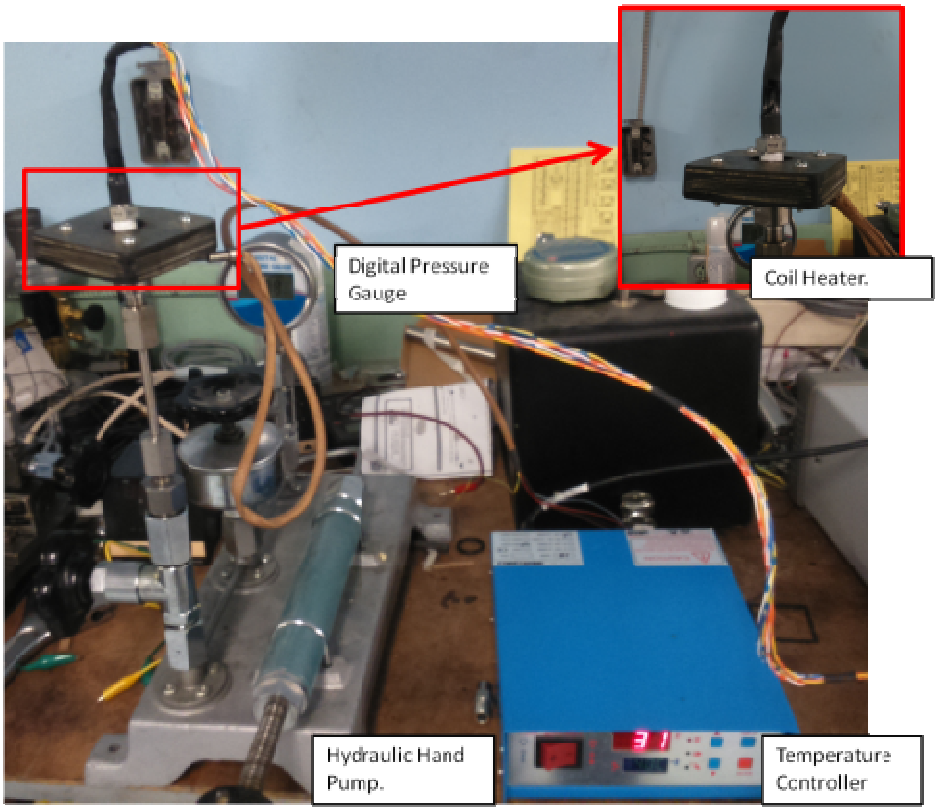

Figure 5-1.- Test set up for Pressure and Temperature measurements

The samples were connected to a 1/4 18 NPT female fitting attached to a custom made hydraulic hand pump which pressure is monitored by a digital hydraulic pressure gauge model HX601 manufactured by HUAXIN INSTRUMENT (BEIJING) CO., LTD. with a resolution of 1 psi and ± 0.05% accuracy of Full Scale Output ,and calibrated by the staff of MorHEAT ©.

The fitting were covered by a coil heater that includes a type -T Thermocouple positioned close to the sample to monitor the temperature. A HotRunner 10A controller monitor and control the temperature. To limit thermal error being introduced as the fitting was heated, the reference pressure gauge was positioned away from the sample on the high-pressure line. The complete apparatus allowed characterization of the test sensor from room pressure (13 psi) to 500 psi over a temperature range of 25 to 120°C. An NI USB-6009 analogue-to-digital converter (ADC) captured and stored outputs from the MEMS Pressure sensor and the RTD using the Labview software suite from National Instruments. This setup tests the sensor with the electronics being external to the apparatus, considering only the effect of temperature on the sensor, which is the case in the real conditions of operation.

The samples were individually connected to the apparatus, pressurized by hydraulic oil and connected to the ADC. A DC input voltage of 5 V was applied to the sensor Wheatstone bridge and a DC input current of 1 mAmp was applied to the RTD transducer using an Agilent E3631A Triple Output DC Power Supply.

5.2 Sensor Characterization

For the realization of this experiment, the temperature was fixed at four different levels: room temperature (25 °C), 40, 60 and 100 ° C. In each of these increments and once the temperature was stable, a stimulus of pressure was applied starting at 25 psi, 50 psi, and thenceforth, 50 psi increments up to 450 psi. These sets of the temperature-pressure stimulus were repeated three times in each sample. The average temperature ramp rate is ~6.1°C/min, while the average temperature reduction rate is ~0.9°C/min. Figure 5-2 shows the output of the pressure sensor of sample # 1 at different temperatures from 25 to 450 psi. During the test of first set of samples, the signal of the MEMS Pressure sensor was lost at 450 psi in the third iteration at room temperature. The analysis of this problem will be addressed later in this chapter. The MEMS pressure sensor reported a change of 0.20 % of the Full-scale output per Celsius according to the experiment, which in terms of millivolts is a decrease in the output of 1.98 mV, 4.62 mV, and 9.9 mV, at 40 °C, 60 °C, and 100 °C, respectively.

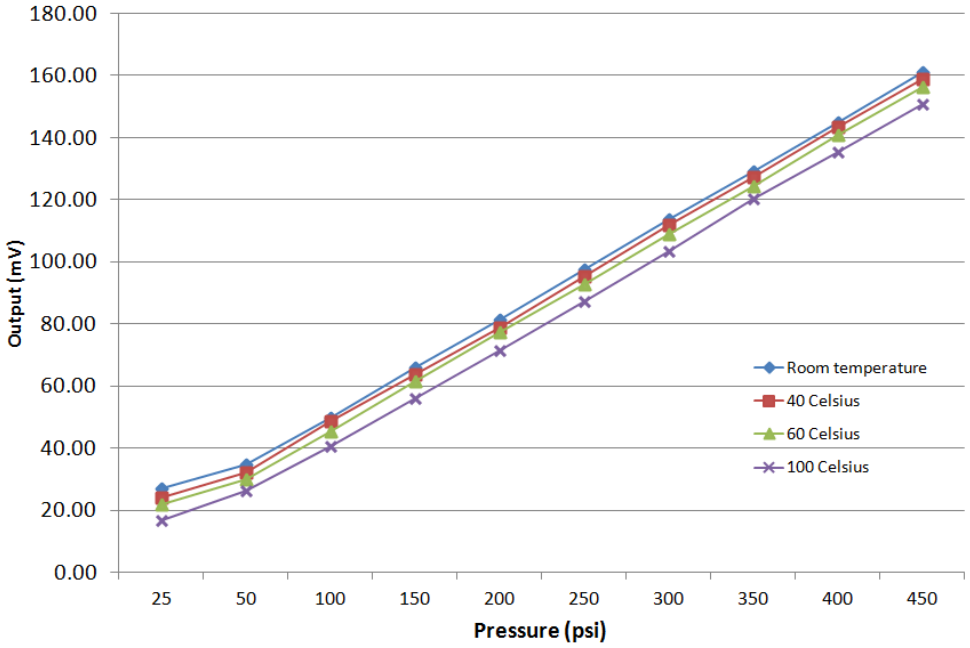

Figure 5-2 Output of the pressure sensor of sample #1 at different temperatures

5.3 Analysis of failure

During the test of the first set of samples, the signal of the first set of samples was lost at 450 psi during the third iteration at room temperature. Three hypothesis of this failure were proposed: 1) a loss of connection between the TO Header pins and the cables, 2) a damage of the bond pad of the MEMS sensor, and 3) a damage of the wire bond. To walk through the analysis of the failure, the connections of the TO Header pins to the electrical wires were checked with a multimeter, no issues were found here. After that, the sample was put under the microscope to analyze the bond pads and the wire bonds. Figure 5-3 shows a picture of the bond pads of the sample under a microscope. No physical damage was found on the bond pads.

Figure 5-3 Microscopic picture of the bond pads of sample # 2 (left), Close up to the bond pad #3 of sample #2 (right).

Once the bond pads were checked, the trajectory of the wires between the TO Header pins and the bond pads were observed with the microscope to look for some possible defect. Broken wire bonds were found in the MEMS sensor. Figure 5-4 shows the detail of the broken wire of bond pad #3 of sample 1.

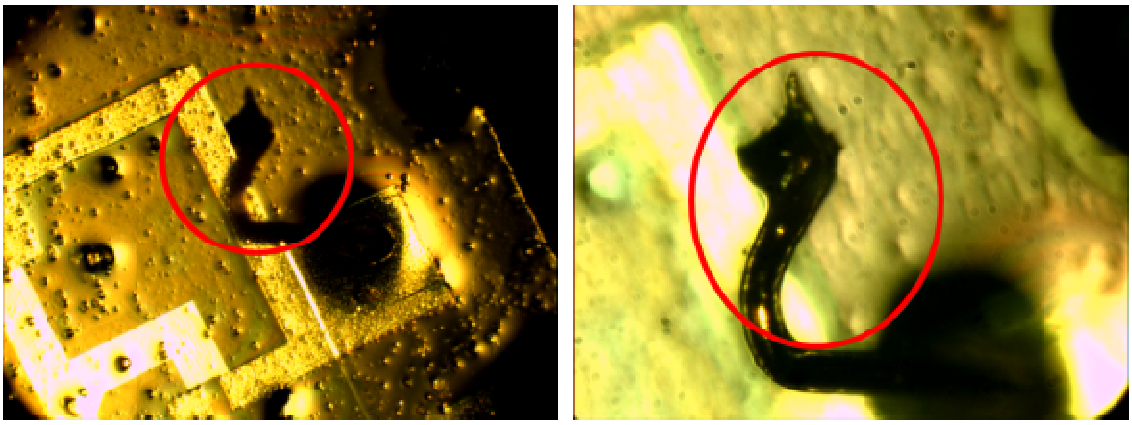

Figure 5-4 Analyze of wire bonds of firs set of samples; Wire connecting the bond pad #3 to the TO Header pin (left), Close up at the area of the broken wire (right).

There are two possible reasons for failure by breaking the cable. One of them may be electrical, due to a short circuit or an over-current that had burned the wire. The other possible reason is by any mechanical event that caused a break in the wire. Considering that the power supply used during the experiment, an Agilent E3631A Triple Output DC Power Supply, which output is protected against overcurrents, has been used to test these same sensors for a while without presenting any problem, this possible cause is discarded. A potential degradation of the parylene

layer is discarded because the parylene is mechanical and thermally stable up to 220 °C, and the presence of a small defect in the Parylene film or Parylene-wire adhesion would cause a severe degradation of the device when exposing it to the oil, and, therefore, the electrical measurement would give an open-circuit signal since the beginning of the test. Taking to account that during the tests of the soldering process some leaks were found in the glass section of the TO Header by applying high pressure, and that during the test of sample #1 a leak was detected on the TO Header at 450 psi, a possible leak could cause a lateral flow of the fluid over the wire, causing a rupture. To protect the wire bonds, a dam and fill epoxy encapsulation was used on the next samples. For this purpose, the Epoxy EPO-TEK 301 manufactured by Epoxy Technology Inc was used to cover the wire bonds. This epoxy is recurrently used to protect semiconductors and optoelectronics, have a normal-good adhesion to Parylene, and doesn't present thermal degradation until 300 °C. It is important to comment that the encapsulation was done in a way that the Epoxy was not applied to the diaphragm of the sensor, because this would blocked the access to the pressure stimulus of the pressure sensor. Furthermore, the Epoxy was not applied to the RTD sensor because this would add thermal mass to the RTD sensor. Figure 5-5 shows the result of the application of the Epoxy over the sensor system.

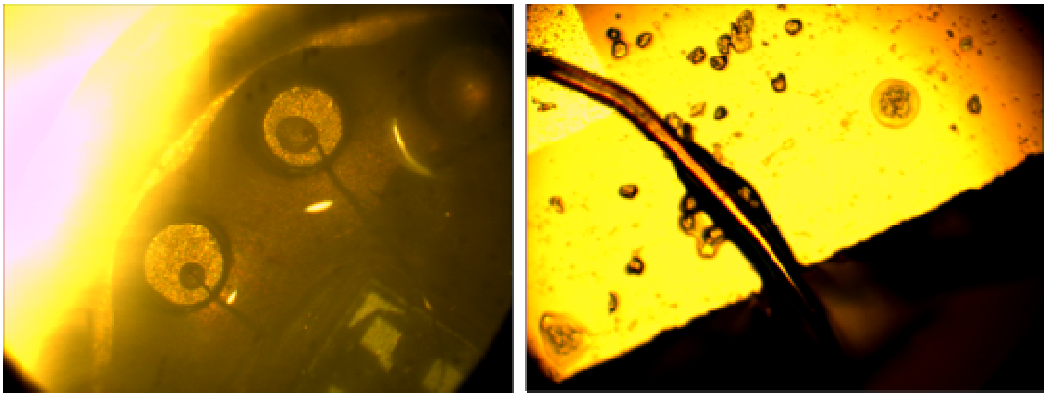

Figure 5-5 Sample # 3 encapsulated by Epoxy. A) Detail of the TO Header pins covered by EPO-TEK 301, b) Detail of the wire bond covered by EPO-TEK 301.

Once the sample was covered with the epoxy and welded at the installations of Whitfield Welding, the sample was tested. This time, the test was performed up to 120 °C in steps of 50 psi up to 450 psi. The set of the temperature-pressure stimulus was repeated three times. The output of the pressure sensor of sample # 3 at different temperatures from 25 to 450 psi are reported on figure 5-6. The MEMS pressure sensor reported a change of 0.24 % of the Full-scale output per Celsius according to the experiment, which in terms of millivolts is a decrease in the output of 7.26 mV, and 13.2 mV, at 60 °C, and 120 °C, respectively.

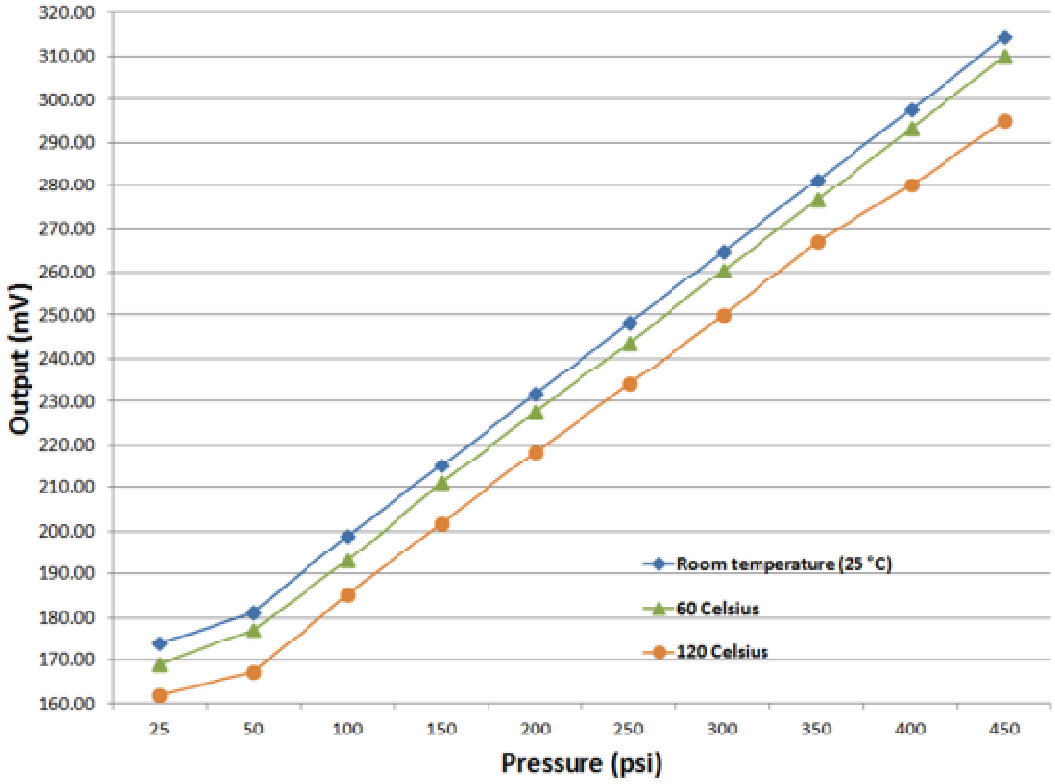

Figure 5-6.- Output of the sample #3 at different temperatures.

Figure 5-7 shows the output of the pressure sensor of the sample at room temperature compared with the output of the sensor without parylene layer reported by the supplier. The plot shows the data without offset and gain. The sample shows a sensitivity of 0.490 mV/bar compares with the commercial output of 0.602 mV/bar**.** The reduction of the sensitivity due to the parylene layer is approximately 18.5 %.

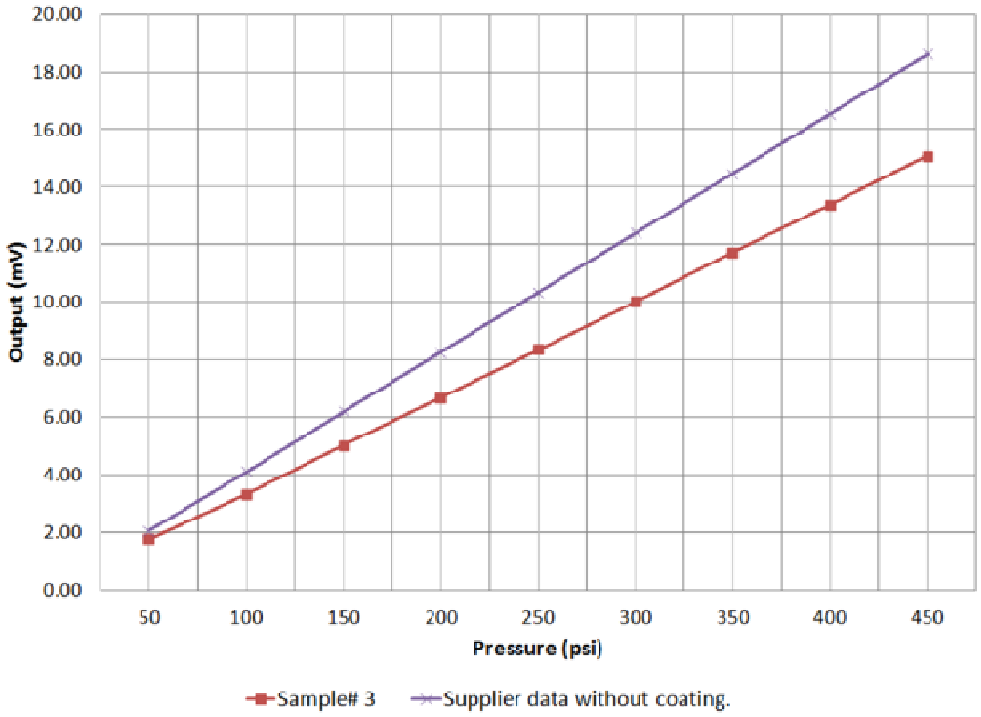

Figure 5-7.- Comparison between sample data versus output reported by the supplier. The sample presents a reduction in the output close to 18.5%.

5.4 Multifunctional characteristic curve.

Figure 5-8 combines the experimental data of the temperature RTD sensor output with the MEMS pressure sensor output and provides a comprehensive characteristic plot for the interpretation of the outputs of the sensor. In the plot, the effect of the temperature at the output of the MEMS pressure sensor can be observed. In the same way, the impact of the pressure on the output of the RTD temperature sensor is observed. The graph shows the results in a pressure range from 25 to 450 psi at intervals of 50 psi and a temperature range of 25 to 120 °C in steps of 20 °C.

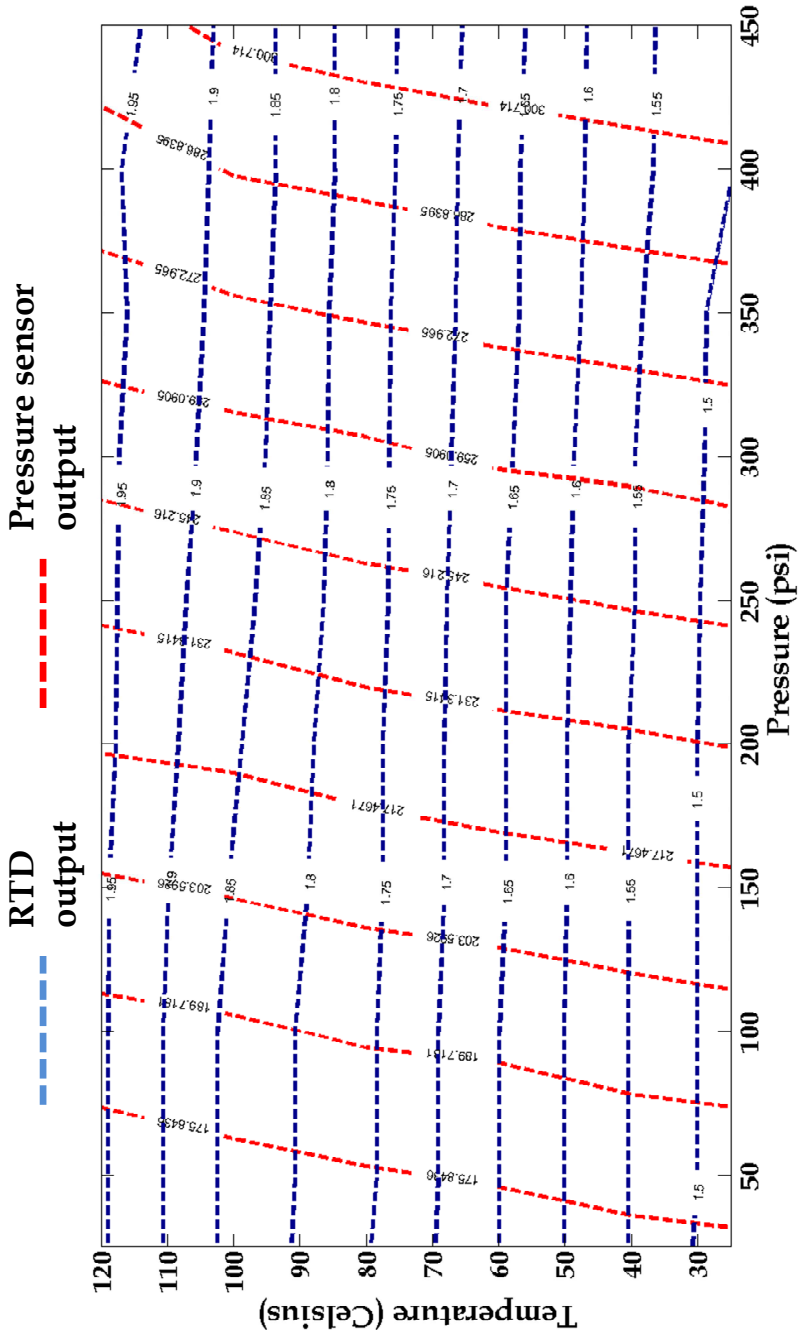

Figure 5-8.- Multifunctional sensor characteristic curve of the sample.

5.5 Accuracy

Accuracy, or more descriptively inaccuracy, is defined as the difference between the actual value and the measured value of a given quantity. Figure 5-9 shows the comparison between the RTD temperature reading (once that the transfer function was used to convert the electrical

output on temperature readings) and the temperature reported by the controller. The plot was obtained from the data recorded with LABVIEW, with a sampling of 1 second. The thermal response of the RTD sensor agrees with the temperature reported by the controller. However, on the parts marked with a green circle there is an increase of temperature with respect to the temperature reported by the controller. This increase of temperature corresponds to the moment when the pressure of 400-450 psi is applied. This increment is due to the application of the high pressure over a container with the fluid of constant volume (such as the apparatus used), temperature and pressure are directly proportional to each other. This means that as the temperature decreases, the pressure also decreases, and as the temperature increases, the pressure increases [50].

For the purpose of estimating the sensor accuracy, the average of the RTD signal during one second on the zones of constant temperature is taken as the actual value of the signal.

Using the data received from the temperature controller and the one obtained from the RTD readings is possible to calculate the accuracy of the RTD sensor using the formula below [51].

$$\%\boldsymbol{Accuracy} = \left|\frac{\boldsymbol{RTD\ reading - Controller\ reading}}{\boldsymbol{Controller\ reading}}\right| \times \mathbf{100}$$

The accuracy with respect to the temperature controller is 0.83 %. It is important to mention that the controller have a accuracy of 1 °C, while the RTD sensor has an accuracy of 0.15 °C @ room temperature and 0.45 @ 100 °C [52] and this can influence the result, given a higher inaccuracy.

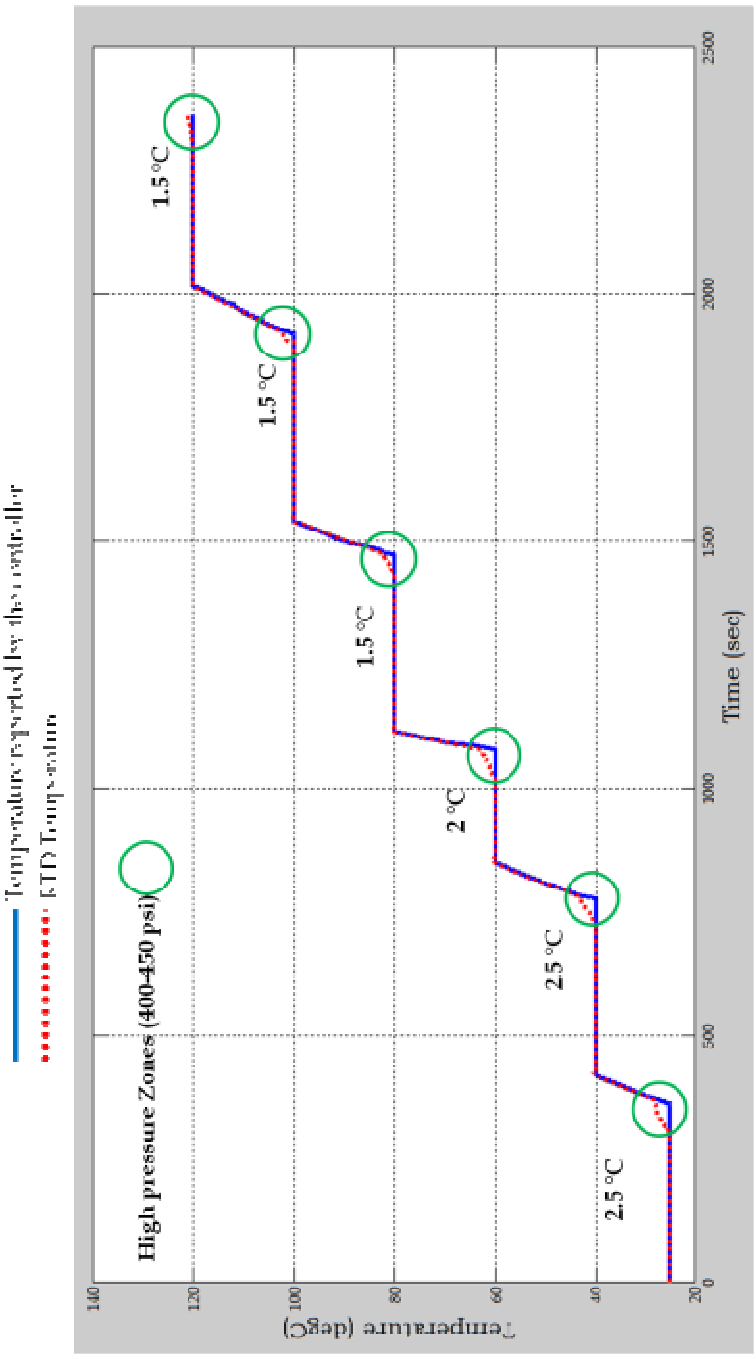

Figure 5-9.- RTD temperature sensor output versus temperature reported by the Temperature Controller. The increment of temperature due to the high pressure is written next to the green circle in each case.

5.6 Sensitivity

Sensitivity is an important characteristic of any sensor as it is part of the transfer function and defines the sensor response. Table 5-1 summarizes the sensitivities of the MEMS pressure sensor obtained during the experiments. As was predicted by the FEM model developed on Chapter 4, the sensitivity of the pressure sensor is affected by the adhesion of the parylene layer. The application of parylene creates a double layer structure that has two opposite influences: (1) it increases the thickness (stiffness) of the device; (2) it increases the mass of the whole structure. The parylene layer reduces the stress response of the diaphragm and hence the sensor sensitivity.

Table 5-1.- Sensitivity of the MEMS pressure sensors.

Samples	Sensitivity (mV/50 psi)	Sensitivity (mV/bar)	Reduction (%)
BCM sensor (no coating)	2.05	0.602	NA
COMSOL Model	1.5375	0.475	21%
First set	1.68	0.493	18%
Second set	1.67	0.490	18.5%

The experimental sensitivity loss is 3% smaller than that of COMSOL model. Even though, the experimental data fits well with the simulation trend, the discrepancy mainly arises due to the approximative nature of the finite element method. Details as a misalignment in placement of piezoresistors from the diaphragm edge, the difference between the boundary conditions assumed when the diaphragm is considered as a plate (clamped at the edges) and the clamping in the real case, the fact that in reality the stresses extend beyond the edge of the diaphragm [53], while the MEMS module of COMSOL Multiphysics® just consider the stress on the surface of the piezoresistors over the edge, can affect the final result of the model. The ideal built-in edges cannot accurately determine the stress distribution patterns found at the edges of the diaphragm, even a more accurate finite element model of the plate will always give a different value of output voltage than the real case as the stress values are overestimated. Regarding the instrumental error of the experiment, the manometer used at the test bench have an accuracy of 0.05% of Full Scale Output, which could represent an error of 0.6% between the sensitivity of the model and the sensitivity of the readings. Further study to develop an analytical model of the sensor response with a parylene layer over is required to determine a more accurate result.

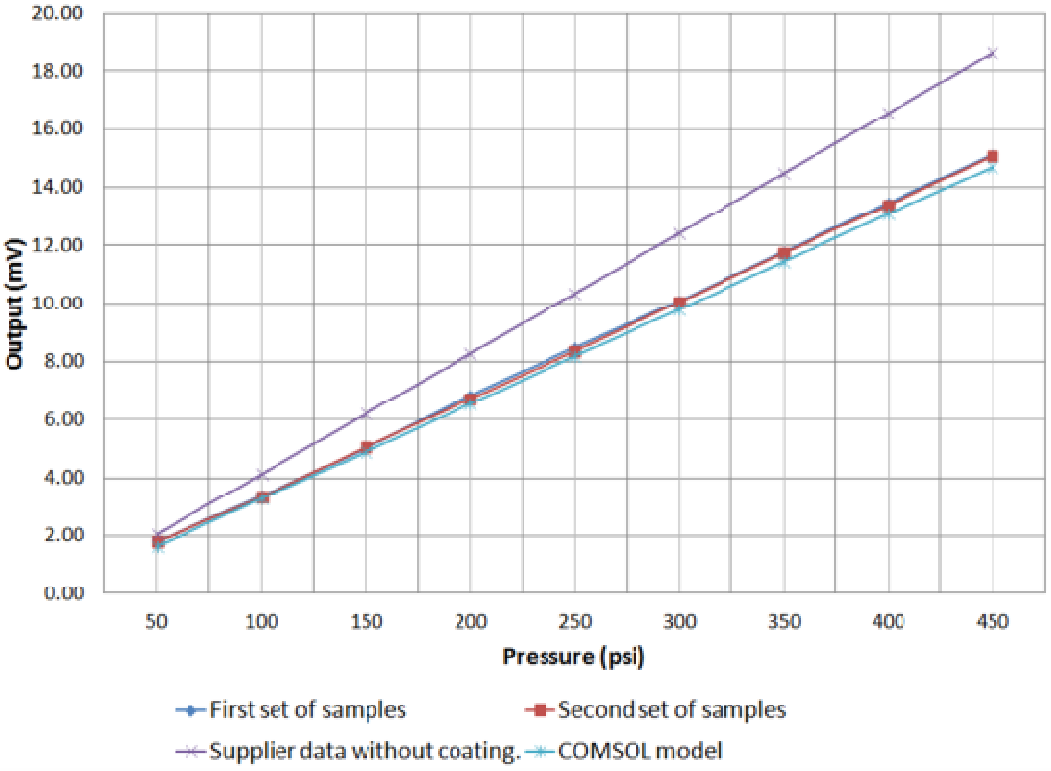

Figure 5-10.- Comparison between first and second set of samples with the output of the commercial sensor without coating and the COMSOL model. The first set of samples present a reduction in the sensitivity close to 18%, and the second set of samples gives a decrease in the sensitivity close to 18.5% due to the effect of the parylene layer. The COMSOL model reported a decrease of 21%.

5.7 Linearity

Non-linearity is defined as the deviation of the specified calibration curve (end point straight line or least square fit line) from the experimentally determined output of the sensor. For each of the read point, there is a particular deviation. The non-linearity error of a particular point is defined as the percentage deviation at that point. The maximum deviation is called the non-linearity of the sensor. Non-linearity at a particular point is defined as [46]:

$$NL_i = \frac{V_o(P_i) - \frac{V_o(P_m)}{P_m} P_i}{V_o(P_m)} \times 100\%$$

where P_i is pressure at a given point, P_m is the maximum pressure of the data set, and V_o is corresponding voltage output. The non-linearity at different values of pressure for all the

pressure steps is found using this formula. The maximum absolute value among the values of non-linearity calculated at various pressure steps is the non-linearity of the sensor. Using the data obtained from the experiment, the non-linearity can be calculated. Table 5-2 summarizes the non-linearity values of the samples tested.

Table 5-2.- Non-linearity of tested MEMS pressure sensor samples.

Samples	Non-Linearity (%)
First set	0.43
Second set	0.45

It is evident from figure 5-10, that the sensors respond quasi-linearly to pressure variations, which agrees with the expected result, as the only factors that can affect the piezoresistive pressure sensor linearity are the topology and placement of the piezoresistive elements, diaphragm thickness, and diaphragm length [54] .

Chapter 6

Conclusions and Future Work

6.1 Conclusions

In this thesis, a multifunctional MEMS sensor system for the simultaneous pressure and temperature measurement within a electro-hydraulic brake system was developed. An unpackaged piezoresistive MEMS pressure sensor and an unpackaged RTD temperature sensor were used due to their robustness, linearity, simple measurement circuitry and immunity to electromagnetic noise. The sensor system was fabricated by integrating these two MEMS sensors on a TO header small enough to allow having both sensors mounted within a single package. As the properties of the brake fluid could damage the MEMS sensors, a method to protect them was developed using Parylene as a protective layer. Since Parylene does not react with the brake fluid chemicals, it is capable to protect the sensor from the pH of the brake fluid and the inherent moisture of the fluid. Parylene has also a maximum operating temperature of 225°C at oxygen free environments.

To test the system under operating brake fluid conditions, the TO Header assembly was joined to a custom machined 18 NPT fitting, which is compatible with current fittings used for EHB systems and it works as the last interface between the sensor system and brake system. The joint process used during prototyping was micro-brazing since it results in small heat-affected zones and ensures that critical components such as the MEMS pressure sensor are unharmed. During testing, the MEMS pressure sensor was excited by a DC input voltage of 5 V while a current of 1 mAmp was applied to the RTD temperature sensor. The output of both sensors was continuosly monitored at different stimulus of temperature and pressure to simulate the brake fluid environment. Based on several experiments, the combined sensor output follows the pressure and temperature cycles of the hydraulic system setup very closely with a consistent pattern. The MEMS sensor system response was shown to be very repeatable for all testing cycles. The MEMS pressure sensor presented an average sensitivity of 0.490 mV/bar compared with the BMC sensor sensitivity of 0.602 mV/bar. The effect of the protection layer on the performance of the sensor system was studied numerically and experimentally. The reduction of the sensitivity of the pressure sensor due to the parylene layer was approximately 18.2% which closely agrees with the 21% reduction predicted by the model. The non-linearity of the MEMS pressure sensor at the tested range was found to be 0.4 % compared to the 0.25% reported by the manufacturer. The RTD temperature sensor reports an accuracy of 0.83% with respect to the temperature controller used. Based on the experimental results, the operating

range of the MEMS multifunctional sensor system could be improved to achieve a higher pressure measurement if a more robust TO Header is used. A better process to protect the wire bonds could also be used to increase the lifetime of the sensor.

One of the main advantages of the proposed sensor system resided in having both sensors in the same packaging and bonded onto the same substrate. Using MEMS technology ensures reduction of size and cost. Having a pressure and a temperature sensor within the same packaging allows the temperature compensation of the pressure sensor with a temperature reading that is being obtained within the same working conditions. Reduction of size reduces the disturbance of the sensor system to the wheel cylinder and in general the brake system. A smaller size also decreases installation cost and improve life cycle. Moreover, the proposed MEMS sensor system could be located exactly next to each brake actuator of the electro-hydraulic brake system with little or no intrusion to the brake fluid environment.

6.2 Future Work

6.2.1 Wire bonding protection.

Further study is needed to protect the wire bonding of the MEMS pressure sensor to the TO header. During the experiment, the connection of the MEMS pressure sensor of sample 1 and sample 2 was damaged. On the second set of samples, a stronger and more robust protection method was used but a better way is needed to protect the wire bonding and obtain a more reliable performance.

6.2.2 Fabrication process

The fabrication process can be improved by including a TO Header that can resist a higher pressure without presenting leaks. A smaller configuration can be obtained by fabricating both MEMS sensors within the same silicon substrate.

6.2.3 Experiments and test setups

The pressure and temperature experiments reported in this thesis were carried out in a controlled environment. For the next generation devices, dynamic tests resembling a real braking process of an EHB system is needed and would likely be performed using a real brake system.

Appendix A

Elements and materials properties of the Mechanical model.

Materials

n-Silicon (single-crystal, lightly doped)

C. S. Smith, “Piezoresistance Effect in Silicon and Germanium”, Physical Review, vol. 94, no. 1, pp. 42-49, 1957.

C. Jacoboni, C. Canali, G. Ottaviani and A. Alberigi Quaranta, “A Review of some Charge Transport Properties of Silicon”, Solid-State Electronics, vol. 20, pp. 77-89, 1977.

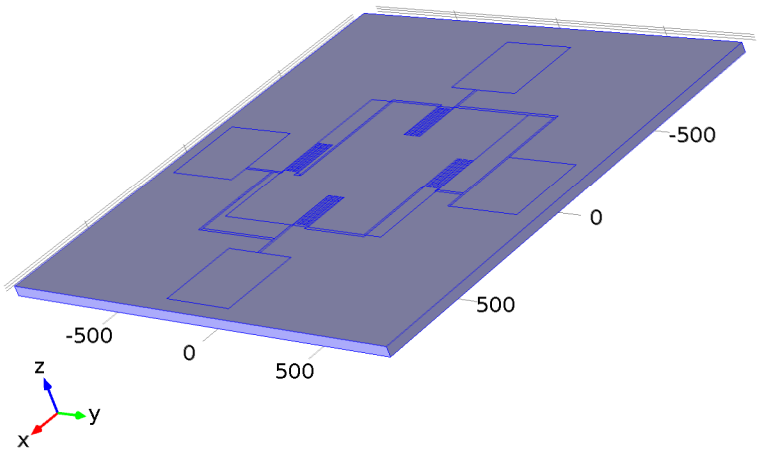

n-Silicon (single-crystal, lightly doped)

Material parameters

Name	Value	Unit
Density	2330[kg/m^3]	kg/m^3
Elasticity matrix, Voigt notation	{166[GPa], 64[GPa], 166[GPa], 64[GPa], 64[GPa], 166[GPa], 0[GPa], 0[GPa], 0[GPa], 80[GPa], 0[GPa], 0[GPa], 0[GPa], 0[GPa], 80[GPa], 0[GPa], 0[GPa], 0[GPa], 0[GPa], 0[GPa], 80[GPa]}	Pa

Basic Settings

Description	Value
Density	2330[kg/m^3]
Relative permittivity	{{4.5, 0, 0}, {0, 4.5, 0}, {0, 0, 4.5}}
Electrical conductivity	{{sigma0(nd[m^3]), 0, 0}, {0, sigma0(nd[m^3]), 0}, {0, 0, sigma0(nd[m^3])}}

Functions

Function name	Type
sigma0	Analytic

Anisotropic Settings

Description	Value
Elasticity matrix	{{166[GPa], 64[GPa], 64[GPa], 0[GPa], 0[GPa], 0[GPa]}, {64[GPa], 166[GPa], 64[GPa], 0[GPa], 0[GPa], 0[GPa]}, {64[GPa], 64[GPa], 166[GPa], 0[GPa], 0[GPa], 0[GPa]}, {0[GPa], 0[GPa], 0[GPa], 80[GPa], 0[GPa], 0[GPa]}, {0[GPa], 0[GPa], 0[GPa], 0[GPa], 80[GPa], 0[GPa]}, {0[GPa], 0[GPa], 0[GPa], 0[GPa], 0[GPa], 80[GPa]}}
Loss factor for elasticity matrix D	{{0, 0, 0, 0, 0, 0}, {0, 0, 0, 0, 0, 0}, {0, 0, 0, 0, 0, 0}, {0, 0, 0, 0, 0, 0}, {0, 0, 0, 0, 0, 0}, {0, 0, 0, 0, 0, 0}}

Anisotropic, Voigt notation Settings

Description	Value
Elasticity matrix, Voigt notation	{{166[GPa], 64[GPa], 64[GPa], 0[GPa], 0[GPa], 0[GPa]}, {64[GPa], 166[GPa], 64[GPa], 0[GPa], 0[GPa], 0[GPa]}, {64[GPa], 64[GPa], 166[GPa], 0[GPa], 0[GPa], 0[GPa]}, {0[GPa], 0[GPa], 0[GPa], 80[GPa], 0[GPa], 0[GPa]}, {0[GPa], 0[GPa], 0[GPa], 0[GPa], 80[GPa], 0[GPa]}, {0[GPa], 0[GPa], 0[GPa], 0[GPa], 0[GPa], 80[GPa]}}
Loss factor for elasticity matrix D, Voigt notation	{{0, 0, 0, 0, 0, 0}, {0, 0, 0, 0, 0, 0}, {0, 0, 0, 0,

Description	Value
	0, 0}, {0, 0, 0, 0, 0, 0}, {0, 0, 0, 0, 0, 0}, {0, 0, 0, 0, 0, 0}}

Piezoresistance form Settings

Description	Value
Piezoresistive coupling matrix	{{-102.2e-11[1/Pa]/sigma0(nd[m^3])[S/m], 53.4e-11[1/Pa]/sigma0(nd[m^3])[S/m], 53.4e-11[1/Pa]/sigma0(nd[m^3])[S/m], 0, 0, 0}, {53.4e-11[1/Pa]/sigma0(nd[m^3])[S/m], -102.2e-11[1/Pa]/sigma0(nd[m^3])[S/m], 53.4e-11[1/Pa]/sigma0(nd[m^3])[S/m], 0, 0, 0}, {53.4e-11[1/Pa]/sigma0(nd[m^3])[S/m], 53.4e-11[1/Pa]/sigma0(nd[m^3])[S/m], -102.2e-11[1/Pa]/sigma0(nd[m^3])[S/m], 0, 0, 0}, {0, 0, 0, -13.6e-11[1/Pa]/sigma0(nd[m^3])[S/m], 0, 0}, {0, 0, 0, 0, -13.6e-11[1/Pa]/sigma0(nd[m^3])[S/m], 0}, {0, 0, 0, 0, 0, -13.6e-11[1/Pa]/sigma0(nd[m^3])[S/m]}}

Functions

Function name	Type
sigma0	Analytic

Elastoresistance form Settings

Description	Value
Elastoresistive coupling matrix	{{-101.4/sigma0(nd[m^3])[S/m], 57.6/sigma0(nd[m^3])[S/m], 57.6/sigma0(nd[m^3])[S/m], 0, 0, 0}, {57.6/sigma0(nd[m^3])[S/m], -101.4/sigma0(nd[m^3])[S/m], 57.6/sigma0(nd[m^3])[S/m], 0, 0, 0}, {57.6/sigma0(nd[m^3])[S/m], 57.6/sigma0(nd[m^3])[S/m], -101.4/sigma0(nd[m^3])[S/m], 0, 0, 0}, {0, 0, 0, -10.8/sigma0(nd[m^3])[S/m], 0, 0}, {0, 0, 0, 0, -

Description	Value
	10.8/sigma0(nd[m^3])[S/m], 0}, {0, 0, 0, 0, 0, -10.8/sigma0(nd[m^3])[S/m]}}

Functions

Function name	Type
sigma0	Analytic

p-Silicon (single-crystal, lightly doped)

C. S. Smith, “Piezoresistance Effect in Silicon and Germanium”, Physical Review, vol. 94, no. 1, pp. 42-49, 1957.

C. Jacoboni, C. Canali, G. Ottaviani and A. Alberigi Quaranta, “A Review of some Charge Transport Properties of Silicon”, Solid-State Electronics, vol. 20, pp. 77-89, 1977.

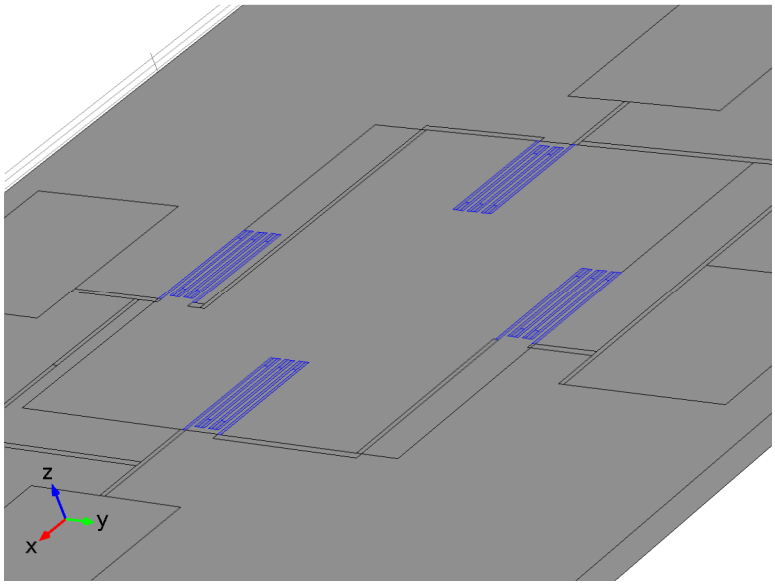

p-Silicon (single-crystal, lightly doped)

Material parameters

Name	Value	Unit
Relative permittivity	4.5	1
Electrical conductivity	sigma0(nd[m^3])	S/m

Name	Value	Unit
Piezoresistive coupling matrix	{6.6e-11[1/Pa]/sigma0(nd[m^3])[S/m], -1.1e-11[1/Pa]/sigma0(nd[m^3])[S/m], 6.6e-11[1/Pa]/sigma0(nd[m^3])[S/m], -1.1e-11[1/Pa]/sigma0(nd[m^3])[S/m], -1.1e-11[1/Pa]/sigma0(nd[m^3])[S/m], 6.6e-11[1/Pa]/sigma0(nd[m^3])[S/m], 0, 0, 0, 138.1e-11[1/Pa]/sigma0(nd[m^3])[S/m], 0, 0, 0, 0, 138.1e-11[1/Pa]/sigma0(nd[m^3])[S/m], 0, 0, 0, 0, 0, 138.1e-11[1/Pa]/sigma0(nd[m^3])[S/m]}	m^4/(s*A^2)

Basic Settings

Description	Value
Density	2330[kg/m^3]
Relative permittivity	{{4.5, 0, 0}, {0, 4.5, 0}, {0, 0, 4.5}}
Electrical conductivity	{{sigma0(nd[m^3]), 0, 0}, {0, sigma0(nd[m^3]), 0}, {0, 0, sigma0(nd[m^3])}}

Functions

Function name	Type
sigma0	Analytic

Anisotropic Settings

Description	Value
Elasticity matrix	{{166[GPa], 64[GPa], 64[GPa], 0[GPa], 0[GPa], 0[GPa]}, {64[GPa], 166[GPa], 64[GPa], 0[GPa], 0[GPa], 0[GPa]}, {64[GPa], 64[GPa], 166[GPa], 0[GPa], 0[GPa], 0[GPa]}, {0[GPa], 0[GPa], 0[GPa], 80[GPa], 0[GPa], 0[GPa]}, {0[GPa], 0[GPa], 0[GPa], 0[GPa], 80[GPa], 0[GPa]}, {0[GPa], 0[GPa], 0[GPa], 0[GPa], 0[GPa], 80[GPa]}}
Loss factor for elasticity matrix D	{{0, 0, 0, 0, 0, 0}, {0, 0, 0, 0, 0, 0}, {0, 0, 0, 0, 0, 0}, {0, 0, 0, 0, 0, 0}, {0, 0, 0, 0, 0, 0}, {0, 0, 0, 0, 0, 0}}

Anisotropic, Voigt notation Settings

Description	Value
Elasticity matrix, Voigt notation	{{166[GPa], 64[GPa], 64[GPa], 0[GPa], 0[GPa], 0[GPa]}, {64[GPa], 166[GPa], 64[GPa], 0[GPa], 0[GPa], 0[GPa]}, {64[GPa], 64[GPa], 166[GPa], 0[GPa], 0[GPa], 0[GPa]}, {0[GPa], 0[GPa], 0[GPa], 80[GPa], 0[GPa], 0[GPa]}, {0[GPa], 0[GPa], 0[GPa], 0[GPa], 80[GPa], 0[GPa]}, {0[GPa], 0[GPa], 0[GPa], 0[GPa], 0[GPa], 80[GPa]}}
Loss factor for elasticity matrix D, Voigt notation	{{0, 0, 0, 0, 0, 0}, {0, 0, 0, 0, 0, 0}, {0, 0, 0, 0, 0, 0}, {0, 0, 0, 0, 0, 0}, {0, 0, 0, 0, 0, 0}, {0, 0, 0, 0, 0, 0}}

Piezoresistance form Settings

Description	Value
Piezoresistive coupling matrix	{{6.6e-11[1/Pa]/sigma0(nd[m^3])[S/m], -1.1e-11[1/Pa]/sigma0(nd[m^3])[S/m], -1.1e-11[1/Pa]/sigma0(nd[m^3])[S/m], 0, 0, 0}, {-1.1e-11[1/Pa]/sigma0(nd[m^3])[S/m], 6.6e-11[1/Pa]/sigma0(nd[m^3])[S/m], -1.1e-11[1/Pa]/sigma0(nd[m^3])[S/m], 0, 0, 0}, {-1.1e-11[1/Pa]/sigma0(nd[m^3])[S/m], -1.1e-11[1/Pa]/sigma0(nd[m^3])[S/m], 6.6e-11[1/Pa]/sigma0(nd[m^3])[S/m], 0, 0, 0}, {0, 0, 0, 138.1e-11[1/Pa]/sigma0(nd[m^3])[S/m], 0, 0}, {0, 0, 0, 0, 138.1e-11[1/Pa]/sigma0(nd[m^3])[S/m], 0}, {0, 0, 0, 0, 0, 138.1e-11[1/Pa]/sigma0(nd[m^3])[S/m]}}

Functions

Function name	Type
sigma0	Analytic

Elastoresistance form Settings

Description	Value
Elastoresistive coupling matrix	{{9.6/sigma0(nd[m^3])[S/m], 1.8/sigma0(nd[m^3])[S/m], 1.8/sigma0(nd[m^3])[S/m], 0, 0, 0}, {1.8/sigma0(nd[m^3])[S/m], 9.6/sigma0(nd[m^3])[S/m], 1.8/sigma0(nd[m^3])[S/m], 0, 0, 0}, {1.8/sigma0(nd[m^3])[S/m], 1.8/sigma0(nd[m^3])[S/m], 9.6/sigma0(nd[m^3])[S/m], 0, 0, 0}, {0, 0, 0, 110.0/sigma0(nd[m^3])[S/m], 0, 0}, {0, 0, 0, 0, 110.0/sigma0(nd[m^3])[S/m], 0}, {0, 0, 0, 0, 0, 110.0/sigma0(nd[m^3])[S/m]}}

Functions

Function name	Type
sigma0	Analytic

Al - Aluminum / Aluminium

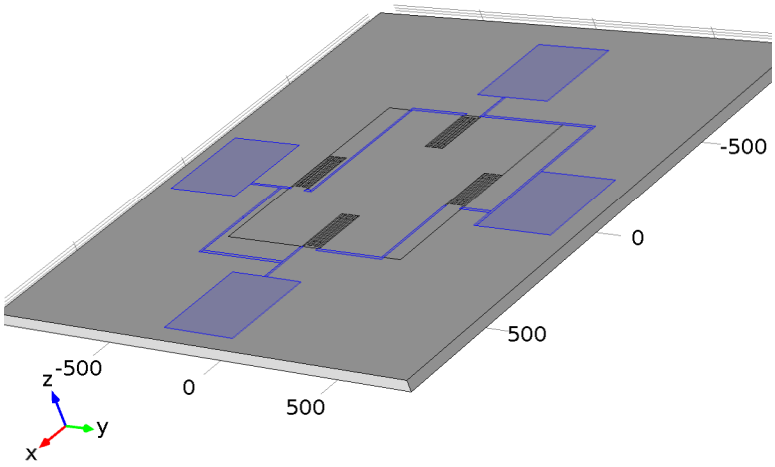

Al - Aluminum / Aluminium

Selection

Geometric entity level	Boundary
Selection	Boundaries 10–13, 16, 22, 32–33, 57–63, 75, 78–81

Material parameters

Name	Value	Unit
Electrical conductivity	35.5e6[S/m]	S/m
Relative permittivity	1.8	1

Basic Settings

Description	Value
Electrical conductivity	{{35.5e6[S/m], 0, 0}, {0, 35.5e6[S/m], 0}, {0, 0, 35.5e6[S/m]}}
Coefficient of thermal expansion	{{23.1e-6[1/K], 0, 0}, {0, 23.1e-6[1/K], 0}, {0, 0, 23.1e-6[1/K]}}
Heat capacity at constant pressure	904[J/(kg*K)]
Density	2700[kg/m^3]
Thermal conductivity	{{237[W/(m*K)], 0, 0}, {0, 237[W/(m*K)], 0}, {0, 0, 237[W/(m*K)]}}
Relative permittivity	{{1.8, 0, 0}, {0, 1.8, 0}, {0, 0, 1.8}}

Young's modulus and Poisson's ratio Settings

Description	Value
Young's modulus	70.0e9[Pa]
Poisson's ratio	0.35

Parylene

The properties were obtained from MATWEB and from the datasheet of SCS

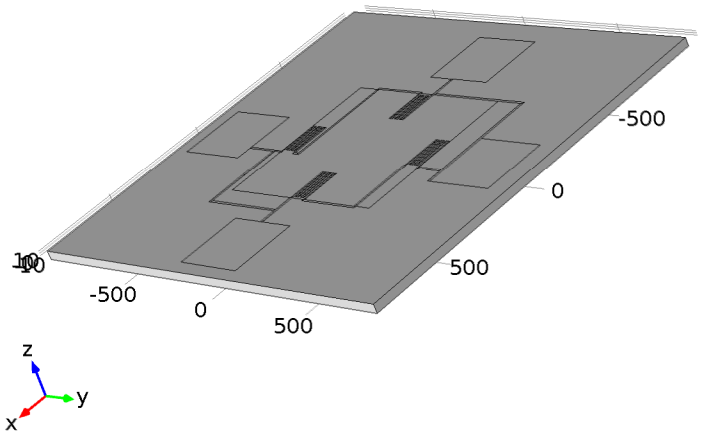

Parylene

Selection

Geometric entity level	Domain
Selection	No domains

Basic Settings

Description	Value
Bulk viscosity	
Density	1290
Absorption coefficient	.1
Coefficient of thermal expansion	{{0.0000350, 0, 0}, {0, 0.0000350, 0}, {0, 0, 0.0000350}}
Relative permeability	{{0.08, 0, 0}, {0, 0.08, 0}, {0, 0, 0.08}}
Thermal conductivity	{{0.0840, 0, 0}, {0, 0.0840, 0}, {0, 0, 0.0840}}
Electrical conductivity	{{1e-14, 0, 0}, {0, 1e-14, 0}, {0, 0, 1e-14}}
Heat capacity at constant pressure	712
Relative permittivity	{{2.95, 0, 0}, {0, 2.95, 0}, {0, 0, 2.95}}

Young's modulus and Poisson's ratio Settings

Description	Value
Young's modulus	2.76e+9

Description	Value
Poisson's ratio	0.4

Table 6-1. Young modulus of parylene versus temperature [55]

Temperature (°C)	Young modulus
10	3.5
25	2.67
40	2.17
60	1.05
80	0.826
100	0.671
120	0.601
150	0.503

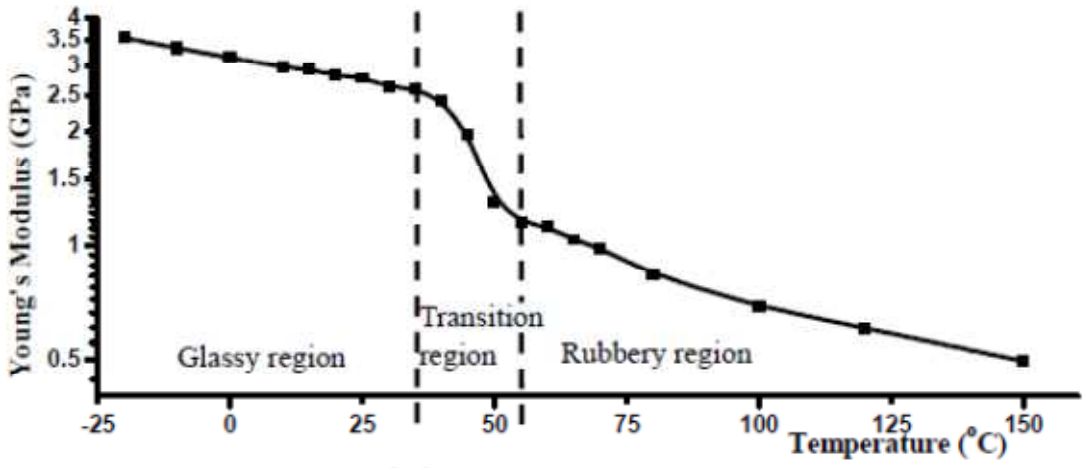

Figure 6-1. Young's modulus versus temperature curve.

Table 6-2. Young modulus of Silicon versus temperature [56]

Temperature (°C)	Young modulus
10	169
25	167
40	167
60	165
80	165
100	165
120	165
150	165

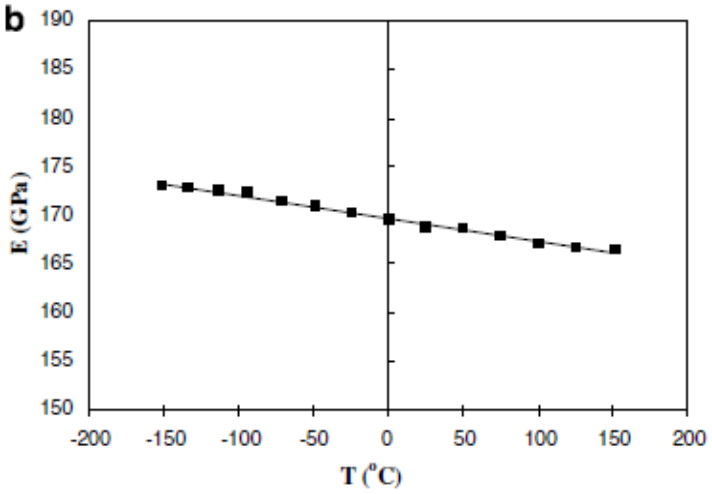

Figure 6-2. Young modulus of Silicon versus temperature

Appendix B

Elements and materials properties of the RTD model.

Materials

Borosilicate

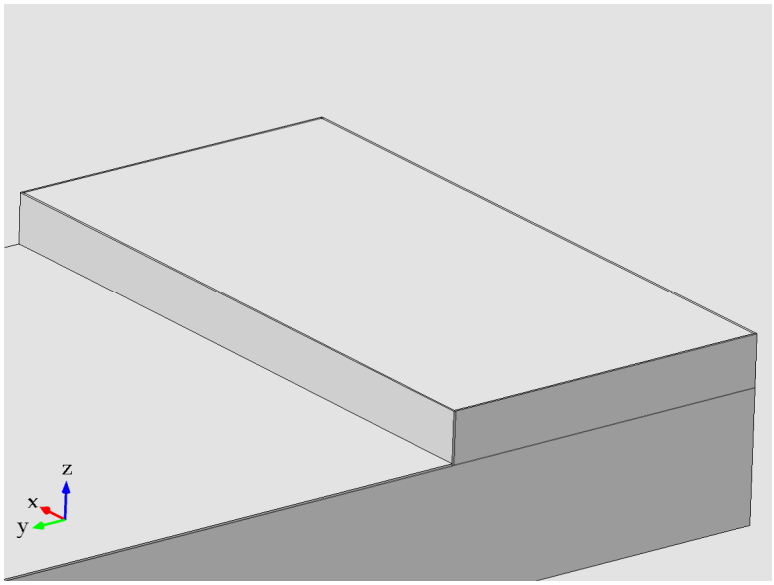

Borosilicate

Selection

Geometric entity level	Domain
Selection	Domain 9

Material parameters

Name	Value	Unit
Heat capacity at constant pressure	int10(t)[J/(kg*K)]	J/(kg*K)
Density	2230[kg/m^3]	kg/m^3
Thermal conductivity	int11(t)[W/(m*K)]	W/(m*K)

Basic Settings

Description	Value
Electrical conductivity	{{0[S/m], 0, 0}, {0, 0[S/m], 0}, {0, 0, 0[S/m]}}
Coefficient of thermal expansion	{{3.3e-6[1/K], 0, 0}, {0, 3.3e-6[1/K], 0}, {0, 0, 3.3e-6[1/K]}}
Heat capacity at constant pressure	int10(t)[J/(kg*K)]

Description	Value
Relative permittivity	{{4.8, 0, 0}, {0, 4.8, 0}, {0, 0, 4.8}}
Density	2230[kg/m^3]
Thermal conductivity	{{int11(t)[W/(m*K)], 0, 0}, {0, int11(t)[W/(m*K)], 0}, {0, 0, int11(t)[W/(m*K)]}}

Young's modulus and Poisson's ratio Settings

Description	Value
Young's modulus	63e9[Pa]
Poisson's ratio	0.20

Pt - Platinum

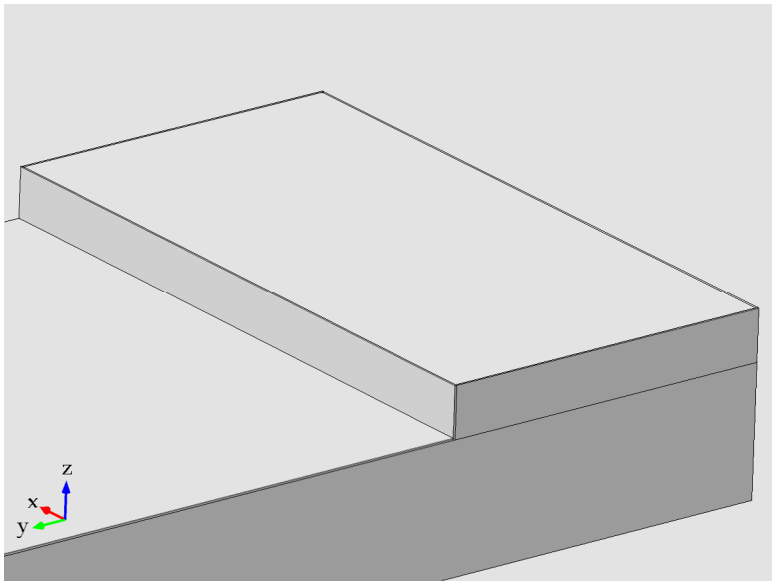

Pt - Platinum

Selection

Geometric entity level	Domain
Selection	Domain 8

Material parameters

Name	Value	Unit
Heat capacity at constant pressure	int9(t)[J/(kg*K)]	J/(kg*K)
Density	21450[kg/m^3]	kg/m^3

Name	Value	Unit
Thermal conductivity	int8(t)[W/(m*K)]	W/(m*K)

Basic Settings

Description	Value
Electrical conductivity	{{8.9e6[S/m], 0, 0}, {0, 8.9e6[S/m], 0}, {0, 0, 8.9e6[S/m]}}
Coefficient of thermal expansion	{{8.80e-6[1/K], 0, 0}, {0, 8.80e-6[1/K], 0}, {0, 0, 8.80e-6[1/K]}}
Heat capacity at constant pressure	int9(t)[J/(kg*K)]
Density	21450[kg/m^3]
Thermal conductivity	{{int8(t)[W/(m*K)], 0, 0}, {0, int8(t)[W/(m*K)], 0}, {0, 0, int8(t)[W/(m*K)]}}

Young's modulus and Poisson's ratio Settings

Description	Value
Young's modulus	168e9[Pa]
Poisson's ratio	0.38

Parylene

The properties were obtained from MATWEB and from the datasheet of SCS

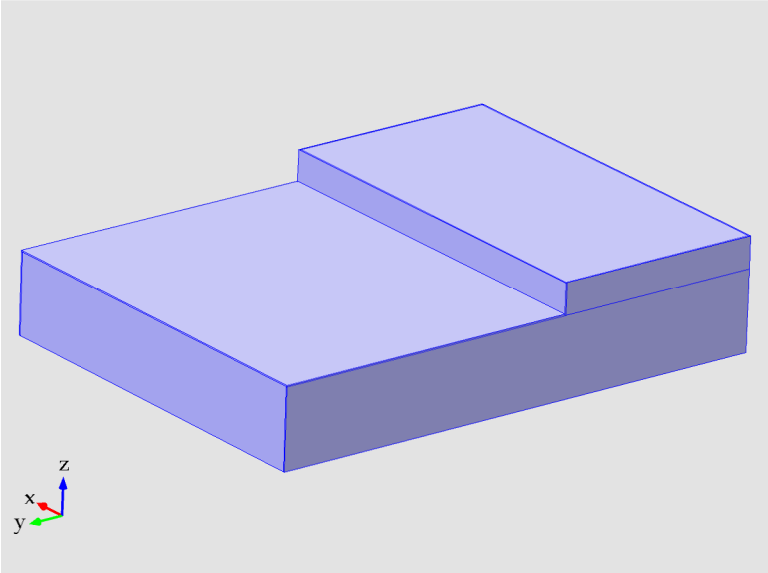

Parylene

Selection

Geometric entity level	Domain
Selection	Domains 2–6, 10–13

Material parameters

Name	Value	Unit
Density	1290	kg/m^3
Thermal conductivity	0.0840	W/(m*K)
Heat capacity at constant pressure	712	J/(kg*K)

Basic Settings

Description	Value
Bulk viscosity	1
Density	1290
Absorption coefficient	.1
Coefficient of thermal expansion	{{0.0000350, 0, 0}, {0, 0.0000350, 0}, {0, 0, 0.0000350}}
Relative permeability	{{0.08, 0, 0}, {0, 0.08, 0}, {0, 0, 0.08}}
Thermal conductivity	{{0.0840, 0, 0}, {0, 0.0840, 0}, {0, 0, 0.0840}}
Electrical conductivity	{{1e-14, 0, 0}, {0, 1e-14, 0}, {0, 0, 1e-14}}
Heat capacity at constant pressure	712
Relative permittivity	{{2.95, 0, 0}, {0, 2.95, 0}, {0, 0, 2.95}}

Young's modulus and Poisson's ratio Settings

Description	Value
Young's modulus	2.76e+9
Poisson's ratio	0.4

KOVAR

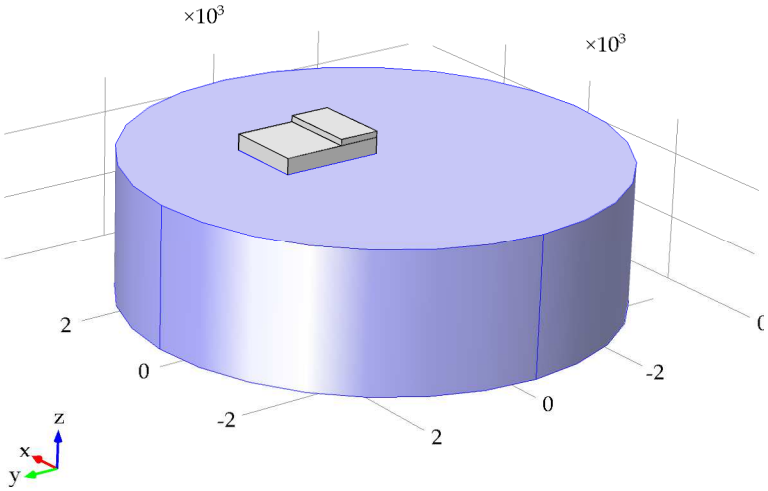

KOVAR

Selection

Geometric entity level	Domain
Selection	Domain 1

Material parameters

Name	Value	Unit
Density	8360	kg/m^3
Thermal conductivity	17.3	W/(m*K)
Heat capacity at constant pressure	439	J/(kg*K)

Basic Settings

Description	Value
Density	8360
Thermal conductivity	{{17.3, 0, 0}, {0, 17.3, 0}, {0, 0, 17.3}}
Heat capacity at constant pressure	439

Al2O3 - Aluminum oxide / Aluminium oxide

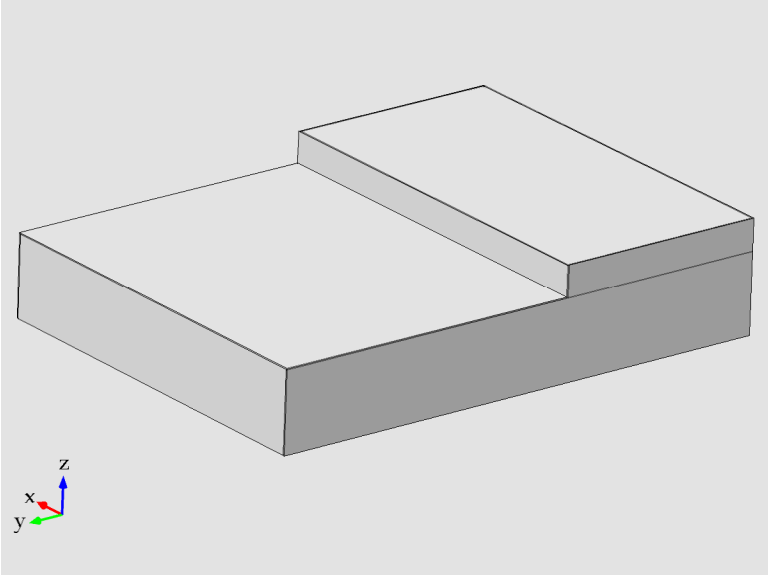

Al2O3 - Aluminum oxide / Aluminium oxide

Selection

Geometric entity level	Domain
Selection	Domain 7

Material parameters

Name	Value	Unit
Heat capacity at constant pressure	int13(t)[J/(kg*K)]	J/(kg*K)
Density	3965[kg/m^3]	kg/m^3
Thermal conductivity	int12(t)[W/(m*K)]	W/(m*K)

Basic Settings

Description	Value
Electrical conductivity	{{0[S/m], 0, 0}, {0, 0[S/m], 0}, {0, 0, 0[S/m]}}
Coefficient of thermal expansion	{{6.5e-6[1/K], 0, 0}, {0, 6.5e-6[1/K], 0}, {0, 0, 6.5e-6[1/K]}}
Heat capacity at constant pressure	int13(t)[J/(kg*K)]
Relative permittivity	{{5.7, 0, 0}, {0, 5.7, 0}, {0, 0, 5.7}}
Density	3965[kg/m^3]
Thermal conductivity	{{int12(t)[W/(m*K)], 0, 0}, {0, int12(t)[W/(m*K)], 0},

Description	Value
	{0, 0, int12(t)[W/(m*K)]}}

Young's modulus and Poisson's ratio Settings

Description	Value
Young's modulus	400e9[Pa]
Poisson's ratio	0.22

Steel AISI 4340

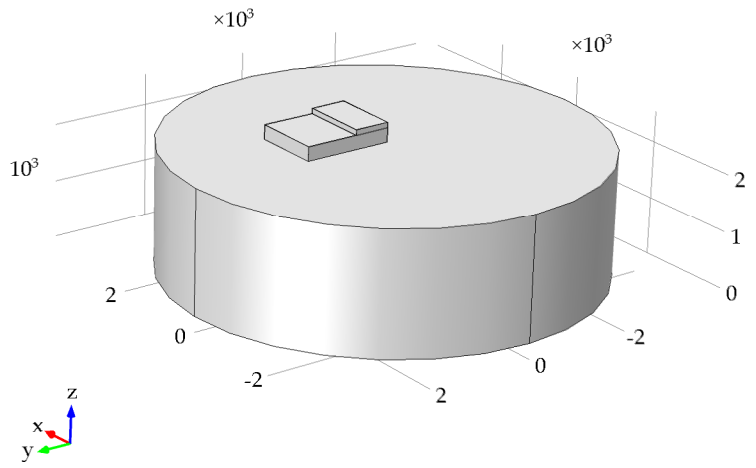

Steel AISI 4340

Selection

Geometric entity level	Domain
Selection	No domains

Basic Settings

Description	Value
Relative permeability	{{1, 0, 0}, {0, 1, 0}, {0, 0, 1}}
Electrical conductivity	{{4.032e6[S/m], 0, 0}, {0, 4.032e6[S/m], 0}, {0, 0, 4.032e6[S/m]}}
Coefficient of thermal expansion	{{12.3e-6[1/K], 0, 0}, {0, 12.3e-6[1/K], 0}, {0, 0, 12.3e-6[1/K]}}

Description	Value
Heat capacity at constant pressure	475[J/(kg*K)]
Relative permittivity	{{1, 0, 0}, {0, 1, 0}, {0, 0, 1}}
Density	7850[kg/m^3]
Thermal conductivity	{{44.5[W/(m*K)], 0, 0}, {0, 44.5[W/(m*K)], 0}, {0, 0, 44.5[W/(m*K)]}}

Young's modulus and Poisson's ratio Settings

Description	Value
Young's modulus	205e9[Pa]
Poisson's ratio	0.28

Temperature-dependent properties

TConductivity_Platinum

Function name	int8
Function type	Interpolation

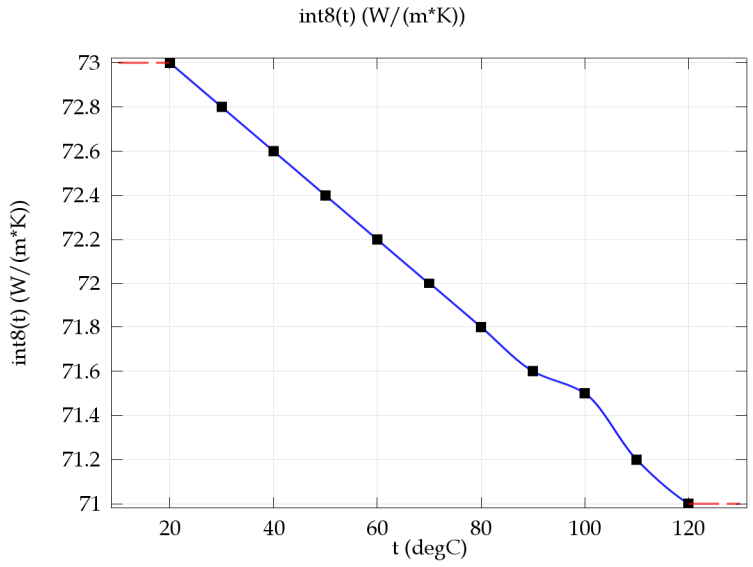

TConductivity_Platinum

HeatCapacityPlatinum

Function name	int9
Function type	Interpolation

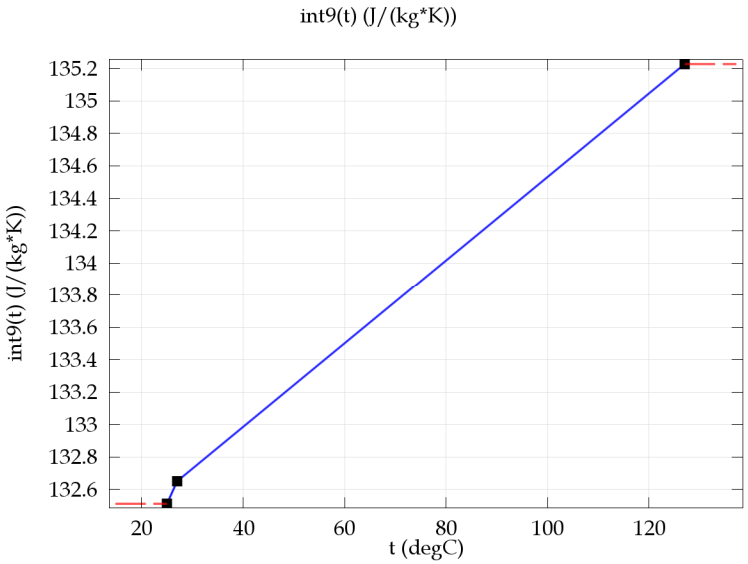

HeatCapacityPlatinum

THeatCapacity_Borosilicate

Function name	int10
Function type	Interpolation

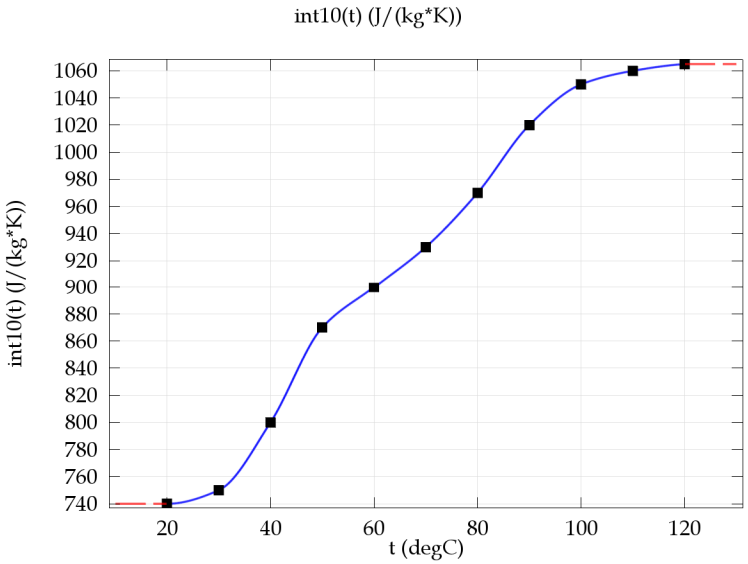

THeatCapacity_Borosilicate

TConductivity_Borosilicate

Function name	int11
Function type	Interpolation

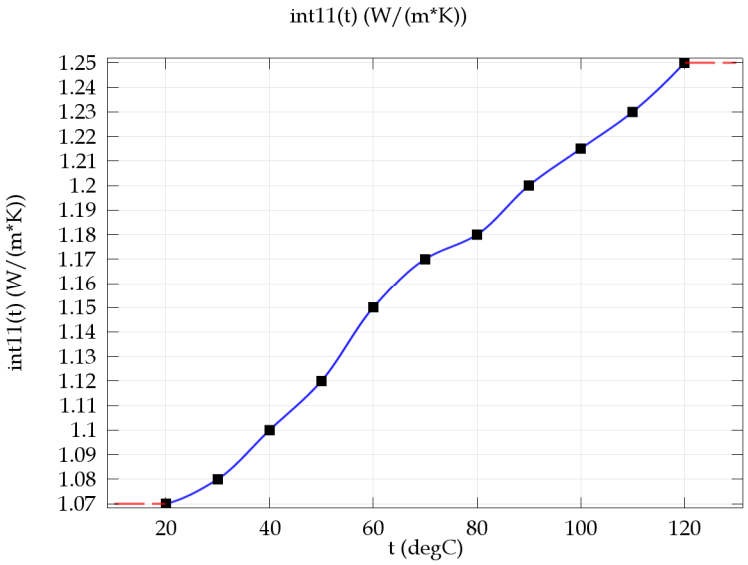

TConductivity_Borosilicate

TConductivity_alumina

Function name	int12
Function type	Interpolation

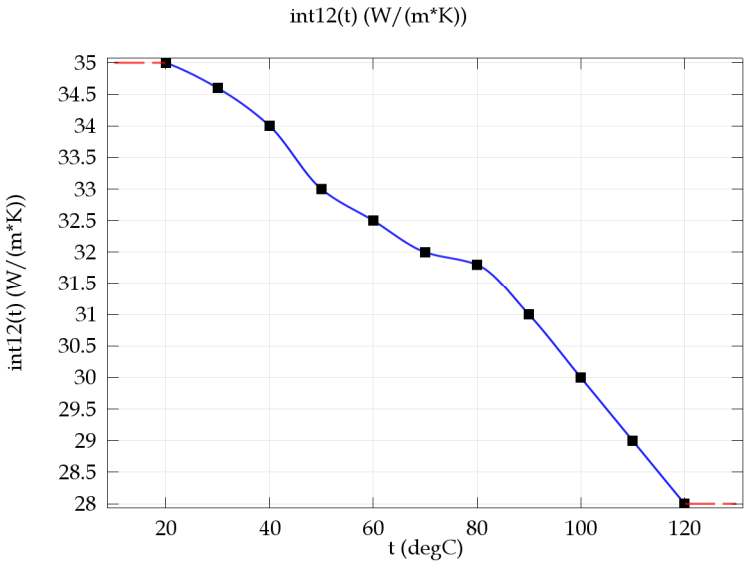

TConductivity_alumina

HeatCapacityAlumina

Function name	int13
Function type	Interpolation

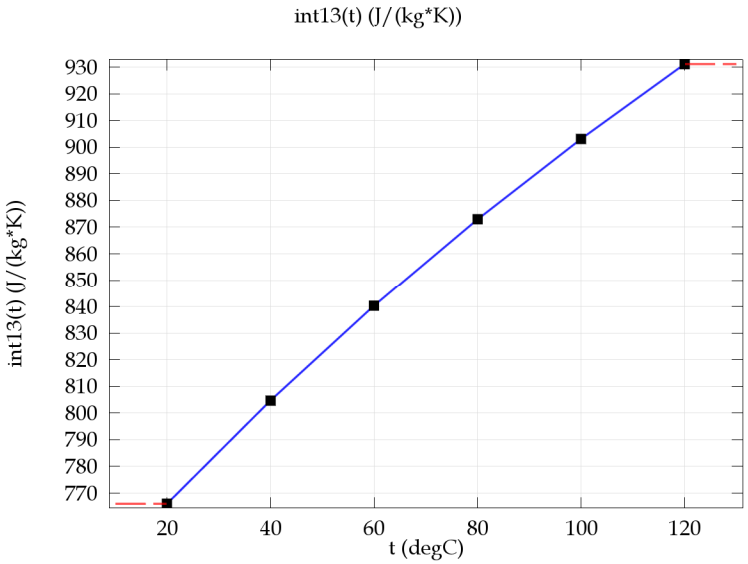
int13(t) (J/(kg*K))
930
920
910
900
890
880
870
860
850
840
830
820
810
800
790
780
770
int13(t) (J/(kg*K))
20
40
60
80
100
120
t (degC)

Appendix C

Convergence plots of the models.

Definition of Convergence.- arriving at a solution that is close to the exact solution within some pre-specified error tolerance or other convergence criterion. The following convergence plots shows the error estimate decreasing between Newton-Raphson iterations obtained from COMSOL Multiphysics. Ideally, the error should go down monotonically if it does converge, then start investigating ramping the loads, the nonlinearities, or the Multiphysics couplings. For the Fig 6-3, the piezoresistive physics and the mechanical physics converge with an error less than 10^{-5}. For the Fig 6-4 the thermal physics converge with an error less than 10^{-3}.

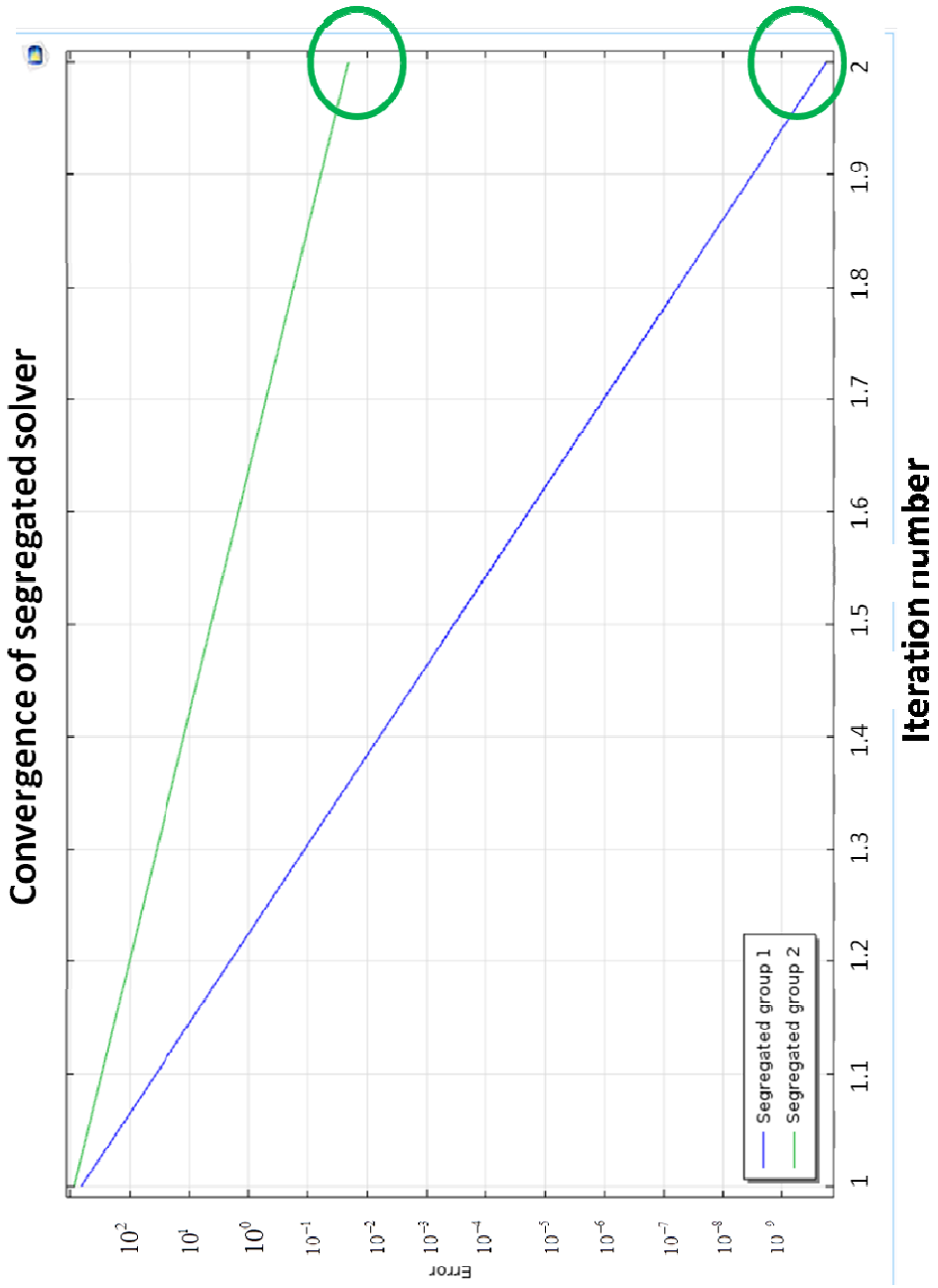

Figure 6-3. Convergence of the MEMS pressure sensor model.

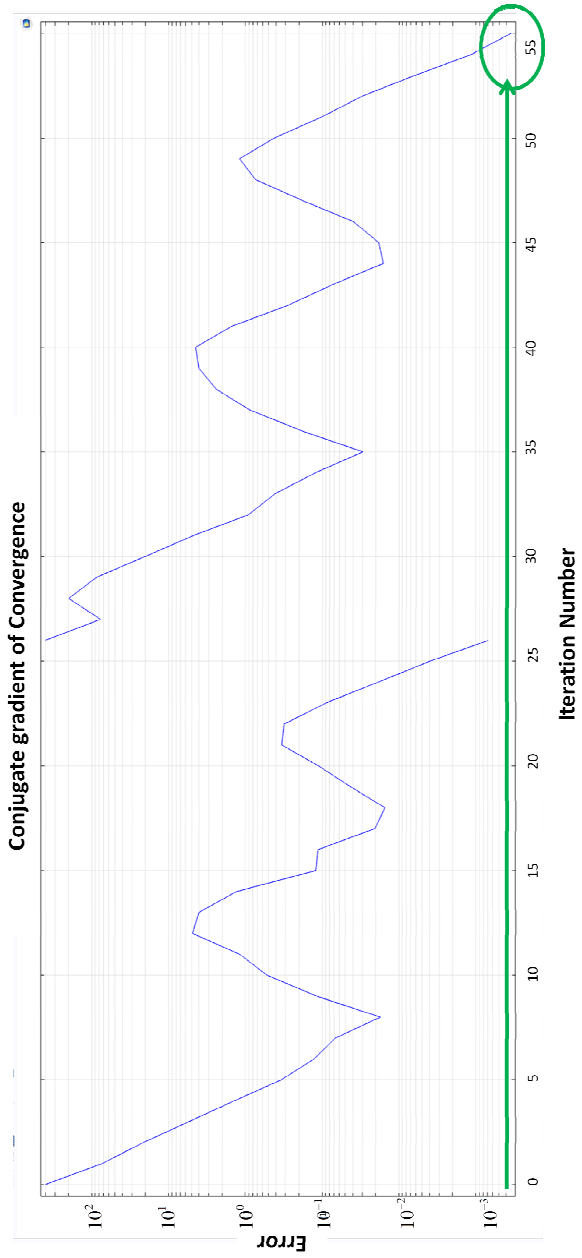

Figure 6-4. Convergence of the RTD Model

References

[1] SAE, “Motor Vehicle Brake Fluids,” *SAE Specifications SAE J1703,* p. 3, 2012.

[2] A. Neys, “In-vehicle brake system temperature model.,” *Master's thesis Chalmers University of Technology, Department of Applied Mechanics*, 2012.

[3] K. Lee, “Numerical prediction of brake fluid temperature rise during braking and heat soaking,” *International Congress and Exposition DELPHI*, 1999.

[4] B. Kant, “Sensotronic brake control (SBC),” *Automotive Mechatronics, Bosch Professional Automotive Information,* pp. 412-415, 2015.

[5] SAE, “Operating performance of motor vehicle braking systems as affected by fluid water content,” *SAE Specifications,* 1971.

[6] H. Tai Ran, MEMS and microsystems : design, manufacture, and nanoscale engineering, John Wiley, 2008.

[7] D. D'Ambrosi, “Fiat 500L: é arrivato il City Brake Control,” FIAT, 2013.

[8] Mitsubishi, “Mitsubishi Motors Develops "e-Assist" Active Safety Technology - Forward Collision Mitigation System,” Mitsubishi Motors, 2012.

[9] F. E. NCAP, “Ford Active City Stop,” Ford, 2013.

[10] K. Sidhu, “Micro Electro-Mechanical System Forge Advancements and Use of Pressure Sensor Technology,” *Macro Sensors,* 2014.

[11] K. W. A.V. Chavan, “Batch-processed vacuum-sealed capacitive pressure sensor,” *Journal of Microelectromechanical Systems,* vol. 10, 2001.

[12] J. C.S. Sander, “A monolithic capacitive pressure sensor with pulse-period output,” *IEEE Trans Electron Devices,* 1980.

[13] K. Y.S. Lee, “A batch-fabricated silicon capacitive pressure transducer with low temperature sensitivity,” *IEEE Trans. Electron Devices,* 1982.

[14] D. Z. Young D.J., “High-temperature single-crystal 3C-SiC capacitive pressure sensor,” *IEEE Sensors Journal*, pp. 464-470, 2004.

[15] A. W.D. Frobenius, “A microminiature, solid-state capacitive blood pressure sensor transducer

with improved sensitivity," *IEEE Trans. Biomed.*, 1973.

[16] W. &. S. ,. J. Eaton, "Micromachined pressure sensor: Review and recent developments," *Smart Materials & Structures,* pp. 530-539, 1998.

[17] P. G. Blazquez, "Capabilities and limits of silicon pressure sensors," *Sensors and Actuators,* vol. 17, 1989.

[18] J. A. K. Karsten, "CMOS- compatible capacitive high temperature pressure sensors," *Sensors and Actuators,* vol. 85, pp. 147-152, 2000.

[19] Motorola, *Freescale Semiconductor datasheets.*

[20] M. Berkson, "Pressure Transducer, understanding and specifying SENSATA Technologies capacitive pressure transducers," *SENSATA Technologies,* 2007.

[21] J. Degrieck, "Embedded optical fibre sensors for the permanent monitoring of filament wound pressure vessels," *Internaltional Conference on Advanced Materials,* 1998.

[22] C. Liu, Foundations of MEMS, Prentice Hall, 2012.

[23] A. Najafi Sohi, A Multifunctional MEMS Pressure and Temperature Sensor for Harsh Environment Applications (Doctoral dissertation)., Waterloo, Ontario.: Retrieved from UWSpace of the University of Waterloo. (Accession URL http://hdl.handle.net/10012/7346), 2013.

[24] C. K. &. H. M. Guo S., "High temperature smart-cut SOI pressure sensor," *Sensors and Actuators A: Physical,* pp. 255-260, 2002.

[25] J. Wilson, Sensor Technology Handbook, Elsevier, 2004.

[26] W. J. Fleming, "Overview of Automotive Sensors," *IEEE Sensors Journal,* 2001.

[27] E. J. P. Santos, "RTD-based Smart Temperature Sensor: Process development and circuit design," *International Conference on Microelectronics,* 2008.

[28] J. Kim, "A study on the fabrication of an RTD (Resistance Temperature Detector) by using Pt thin film," *Korean Journal of Chemistry Engineering,* pp. 61-66, 2001.

[29] G. &. C. M. Mohammadi A. R., "Development of a compensated capacitive pressure and temperature sensor using adhesive bonding and chemical-resistance coating for multiphase chemical reactors," *Sensors and Actuators A: Physical,* 2010.

[30] A. Pisano, "Harsh environment wireless MEMS sensors for energy & power.," *MTO (DARPA*

Microsystems Technology Office) Symposium, 2009.

[31] A. R. Mohammadi, MEMS pressure, temperature and conductivity sensors for high temperature and harsh environment, University of British Columbia Phd Thesis., 2011.

[32] E. S. a. H. H. Jonathan Oiler, "Harsh Environment Sensor Array-Enabled Hot Spring Mapping," *IEEE Sensors Journal*, vol. 14, no. 10, 2014.

[33] C. L. &. W. Z. Zhang Zongyang, "Optimization of Packaging Process of Piezoresistive Engine Oil Pressure Sensor," *11th International Conference on Electronic Packaging Technology High Density Packaging (ICEPT- HDP)*, 2010.

[34] B. Mertens J. & E., "Effects of temperature and pressure on microcantilevers resonance response," *Ultramicroscopy*, 2003.

[35] A. N. Sohi, "A structurally multifunctional pressure and temperature sensor," *MNRC*, 2009.

[36] L. Durali, "A new individual wheel actuated braking system to improve reliability and vehicle stability," *A Research Proposal proposed for PhD. Comprehensive Examination*, p. 39, 2013.

[37] B. Sensors, "Datasheet of SE103 ,pressure sensor dies for pressure applications," *Datasheet BCM Sensors*, 2014.

[38] T. R. B. a. G. F. E. K. Dyrbye, "Packaging of physical sensors for aggressive media applications," *J. Micromech. Microeng*, vol. 6, no. 1, p. 187, 1996.

[39] C. P. B. &. C. M. Mohammadi Abdolreza R., "Development of a Combined Piezoresistive Pressure and Temperature Sensor Using a Chemical Protective Coating for Kraft Pulp Digester Process Monitoring," *Journal of Micromechanics and Microengineering 21*, 2011.

[40] J. Licari, Coating Materials for Electronic Applications - Polymers, Processes, Reliability and Testing., Whittier California: Noyes Publications , 2003.

[41] L. James, "Reliability Assurance and Testing In Coating Materials for Electronics Applications," *Materials and Processes for Electronic Applications*, 2003.

[42] Q. L. S. P. K. X. T. &. S. C. Li Xin, "High- Temperature Piezoresistive Pressure Sensor Based on Implantation of Oxygen into Silicon Wafer," *Sensors and Actuators A: Physical 179*, 2012.

[43] L. W. Corporation, "Callendar-Van Dusen Equation and RTD Temperature Sensors," *Light Wave Corporation*, 2010.

[44] IJARCET, "Design and Simulation of MEMS based Microhotplate as Gas Sensor," *International*

Journal of Advanced Research in Computer Engineering & Technology, 2013.

[45] B. S. Santosh Kumar, “Design Principles and considerations for the "ideal" Silicon Piezoresistivity Pressure Sensor: A Focused Review.,” *Microsystems Technologies 20,* pp. 1213-1247, 2014.

[46] B. Min-Hang, Analysis and design principles of MEMS devices, Amsterdam: Elsevier, 2005.

[47] S. D., Microsystems Design, Springer, Kluwer Academic Publishers, 2002.

[48] S. K. S. S. Meenatchisundaram, “Sensitivity Analysis of Different Models of Piezoresistive Micro Pressure Sensors,” *Proceedings of the 2013 COMSOL Conference,* 2013.

[49] H.-M. A. S.-C. BS., “Electromechanical analysis of a Piezoresistive Pressure Micro-sensor for low-pressure biomedical applications,” *Revista Mexicana de Fisica,* 2009.

[50] C. Yunus, Thermodynamics: an engineering approach, New York: McGraw-Hill, 2011.

[51] W. M. David Buchla, Applied electronics Instrumentation and Measurement, New York: Macmillan Publishing Company, 1992.

[52] ASTM, “ASTM E1137-97, Standard Specification for Industrial Platinum Resistance Thermometers.,” *ASTM International,* 1997.

[53] Y. W. C. H. C. M. Lin L, “Surface micromachined diaphragm pressure sensors with optimized piezoresistive sensing resistors,” *Proceedings of the IEEE international conference on microelectronics and VLSI.,* p. 24–27, 1995.

[54] B. P. S. Santosh Kumar, “Design principles and considerations for the "ideal" silicon piezoresistive pressure sensor: a focused review.,” *Microsystem Technology,* vol. 20, pp. 1213-1247, 2014.

[55] P. D. G. L. B. L. Y.-K. L. J. C.-H. Lin, “Creep of parylene-C film 2011,” *16th International Solid-State Sensors, Actuators and Microsystems Conference (TRANSDUCERS), 2011 ,* p. 2698–2701., 2011.

[56] C. Cho, “Characterization of Young’s modulus of silicon versus temperature using a ‘beam deflection’ method with a four-point bending fixture.,” *Current Applied Physics,* vol. 9, no. 2, pp. 538-545, 2009.

[57] P. S. Z. Chu, “Silicon three-axial tactile sensor,” *Sensors and Actuators 54,* 1996.